Region Of Interest Based Image Classification: A Study in MRI Brain Scan Categorization

Thesis submitted in accordance with the requirements of
the University of Liverpool for the degree of Doctor in
Philosophy
by
Ashraf Elsayed

November 2011

Dedication

To my family,
especially
my wife and my children

Abstract

This thesis describes research work undertaken in the field of *image mining.* More specifically, the research work is directed at image classification according to the nature of a particular Region Of Interest (ROI) that appears across a given image set. Four approaches are described in the context of the classification of medical images. The first is founded on the extraction of a ROI signature using the Hough transform, but using a polygonal approximation of the ROI boundary. The second approach is founded on a weighted subgraph mining technique whereby the ROI is represented using a quad-tree structure which allows the application of a weighted subgraph mining technique to identify feature vectors representing these ROIs; these can then be used as the foundation with which to build a classifier. The third uses an efficient mechanism for determining Zernike moments as a feature extractor, which are then translated into feature vectors to which a classification process can be applied. The fourth is founded on a time series analysis technique whereby the ROI is represented as a pseudo time series which can then be used as the foundation for a Case Based Reasoner. The presented evaluation is directed at MRI brain scan data where the classification is focused on the *corpus callosum*, a distinctive ROI in such data. For evaluation purposes three scenarios are considered: distinguishing between musicians and non-musicians, left handedness and right handedness, and epilepsy patient screening.

Acknowledgement

First and Foremost, I am very grateful to my first supervisor Dr. Frans Coenen, specially for his constant patience, ongoing support and encouragement throughout the past four years. His enthusiasm, constructive criticism, research ideas and always making time for discussions have made the completion of my Ph.D. possible and highly enjoyable. I am privileged to have worked with him.

I would like to express my gratitude to my second supervisor, Dr. Marta García-Fiñana, for her assistance, suggestions and valuable comments; and to thank Dr. Vanessa Sluming, for her assistance and her medical expertise. I also would like to express my gratitude to Joanne Powell for assistance in supplying the "handedness" data set; and to my colleague, Chuntao Jiang (Geof), for our collaborative research work.

The Department of Computer Science in general at the University of Liverpool has been an excellent place in which to conduct research, and all members of staff and colleagues have been encouraging and helpful whenever needed.

Fundamental to my being able to conduct this research was the financial support of the Egyptian government, so I also extend my gratitude to the Egyptian Cultural Bureau in London, and Alexandria University.

Last, but by no means least, I am eternally indebted to my wife for her constant support and encouragement, without whom the completion of my Ph.D. would not have been possible to accomplish.

Contents

List of Figures

List of Tables

Chapter 1

Introduction

"Knowledge Discovery in Data (KDD) is the non-trivial process of identifying valid, novel, potentially useful, and ultimately understandable patterns in data" [49]. Data mining is an essential element within this process that is concerned with the discovery of the desired hidden information within the data. The data that data miners wish to mine comes in many different forms including: images, graphs, text and so on. Consequently, data mining includes sub-fields such as image mining, graph mining, and text mining. The work described in this thesis is concerned with image mining.

Image mining is directed at the extraction of useful knowledge and relationships from within image sets. Large amounts of visual information, in the form of digital images, are generated on a daily basis with respect to many domains such as the remote sensing and medical domains. Extracting useful knowledge from within these images presents a significant challenge. Image mining also encompasses elements from fields such as image analysis and content based image retrieval.

The work described in this thesis is directed at image classification, as opposed to (say) image clustering. Image classification is a non-trivial problem, because of the typically complex structure of image data, and is still a very active field of research. In image classification, a collection of pre-classified (training) images are taken as input and used to construct (train) a classifier which can then be applied to unlabelled images. Image classification typically involves the pre-processing of collections of images into a format whereby established classification techniques may be applied. As with many data mining applications the main challenge in the pre-processing of image data is to produce a representation whereby no relevant information is lost while at the same time ensuring that the end result is succinct enough to allow for the application of effective data mining. In image mining this challenge is more acute because it is usually not clear what can be thrown away. In most cases it is not possible to pre-process the images in such a way that all pixel data, and the spatial relationships between pixels, can be retained; some decision regarding resolution needs to be made. One approach is to apply some form of segmentation to identify "blobs" (objects) within the images and then use these objects to form an *attribute set.*

Image classification can be conducted with respect to as much of the information contained in the images as possible, or can be focused on a particular object or objects (blob or blobs) that occur across the image set. In this thesis the latter is referred to as a Region Of Interest (ROI) and consequently the term ROI Based Image Classification (ROIBIC) is used to identify this type of image classification. The advantage offered is that the remainder of the image can be ignored and thus computational advantages gained. Consequently, the representation can be more detailed. The work described in this thesis is directed at ROIBIC.

The rest of this introductory chapter is organised as follows. The motivation for the work is presented in Section 1.1. The research objectives and associated research issues are presented in Section 1.2. The research methodology used to address the research issues, including the "criteria for success", is presented in Section 1.3. An overview of the rest of this thesis is then given in Section 1.5, and a summary of this chapter in Section 1.6.

1.1 Motivation

From the above, the research described in this thesis is directed at image classification, more specifically ROIBIC. Image classification, in whatever form, has many applications. However, an important focus for image mining research is with respect to medical applications. Global investment in the use of medical imaging technology, such as Computed Tomography (CT), Magnetic Resonance Imagery (MRI), Nuclear Medicine (NM) and MR Spectroscopy (MRS), has grown rapidly over the last decade. The quantity of medical image data that is being generated is fast becoming overwhelming, while at the same time there is a requirement for ever more sophisticated tools to assist in the analysis of this imagery. Consequently, medical image mining is attracting significant attention from both the commercial and the research communities.

Medical diagnosis is often founded on a categorization (classification) of medical images according to the nature of a specific object contained within such images rather than the entire image. Often the distinguishing features that would indicate a particular classification are difficult to observe even by trained clinicians. Therefore there is a necessity for content based image classification to classify these types of images according to the nature of a ROI contained within them. This is then the motivation for the work described in this thesis.

The principal challenge of ROIBIC is the capture of the features of interest in such a way that relative spatial information is retained. Some popular feature representations are directed at colour, texture and/or shape. Little work has been done on techniques that maintain the relative structure of the features of interest. The work described in this thesis is directed at medical image classification according to a particular feature of interest that appears across the image set. There are many medical studies [4, 27, 31, 34, 38, 61, 74, 98, 124, 128, 149, 151] that demonstrate that the shape and the size of specific regions of interest play a crucial role in the image classification process. One example (and the application focus of the work described) is that the shape of the corpus callosum, a prominent feature located in brain MRI scans, is influenced by neurological diseases such as epilepsy and autism, and by special abilities (such as mathematical or musical ability) [111, 132, 149]. Many studies have shown a correlation between the progression of Alzheimers disease (AD) and the decrease of volume in brain periventricular structures, such as the hippocampus and the amygdala [50, 147]. In [146], a voxel discriminant map classification method is described applied to brain ventricles in order to distinguish between healthy controls and Alzheimers disease (AD) patients based on the shape of brain ventricles. In [55] the clinical research problem of classifying the identical monozygotic and non-identical dizygotic twin pairs according to the shape and size of brain ventricles structures has been addressed.

In summary the work described is motivated by a need for techniques that can classify images according to the shape and relative size of features of interest that occur across some medical image sets. As noted above, one example is the classification of MRI brain scan data according to the nature of corpus callosum which features across those MRI brain scan collections.

1.2 Thesis Objectives

Given the motivation presented in the previous section, this thesis is targeted at an investigation of techniques to facilitate the analysis of medical images according to a ROI that may feature across such data sets. More specifically, the work described investigates techniques for classifying 2D MR images, extracted from 3D MRI brain volumes, according to the nature of a ROI within these scans. The research question to be addressed is thus how best to process image collections so that efficient and effective classification, according to some ROI contained across the image set, can be achieved. The techniques investigated assume that some appropriate ROI exists across the image set, thus the proposed techniques will not be applicable to all image classification problems, but the techniques will be applicable to the subset of problems where classification according to a ROI makes sense.

The above research question encompasses a number of research issues.

1. The techniques derived should serve to maximize classification accuracy while at the same time allowing for efficient processing (although efficient processing can be viewed as a secondary requirement to accuracy).
2. To achieve the desired classification accuracy any proposed feature extraction (representation) method should capture the salient elements of the ROI without knowing in advance what those salient elements might be. In other words any proposed feature extraction method, whatever form this might take, should retain as much relevant information as possible.
3. Not withstanding point 2 it is also desirable to conduct the classification in reasonable time, there is thus a trade off between accuracy and efficiency that must be addressed.
4. Not all potential representations are compatible with all available classification paradigms, thus different representations may require the application of different classification techniques.

1.3 Research Methodology

To address the above research objective and associated issues the adopted research methodology was to investigate and evaluate a series of techniques that could be applied to extract and process ROIs. Although there are a great variety of potential techniques that can be adopted for ROI representation this thesis focuses on four techniques as follows:

1. **Tree representations**: The representation of ROI in terms of quad-trees coupled with the application of a weighted frequent subgraph mining technique to identify frequently occurring subgraphs which can then be used as the input to a standard classification algorithm.
2. **Time series representations**: The representation of ROI as time series coupled with the application of a Case Based Reasoning (CBR) process to achieve the desired classification.
3. **Hough Transform**: The application of Hough transform methods to ROIs so as to extract a "signature" that encapsulates the desired details of the ROI which can then be used in conjunction with appropriate classification algorithms.
4. **Zernike Moments**: The representation of ROIs using Zernike moments so as to define a "signature", as in the case of (3), that both encapsulates details of the ROI and is compatible with appropriate classification algorithms.

The first two were selected because they were two very distinct techniques that have (to the best knowledge of the author) not been previously applied in the context of ROIBIC for MRI brain scan data. The third and fourth options were selected because, from the literature, the Hough transform and Zernike moments have frequently been applied in the context of image classification.

To facilitate the above an appropriate segmentation technique was required so as to isolate the desired ROI contained within a given input image collection. The investigation therefore commenced with the consideration of the nature of the segmentation techniques that might be required. This was then followed by consideration of the above four selected representations. To evaluate the effectiveness of each technique standard measures (classification accuracy, specificity, sensitivity and runtime) were used to assess the performance of the resulting classification. The aim was to identify the best performing technique. To support the evaluation a number of MRI brain scan data sets were used. In each case the proposed ROIBIC was directed at the classification of MRI brain scan data according to the nature of the corpus callosum (introduced above).

1.4 Contributions

The contributions of the research work presented in this thesis can be summarized as follows:

(a) A variation of the *multiscale normalized cuts algorithm* to achieve the desired segmentation and delineation of a ROI contained across an image data set.

(b) A novel approach to MR image classification based on the Hough transform coupled with a polygonal approximation. The aim of the application of the polygonal approximation to the ROI was to obtain a smooth curve over a minimum number of line segments describing the region boundary. The Hough transform was then used to extract (1D) image signatures.

(c) An effective approach to MR image classification based on a quad tree represented hierarchical decomposition coupled with a weighted frequent subgraph mining algorithm in order to identify frequently occurring subgraphs (subtrees) within the quad-tree representation. The identified frequent subtrees were viewed as defining a feature space which could be used to represent the image set.

(d) A novel mechanism to speed up the computation of exact Zernike Moments, also based on a quad-tree decomposition, and the usage of the resulting exact Zernike moments to define signatures for input to a classification system.

(e) An effective mechanism to describe ROIs in the form of a time series coupled with the use dynamic time warping to determine the similarity between images within the context of a CBR framework.

1.5 Thesis Organisation

The organisation of the rest of this thesis is as follows. Chapter 2 provides an extensive literature review on medical image classification systems and also discusses the challenges associated with 2D image segmentation to identify the desired ROIs. Chapter 3 describes the nature of the MRI brain scan datasets and the application domain used as the focus for the work described in this thesis and to evaluate the proposed techniques. The necessary data preparation and image pre-processing is also described in this chapter. The four techniques considered are then described in the following four chapters. Chapter 4 deals with image classification techniques using the Hough transform. A variation of the Hough transform that employs a polygonal approximation of the curves representing the regions of interest is proposed. Chapter 5 describes the tree based approach to image classification and an associated weighted frequent subgraph mining technique is used to identify frequently occurring "patterns". Chapter 6 presents the Zernike moments based signature representation ROIBIC technique and includes consideration of mechanisms for the fast computation of Zernike moments to enhance the accuracy and efficiency of the technique. In Chapter 7 the image classification framework based on a time series representation is described. The chapter includes discussion of a "dynamic time warping" similarity matching mechanism. Finally, in Chapter 8, this dissertation is concluded with a summary, presentation and discussion of the main findings, and some suggestions for future work.

1.6 Summary

This chapter has provided the necessary context and background to the research described in this thesis. In particular the motivation for the research and the thesis objectives have been detailed. A literature review of the related previous work, with respect to this thesis, is presented in the following chapter (Chapter 2).

Chapter 2

Background and Literature Review

2.1 Introduction

In this chapter a review of the background and previous work with respect to the research described in this thesis is presented. The chapter starts, Section 2.2, with a review of the MRI brain scan application domain. In Section 2.3 a brief review is then presented concerning image preprocessing, a necessary precursor to any image analysis process. Broadly the work described in this thesis falls within the domain of data mining, and more specifically image mining. Section 2.4 therefore introduced the concept of data mining and then goes on to consider, in more detail, the sub-domains of image mining and image classification. In particular the application of Case Based Reasoning (CBR) to the classification problem and frequent subgraph mining are discussed, because these are two of the techniques used (in part) to provide an answer to the research question central to this thesis (how best to process image collections so that efficient and effective classification, according to some ROI contained across the image set, can be achieved?).

One of the main issues associate with image classification is how best to represent the image input set so that an appropriate image mining technique can be applied. The nature of this representation is of course related to the nature of the image mining techniques to be adopted. A review of various representation techniques, that impact on the representations proposed in this thesis, is thus given in Section 2.5. A chapter summary is presented in Section 2.6.

2.2 Magnetic Resonance Imaging (MRI)

Magnetic Resonance Imaging (MRI) came into prominence in the 1970s. MRI is similar to Computerized Topography (CT) in that cross-sectional images are produced of some object. MRI uses a strong magnetic field and radio waves to produce high quality and detailed computerized images of the inside of some object. MRI is based on the principle of Nuclear Magnetic Resonance (NMR), a spectroscopic technique used by scientists to obtain microscopic chemical and physical information about molecules. The first successful Nuclear Magnetic Resonance (NMR) experiments were conducted in 1946 independently by two scientists, Felix Bloch and Edward Purcell, both of whom were awarded the Nobel Prize in 1952. In 1977, Raymond Damadian discovered the basis for using MRI as a tool for medical diagnosis and demonstrated the first MRI examination of a human subject [32]. The technique was called MRI rather than Nuclear Magnetic Resonance Imaging (NMRI) because of the negative connotations associated with the word nuclear in the late 1970's. MRI started out as a tomographic imaging technique, that is it produced an image of the NMR signal in a thin slice through the human body. Since then MRI has advanced beyond a tomographic imaging technique to a 3D imaging technique.

MRI is commonly used to examine the spine, joints, abdomen, and pelvis. A special kind of MRI exam, called Magnetic Resonance Angiography (MRA) can be used to examine blood vessels. MRI is also used for brain diagnosis, for example to detect abnormal changes in different parts of the brain. A MRI of the brain produces a very detailed picture. An example brain scan image is given in Figure 2.1.

As noted in the previous chapter the focus of the work described in this thesis is directed at the classification/categorisation of MRI brain scans according to a particular feature (ROI) within these scans, namely the corpus callosum. MRI brain scans underpin the diagnosis and management of patients suffering from various neurological and psychiatric conditions. Analysis of MRI data relies on the expertise of specialists (radiologists) and is therefore subjective. More specifically the focus of the work is the classification of MRI brain scan data according to a feature called the corpus callosum. Figure 2.2 gives an example midsagittal slice of a MRI scan, the corpus callosum is located in the centre of

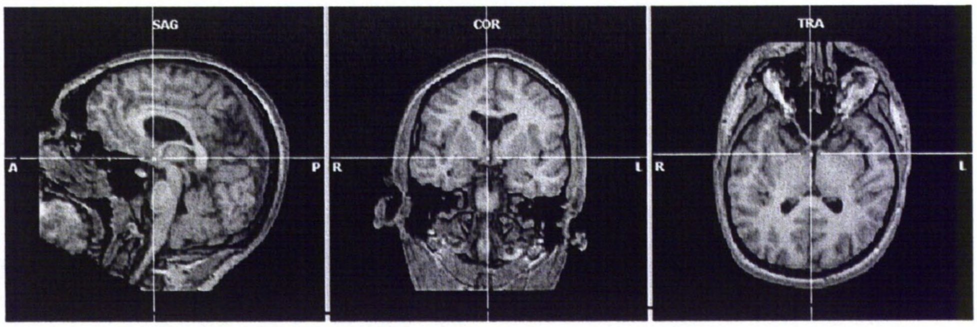

Figure 2.1: An example brain scan image. The three images show (from left to right) sagittal, coronal and axial planes. A common point is marked in each image.

the image. The *midsagittal slice* is the middle slice with a MRI scan, where a MRI scan comprised a sequence (or bundle) of "image slices".

The size and shape of the corpus callosum has been shown to be correlated to sex, age, neurodegenerative diseases (e.g. epilepsy, multiple sclerosis and schizophrenia) and various lateralized behaviour in people (such as handedness). It is also conjectured that the size and shape of the corpus callosum reflects certain human characteristics (such as a mathematical or musical ability). Within neuroimaging research considerable effort has been directed at quantifying parameters such as length, surface area and volume of structures in living adult brains, and investigating differences in these parameters between sample groups. Several studies indicate that the size and shape of the corpus callosum, in humans, is correlated to sex [4, 34, 128], age [128, 151], brain growth and degeneration [61, 98], handedness [31], epilepsy [27, 124, 149] and brain disfunction [38, 74]. It is worth noting that although the work described in this thesis is directed at MRI brain scan classification there are other features in MRI brain scans to which the techniques could be applied, such as the ventricles.

2.3 Image Preprocessing, Registration and Segmentation

The automated analysis of images, regardless of the nature of this analysis, typically requires some form of image pre-processing. This may include simple noise

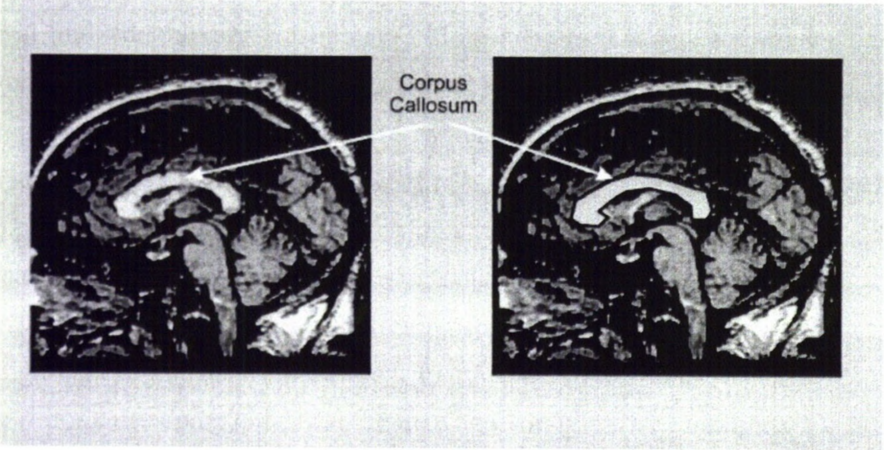

Figure 2.2: Midsagital MRI brain scan slice showing the corpus callosum (highlighted in the right-hand image).

removal and "deblurring" of objects. More advanced image preprocessing may require operations such as registration and segmentation.

Registration is the process where by one or more images are aligned with a reference image. This is important so that a collection of images can be effectively compared. Image registration is used in a range of application domains, such as medical image analysis (e.g. diagnosis), neuroscience (e.g. brain mapping), computer vision (e.g. stereo image matching for shape recovery), astrophysics (e.g. the alignment of images from different frequencies), etc. Image registration in the medical domain is particularly difficult when complex (e.g. nonlinear) geometric transformations are required to relate the images, e.g. when registering images of different human brains (multi-subject registration). Registration of medical image data sets can be defined as the problem of identifying a set of geometric transformations which map the coordinate system of one data set to that of the others. In the context of the work described in this thesis, image registration was undertaken to ensure that all brain MRI scans in a given collection conformed to a single set of coordinate axes. Therefore, all scans in the study have been aligned manually by trained physicians.

Image segmentation is defined as the partitioning of an image into non-overlapping meaningful regions that are homogeneous with respect to some characteristic such as intensity, colour or texture or by extracting one or more specific objects in images such as medical structures. Ideally a segmentation method finds the group of pixels that correspond to anatomical structures or regions of interest in the image, usually this is done by distinguish objects or regions of interest (the "foreground") from everything else (the "background"). In the simplest cases there are only two pixel types (foreground and background), consequently the segmentation results in a binary image. Segmentation is often the first stage in an image analysis process. Once the regions of interest are isolated from the rest of the image, certain characterizing measurements can be made and these can be used to (say) classify the regions.

Image segmentation has gone through many stages of development and refinement over the last few decades [108]. However, any individual image segmentation technique is not likely to achieve reliable results under all circumstances; there is no all purpose "best" segmentation technique. Medical image segmentation is a key task in many medical applications such as surgical planning, post-surgical assessment and abnormality detection. Segmentation is used, for example: (i) in the detection of organs such as the brain, heart, lungs or liver in MRI scans; and (ii) to distinguish pathological tissues, such as tumours, from normal tissue. The most basic attributes used to identify the ROI are image grey scale level or brightness, but other properties such as texture can be used. Medical images mostly contain complicated structures and precise segmentation is often deemed necessary for clinical diagnosis. A lot of methods for automatic and semi-automatic image segmentation fail to partition medical images precisely due to poor image contrast, inhomogeneity and weak boundaries between regions. This includes brain image segmentation. The segmentation of brain MRI scans is a challenging problem that has received much attention [118, 154].

A variety of artifacts (noise) may appear in MRI data. Since the artifacts change the appearance of the image they may also affect the performance of a segmentation algorithm. The most significant artifacts in image segmentation are intensity inhomogeneities and the partial volume effect. Intensity inhomogeneities are not always visible to the human eye, but can nonetheless have negative influence on automatic segmentation. This may manifest itself by making intensities in one part of the image brighter or darker than another part. It is often caused by the Radio Frequency (RF) coils used in the MRI acquisition process. The partial volume effect occurs when a pixel can not be accurately assigned to one tissue type. This is because the intensity of the pixel originates from more than one tissue. It occurs when one pixel covers a number of different tissue types and the collective signal emitted from these tissue cells makes up the detected intensity of the pixel. The partial volume effect is most apparent at edges between different tissues (regions).

Many image segmentation techniques are used in the context of brain MRI segmentation including pixel classification, deformable models, statistical models, fuzzy based approaches and graph based approaches. Each is discussed in the following sub-sections.

2.3.1 MRI Segmentation Using Pixel Classification

Pixel classification methods segment brain structures pixel by pixel based on spatial and appearance information, which are represented by pixel features. These pixel features can include pixel coordinates describing the location, as well as intensity values of filtered versions of MRI data that describe the appearance of the region of interest. In classification-based segmentation image pixels are represented as points in a high-dimensional space, in which the coordinate axes are defined by the feature values associated with the pixel (for example colour intensity). To segment an unlabelled target image using supervised classification techniques, first manually labelled example images are used to train a pixel classifier. This is done by first sampling pixels from the training images and mapping them to the feature space. In the feature space a decision boundary is then found that best separates the groups of pixels labelled as regions, from the pixels that were labelled as background in the examples. Different types of classifiers use different methods to derive this boundary from the training samples. After training, the classifier is applied to the unlabelled target pixels by mapping them into the feature space, and labelling them according to the decision boundary. The more pixel features that are used the better the classifier's ability to model the region's appearance and location. However, it also tends to increase the complexity of the decision boundary which increases the risk of over-training (where the classifier is over tuned to a particular training set) causing errors when classifying images that were not used for training. This risk can be decreased by increasing the number of examples, constraining the complexity of the decision boundary, or decreasing the number of features by ignoring those that are not considered relevant to the classification accuracy. The most important differences between brain structure segmentation methods based on pixel classification are the number and type of pixel features used. In Powell et al. [117] up to 100 features were employed, including the intensities of pixels and their direct neighbours. Morra et al. [104] segmented the hippocampus using thousands of features and the AdaBoost ensemble classification method [53].

2.3.2 MRI Segmentation Using Deformable Models

Methods based on the *deformable model* paradigm, such as the *active contour model*, also called *snakes*, delineate brain regions of interest by fitting a boundary model to the image, which incorporates some form of global shape knowledge. Using Snake and Level Sets the shape information is relatively weak, as these techniques merely enforce smooth boundaries [11]. Statistical shape models enforce stronger shape constraints and are therefore better equipped to deal with low-contrast boundaries. These models are constructed by parametrizing the shapes of manually labelled examples, and learning their mean shape and typical variations. Examples of shape models used for brain segmentation have been reported in [71, 80]. The most important difference between these methods is the flexibility of the parametrization. As a general rule, models with many degrees of freedom can describe a complex boundary, but also require more labelled examples to represent the potential shape variation. The initialization of the boundary offers a way to incorporate spatial information in a deformable model. Deformable models operate by minimizing a cost function that generally has several local minima. This usually ensures that the final result is close to the initialization and can therefore be used as a de-facto constraint on the spatial domain of the segmentation.

2.3.3 MRI Segmentation Using Statistical Models

Methods based on the statistical model paradigm pay attention to spatially intrinsic characteristics. The most popular stochastic model is the Markov Random Field (MRF) model [14]. The MRF model, and its variants, have been successfully used for brain MRI segmentation [138]. Ruan et al. proposed a fuzzy Markovian method for brain tissue segmentation from magnetic resonance images that calculated a fuzzy membership value for each pixel to indicate the partial volume degree [125].

In unsupervised statistical segmentation techniques the number of class labels and the model parameters are assumed to be unknown. Hence, estimations of model parameters and image labels (where each group of pixels characterizing a region of interest can be represented as an image label) are required simultaneously. Since, the image label estimation depends upon the optimal set of parameters, the segmentation problem can be viewed as an incomplete data problem. To handle this problem, an iterative scheme, the Expectation-Maximization (EM) algorithm, has been proposed [103]. Zhang et al. proposed a Hidden Markov Random Field (HMRF) model to achieve brain MRI segmentation in the case of unsupervised statistical techniques [169]. A new Bayesian method for automatic segmentation of brain MRI was proposed in [99] where a variant of the EM algorithm was used so as to make the whole procedure more computationally efficient.

2.3.4 MRI Segmentation Using Fuzzy Based Approaches

Fuzzy based segmentation approaches are increasing popular because of recent developments in fuzzy set theory, the development of various fuzzy set based mathematical modelling techniques, and its successful application in computer vision systems [139]. Ahmed et al. proposed a bias correction Fuzzy C-Means (FCM) segmentation algorithm in which they incorporated a neighbourhood regularizer into the FCM objective function to allow labelling of a pixel to be influenced by the labels in its immediate neighbourhood [3]. The algorithm is realized by incorporating the spatial neighbourhood information into the standard FCM algorithm and modifying the membership weighting of each cluster. Siyal et al. presented a modified FCM algorithm formulated by modifying the objective function of the standard FCM and used a special spread method for the classification of tissues [137]. Wang et al. proposed a modified FCM algorithm, called mFCM, for brain MR image segmentation [148]. Aboulella et al. proposed a statistical feature extraction technique for diagnosis of breast cancer mammograms by combining fuzzy image processing with rough set theory [65].

2.3.5 MRI Segmentation Using Graph Based Approaches

Recently, automatic segmentation of MR images of the developing new born brain has been addressed [118] using graph clustering and parameter estimation for finding the initial intensity distributions. Cocosco et al. [24] used sample selection through minimum spanning trees for intensity-based classification. Shi and Malik [135] proposed the Normalized Cuts (NCut) algorithm for image segmentation problems, which is based on Graph Theory. The NCut algorithm treats an image pixel as a node of a graph, and considers segmentation in terms of a graph partitioning problem. A variation of this technique is used in the context of the work described later in this thesis. Chapter 3 gives more details of this image segmentation technique.

Note that with respect to the work described in this thesis a necessary pre-cursor for the desired classification is the identification (segmentation) of the corpus callosum, although the precise nature of the adopted segmentation algorithm is not significant as its is the relative performance of the proposed representations with respect the classification task that is central to the investigation described in this thesis.

2.4 Data Mining and Image Classification

Data Mining is broadly concerned with the identification of hidden patterns in data. Data mining is part of a super process called Knowledge Discovery in Databases (KDD) [47, 48, 64] and draws on the fields of statistics, machine learning, pattern recognition and database management. Data mining first came to prominence in the early 1990s when advances in computing technology meant that large quantities of data could be effectively collected and stored, and subsequently analysed. However, we can trace the origins of data mining to much earlier work on machine learning and statistics [18, 48, 49, 64]. Originally data mining was directed at tabular data, for example the analysis of the contents of super market baskets [2]. Subsequently data mining techniques have been applied to many forms of data: examples include text [17], web usage logs [168], and graphs [72]. The work described in this thesis is directed at image mining.

Image mining deals with the extraction of implicit knowledge from image collections, for example image relationships or patterns, that are not explicitly stored in the image database. The main challenge of image mining is concerned with mechanisms to translate low-level pixel representations into high-level image objects that can be efficiently mined [69, 110, 114, 166, 167].

One branch of data mining, and that of interest with respect to the work described here, is classification (also sometimes referred to as categorisation). Classification is concerned with software systems to generate a "classifier" which can then be used to classify (categorise) new data. Typically a pre-labelled training set is used to build the classifier. Thus, in the case of the corpus callosum application; the training data will comprise a set of labelled images, (say) epilepsy and non-epilepsy, from which a classifier can be generated. This classifier can then be used to categorise new images. Thus the goal of image classification is to build a model that will be able to predict accurately the class of new, unseen images. There are various techniques that can be used to generate the desired classifier, examples include decision trees [122], Support Vector Machines (SVMs) [28], KNN [100] and Naive Bayes [95].

For the work described in this thesis, the popular C4.5 decision tree classifier [122] and SVMs [28] were adopted in Chapters (see 5 and 6). A C4.5 decision tree consists of internal nodes that specify tests on individual input variables or attributes that split the data into smaller subsets, and a series of leaf nodes assigning a class to each of the observations in the resulting segments. The C4.5 algorithm builds decision trees using the concept of information entropy [122]. The entropy of a sample S of classified observations is given by:

$$Entropy(S) = -p_1\, log_2(p1) - p_0\, log_2(p0), \tag{2.1}$$

where $p_1(p_0)$ are the proportions of the class values 1(0) in the sample S, respectively. C4.5 examines the normalised information gain (entropy difference) that results from choosing an attribute for splitting the data. The attribute with the highest normalised information gain is the one used to make the decision. The algorithm then recurs on the smaller subsets.

Support Vector Machines (SVMs) have proved to be a useful technique for data classification. SVMs have provided improvements in the fields of handwritten digit recognition, object recognition and text categorization, among others. SVMs try to map the original training data into a higher dimensional space by a kernel function Φ. The aim is then to identify a linear separating hyper-plane, with the maximal margin between negative and positive samples, in this higher dimensional space. From the mathematical point of view, given a training set of instance label pairs (x_i, y_i); $i = 1 \cdots l$, where $x_i \in R^n$ and $y \in \{-1, 1\}^l$, SVMs search for a solution to the following optimization problem:

$$\begin{aligned} & \min_{w,b,\xi} \frac{1}{2} w^T w + C \sum_{i=1}^{l} \xi_i \\ subject\, to: \ & y_i(w^T \Phi(x_i) + b) \geq 1 - \xi_i; \ \xi_i > 0 \end{aligned} \tag{2.2}$$

Here training vectors x_i are mapped into the higher dimensional space by the function Φ. $C > 0$ is the penalty parameter of the error term. Furthermore, $K(x_i, x_j) \equiv \Phi(x_i)^T \Phi(x_j)$ is the kernel function. There are four basic kernel functions: linear, polynomial, radial basis and sigmoid functions. SVMs are able to deal with two-class problems, but there exists many strategies to allow SVMs work with a larger number of categories.

The automatic categorization of medical images is a challenging task that can be of importance when managing real data collections. More specifically, because of the increasing amount of medical image data available, locating relevant information in an efficient way presents a particular challenge. Moreover, the extraction of appropriate visual descriptors to reduce the gap between the semantic interpretation and the visual content of medical images remains a research issue [106].

There has been a substantial amount of work on the application of classification techniques within the medical domain. For example, Antonie et al. [161] distinguished mammography tumours from the normal mammography using a medical image classification approach. Many successful techniques for automatic categorization of medical images rely on the same kind of feature space descriptors as more general methods for generic image classification. For example, Avni et al. [7] have successfully applied a Bag-of-Features (BoF) approach to the classification of X-Ray images. Their method uses histograms of vector quantized scale invariant features for automatic organ recognition. Their Scale Invariant Feature Transform (SIFT) technique computes a 128-bin gradient histogram as a description vector for each salient region [96]. They have also applied their method to discriminate between healthy and pathologic cases on a set of chest radiography images. SIFT descriptors and the BoF representation have also been successfully applied to binary classification problems related to endomicroscopic images, thus enabling users to discriminate between neoplastic and benign cases with high accuracy [5]. Another tool for feature extraction in medical image retrieval and classification is the Local Binary Patterns (LBP) descriptor [109]. This descriptor is based on a very simple idea to efficiently describe the local texture pattern around a pixel. LBP comprises a binary code that is obtained by thresholding a neighbourhood according to the grey value of its centre. The effectiveness of LBP for radiographic images has been recently demonstrated by Jeanne et al. [78], who have found significant performance improvement over other common visual descriptors. In the context of MRI scan classification, Yang et al. [157] proposed an automatic categorization of brain MRI scans based on Independent Component Analysis (ICA) coupled with an SVM technique to discriminate MRI scans among Alzheimer patients, mild cognitive impairment, and control subjects using whole brain images. In [83], a hybrid approach combines an SVM technique and Genetic Algorithm (GA) to classify tumour and normal tissue of brain MRI scans based on wavelet descriptors.

2.4.1 Case Based Reasoning

Case-Based Reasoning (CBR) is a well established Artificial Intelligence (AI). CBR operates by using a Case Base (CB) of previous cases to solve a new case. Essentially the features of the new case are compared with the features of the cases in the CB and the identified most similar cases are used to formulate a solution to the new case. Thus the basic idea behind CBR is to solve a current problem by reusing solutions that have been applied to similar problems in the past. At the highest level of generality, the CBR cycle may be described by four tasks [1]: (i) retrieve the most similar case or cases, (ii) reuse the information and knowledge in the retrieved cases to solve the problem, (iii) generate a solution, and (iv) retain in the CB the parts of this experience likely to be useful for future problem solving. In order to do the retrieval, case representation and case indexing techniques are required so that it is possible to retrieve cases using a similarity computation. The retrieved cases are then reused to provide a possible solution to the given problem and therefore, a case adaptation mechanism is also required.

CBR is not normally thought of as a data mining technique. However, if we think of a case base (CB) as comprising a set of examples each with an associated label then CBR can be used for classification purposes. CBR style systems have been applied successfully in the context of classification. For example Nearest-Neighbour Classification (NNC) systems [100] can be characterised as a simple CBR technique. As noted above the goal of classification is to predict the class membership of given entities. The basic idea of NNC is to use information about records (cases) for which the class membership is already known. In order to classify a new record (case), its description has to be compared to the descriptions of the known records. From an abstract point of view, each record can be characterised as a point in some problem space defined by the properties used to describe the record (see Figure 2.3). To predict the class of the new record its nearest neighbours within the problem space is identified using some distance metric. Finally, the information about the class membership of these nearest neighbours is used to predict the class the new record. Either the class of the actual nearest neighbour may be used or a weighted voting system may be adopted where k nearest neighbours have been identified. In the example shown in Figure 2.3 the entities belong either to the class "+" or "-". Using a 5-NNC the prediction for the shown query would be that it belongs to class "+", because 3 of the 5 nearest neighbours belong to this class. From the CBR point of view it is obvious that this approach requires no sophisticated adaptation methods as long as the number of cases exceeds the number of possible classes significantly. Excellent reviews of the foundations of CBR techniques, systems and tools can be found in [1] and [136].

In the context of CBR based image classification the main issue is the similarity matching technique to be adopted; given a case to be classified how best

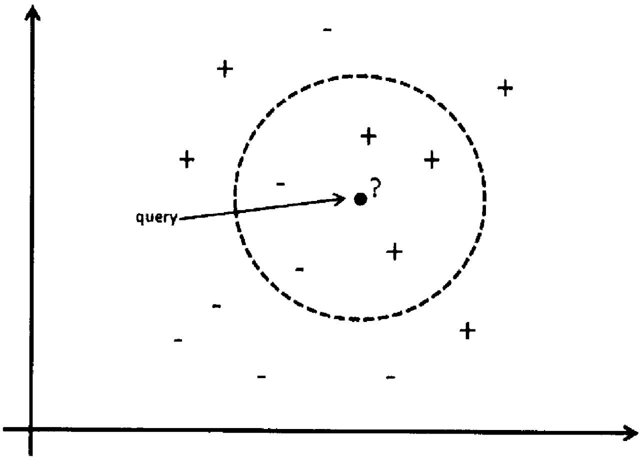

Figure 2.3: An example of 5-Nearest Neighbour Classification.

can this be matched with cases in the CB. The traditional measures used to compare cases in CBR are distance measures (assuming of course that we are only considering numerical attributes). Popular examples of such distance measures are: Minkowsky distance, Hausdroff Distance, Bottleneck Distance and Reflection Distance [143]. In the case of the work described here a Dynamic Time Warping (DTW) technique has been adopted, this is described further in Chapter 7.

2.4.2 Graph Mining

Graph mining is the process of discovering hidden patterns (frequent subgraphs) within graph datasets. From the literature graph mining can be categorized in terms of transaction graph mining and single graph mining. In transaction graph mining the dataset to be mined comprises a collection of small graphs (transactions). The goal is to discover frequent recurring subgraphs across the dataset. In single graph mining the input of the mining task is one single large graph, and the objective is to find frequent subgraphs which occur within this single graph. Frequent Subgraph Mining (FSM) has demonstrated its advantages with respect to various tasks such as chemical compound analysis [73], document image clustering [13], graph indexing [156], etc.

The straightforward idea behind FSM is to "grow" candidate subgraphs in either a Breadth First Search (BFS) or Depth First Search (DFS) manner (candidate generation), and then determine if the identified candidate subgraphs occur frequently enough in the graph data for them to be considered interesting (support counting). The two main research issues in FSM are thus how to efficiently and effectively: (i) generate the candidate frequent subgraphs and (ii) determine the frequency of occurrence of the generated subgraphs. Effective candidate subgraph generation requires that the generation of duplicate or superfluous candidates is avoided. Occurrence counting requires repeated comparison of candidate subgraphs with subgraphs in the input data, a process known as subgraph isomorphism checking. FSM, in many respects, can be viewed as an extension of Frequent Itemset Mining (FIM) popularised in the context of Association Rule Mining (ARM). Consequently, many of the proposed solutions to addressing the main research issues effecting FSM are based on similar techniques found in the domain of FIM.

It is widely accepted that FSM techniques can be divided into two categories: (i) the Apriori-based approach (also called the BFS strategy based approach) and (ii) the pattern growth approach. These two categories are similar in spirit to counterparts found in ARM, namely the Apriori algorithm [2] and the FP-growth algorithm [63] respectively. The Apriori-based approach proceeds in a "generate-and-test" manner using a BFS strategy to explore the subgraph lattice of the given database. Therefore, before exploring any $(k+1)$-subgraphs, all the k-subgraphs should first be explored. For each discovered subgraph g, this approach extends g recursively until all the frequent supergraphs of g are discovered [62]. Pattern growth approaches can use both BFS and DFS strategies, but the latter is preferable to the former because it requires less memory usage.

One of the main challenges associate with FIM and FSM is the substantial number of patterns which can be mined from the underlying database. This problem is particularly important in the case of graphs since the size of the output can be extremely large.

The significance of FSM with respect to the work described here is that one of the techniques proposed uses this technique for the purpose of generating a feature space. The application of FSM algorithms to the datasets described in this work entails a significant computational overhead because of the great number of generated frequent subgraphs. To reduce this overhead a Weighted

FSM approach can be applied, the objective being to focus on the identification of those frequent subgraphs that are likely to be the most significant according to some weighting scheme.

2.5 Image Representation

As noted above, image representation is an important issue with respect to image classification. It is currently not computationally possible to present images to a classification algorithm in their entirety, consequently it is necessary to process the images in such a way that the classification process is tractable while at the same time minimising information loss. Thus, one of the fundamental challenges of image mining is to determine how the low-level pixel representation contained in a raw image or image sequence can be efficiently and effectively processed to identify high-level spatial ROIs and their relationships. Image classification techniques use visual contents such as colour, texture, and shape to represent and classify images. Colour and texture have been explored more thoroughly than shape. Because shape is a more intrinsic property of ROIs than colour or texture, and given the considerable evidence that natural ROIs are recognized based primarily on their shape [107], the increasing interest in using the shape features of ROIs for image classification is not surprising. The focus of this research is therefore on shape-based image classification. Since humans can often recognize the characteristics of ROIs using only their shapes, it is possible to expect shape-based techniques to be intuitive as a tool for classifying images. However, image classification by shape is still considered to be a more intrinsically difficult task compared to image classification based on other visual features [107]. In addition, the problem of shape-based image classification becomes more complex when the extracted ROIs are corrupted by occlusions or noise as a result of the image segmentation process.

Deriving shape descriptions is an important task in image classification. Once the ROI has been acquired in the image, a set of techniques can be applied in order to extract information from its shape, so that it can be analysed further. This process is called shape description and generally results in a feature vector (a shape descriptor). Shape description can be viewed as a mapping from a shape space to a vector space that satisfies the requirement that two similar shapes will also have close-to-identical shape descriptors while still allowing for discrimination between different shapes. Note that it is not a requirement that the original shape can be reconstructed from the feature vector. In most studies, the terms shape representation and description are used interchangeably. Since some of the representation methods are used as shape descriptors, there is no well-defined separation between shape representation techniques and shape description techniques. However, shape representation and description methods are defined in [93] as follows. Shape representation results in non-numeric values of the original shape. Shape description results in numeric values and is a step subsequent to shape representation. For the sake of simplicity, we consider representation and description to be synonymous and, throughout the rest of this section, collectively refer to such techniques as shape description methods.

During the last decade, significant progress has been made with respect to both the theoretical and practical aspects of shape description, and the literature reports a variety of techniques directed at describing ROIs based on their shape. Two main approaches to deriving shape descriptors are region-based and boundary-based (also known as the contour-based approach). In the region-based approach, all the pixels defining a ROI are used in order to obtain the desired shape descriptors (vectors). On the other hand, the boundary-based descriptor approach uses only the boundary of a ROI to extract its shape descriptor. The two approaches are considered in more detail in subsection 2.5.1 and 2.5.2 below. The representations proposed in this thesis include both region based and boundary based descriptions.

The problem of shape analysis has been pursued by many authors, thus, resulting in a great amount of research. Recent review papers [93, 165] as well as books [29, 41] provide a good overviews of the subject.

2.5.1 Region Based Methods

Region based shape descriptors express the pixel distribution within a 2D ROI. They can be used to describe complex ROIs consisting of multiple disconnected regions as well as simple ROIs with or without holes. Since it is based on the regional property of a ROI, the descriptor is insensitive to noise that may be introduced inevitably in the process of segmentation. From the literature we can identify a number of techniques for generating region based shape descriptors, examples include: (i) moments, (ii) simple scalar descriptors, (iii) angular radial transformation descriptors, (iv) generic Fourier descriptors, (v) grid descriptors, (vi) shape decomposition and (vii) medial axis transforms. A number of these techniques form the foundation for some of the representations formulated later in this thesis. Others have been included for consideration in this sub-section purely for comparison purposes or because they are of historical interest.

2.5.1.1 Moments

Moments are widely used as shape descriptors. These moments can be classified as being either orthogonal or non-orthogonal according to the basis used to derive them. The most popular type of moments are called geometric moments which are non-orthogonal moments that use a power basis $(x^p y^q)$. The geometric moment m_{pq} of order $p+q$ of an $(N \times M)$ digital image $f(x,y)$ is defined as:

$$m_{pq} = \sum_{x=0}^{M-1} \sum_{y=0}^{N-1} x^p y^q f(x,y) \tag{2.3}$$

The use of moments for shape description was initiated in [70], where it was proved that moment-based shape description is information preserving. The zeroth order moment m_{00} is equal to the shape area assuming that $f(x,y)$ is a silhouette function with value one within the shape and zero outside the shape. First order moments can be used to compute the coordinates of the center of mass as $x_c = m_{10}/m_{00}$ and $y_c = m_{01}/m_{00}$. Based on the moments formulated in equation 2.3, a number of functions can be defined that are invariant under certain transformations such as translation, scaling and rotation. The moment invariants are then put into a feature vector. Global object features such as area, circularity, eccentricity, compactness, major axis orientation, Euler number and algebraic moments can all be used for shape description [120].

Central moments are constructed by subtracting the centroid from all the coordinates. These moments are represented as:

$$\mu_{pq} = \sum_{x=0}^{M-1} \sum_{y=0}^{N-1} (x - x_c)^p (y - y_c)^q f(x,y) \tag{2.4}$$

The disadvantage of using these moments is that the basis used to derive these moments is not orthogonal, so these moments suffer from a high degree of information redundancy. A generalization of moment transforms to other basis is also possible by replacing a conventional basis $x^p y^q$ by a form $P_p(x)\,P_q(y)$, for example orthogonal polynomials. In this case, the moments produce minimal information redundancy, which is important for optimal utilization of the information available in a given number of moments [93]. Some of the orthogonal polynomial systems include Legendre and Zernike polynomials [141]. Teague [141] adopt Zernike orthogonal polynomials to derive a set of invariant moments, called Zernike moments. Zernike moments are defined as the projections of $f(x,y)$ on complex Zernike polynomials which form a complete orthogonal set over only the interior of the unit circle; that is, $x^2+y^2 \leq 1$. The function of complex Zernike moments with an order p and repetition q in polar coordinates is defined as:

$$ZM_{pq} = \frac{p+1}{\pi} \int_0^{2\pi} \int_0^1 f(r,\theta).V_{pq}^*(r,\theta).\,r\,dr\,d\theta \tag{2.5}$$

$V_{pq}(r,\theta)$ is the Zernike polynomial, defined as:

$$V_{pq}(r,\theta) = R_{pq}(r).e^{iq\theta}, \quad i = \sqrt{-1} \tag{2.6}$$

where p is a positive integer or zero and q is a positive integer subject to the constraints that $p-|q|$ is even and $q \leq p$, r is the length of the vector from the origin to the (x,y) pixel; i.e.,$r = \sqrt{x^2+y^2}$, θ is the angle between the vector r and the x axis in a counter-clockwise direction, the symbol $(*)$ denotes the complex conjugate, and $R_{pq}(r)$ is a real-valued Zernike-radial polynomial defined as follows:

$$R_{pq}(r) = \sum_{k=0}^{p-|q|/2} (-1)^k.\frac{(p-k)!}{k!\left(\frac{p+|q|}{2}-k\right)!\left(\frac{p-|q|}{2}-k\right)!}.r^{p-2k} \tag{2.7}$$

Many researchers have adopted Zernike moments for many applications, such as character recognition [15], face recognition [10], and shape retrieval [81]. Zernike moment invariants have been shown to outperform several other shape descriptors and to be highly effective in terms of image representation [85, 164]. Teh and Chin [123] evaluated the performance of several moments with respect to issues such as representation ability, noise sensitivity, and information redundancy. In terms of overall performance, Teh and Chin showed that Zernike moments outperform geometrical and Legendre moments. Further details about Zernike moments will presented in Chapter 6 as this is the foundation of one of the representations considered in this thesis.

2.5.1.2 Simple Scalar Descriptors

A shape can be described using scalar measures based on its simple geometric characteristics. These simple descriptors of a shape can often discriminate only between shapes with large dissimilarities; therefore, they are usually used in the context of image classification to act as filters to eliminate false hits or are combined with other techniques to differentiate shapes. The advantage of these descriptors is that they have a physical meaning. A brief description of the most commonly used simple global descriptors is given below.

Eccentricity: Eccentricity (E) has been widely used as a scalar descriptor. It illustrates the way in which the pixels of a ROI are scattered around the centre of the ROI. E is defined as the ratio of the major axis of the ROI to the minor axis. It is calculated using central moments such that [153]:

$$E = \frac{\mu_{20} + \mu_{02} + \sqrt{\mu_{20}^2 + \mu_{02}^2 - 2\mu_{02}\mu_{20} + 4\mu_{11}^2}}{\mu_{20} + \mu_{02} - \sqrt{\mu_{20}^2 + \mu_{02}^2 - 2\mu_{02}\mu_{20} + 4\mu_{11}^2}} \tag{2.8}$$

where μ_{pq} are the central moments of order $(p+q)$.

Solidity: Solidity (S) is computed as the ratio between the ROI area A_0 and the area of the corresponding convex hull. Solidity is computed as follows [153]:

$$S = \frac{A_0}{Convex\ Area} \tag{2.9}$$

Extent (Rectangularity): Extent (EX) is a measure that reflects the rectangularity of a ROI [21], in other words, how much of a ROI fills its minimum enclosing rectangle (MER). Extent is defined as:

$$EX = \frac{A_0}{A_{MER}} \tag{2.10}$$

where A_{MER} is the area of the ROI's MER.

Circularity (Compactness): Circularity (C) is a measure of roundness and is defined as follows:

$$C = \frac{4\pi * A_0}{(P_0)^2} \tag{2.11}$$

where A_0 is the ROI area, and P_0 is the ROI perimeter.

It is sometimes used as inverse formula $C = \frac{(P_0)^2}{4\pi * A_0}$.

Euler's Number: Euler's Number is the difference between the number of contiguous parts and the number of holes in the ROI.

Elongatedness: Elongatedness is the ratio between the length and width of the region bounding rectangle.

2.5.1.3 Angular Radial Transform Descriptors

For region-based shape descriptions, the MPEG-7 working group has selected angular radial transform descriptors [19] as MPEG-7 region based shape descriptor. Angular radial transform (ART) descriptors are similar to Zernike moments descriptors. The main difference is that ART descriptors are based on cosine functions rather than on Zernike polynomials. The ART basis functions are separable along the angular and radial directions and are defined on the unit circle as follows [19]:

$$V_{pq}(x,y) = V_{pq}(r,\theta) = \frac{1}{2\pi} R_p(r) e^{iq\theta} \qquad (2.12)$$

The complex ART descriptors of order p with repetition q for a continuous function $f(x,y)$ are defined in polar coordinates as:

$$ART_{pq} = \frac{1}{2\pi} \int_0^{\pi} \int_0^{1} f(r,\theta).R_p(r).e^{-iq\theta}\, r\, dr\, d\theta \qquad (2.13)$$

where

$$R_p(r) = \begin{cases} 1 & p = 0 \\ 2cos(p\pi r) & p \neq 0 \end{cases} \qquad (2.14)$$

For a digital image, the integrals are replaced by summations to obtain:

$$ART_{pq} = \frac{1}{2\pi} \sum_r \sum_\theta f(rcos\theta, rsin\theta).R_p(r).e^{-iq\theta}\, r\, dr\, d\theta \quad , \quad r \leq 1 \qquad (2.15)$$

One of the advantages of the ART method is the compactness and efficiency in describing the properties of multiple disjoint regions, simultaneously. It describes the ROIs that may be split into disconnected sub-regions in the segmentation process. It has been reported that Zernike moments outperform angular radial transform descriptors in classifying ROIs that can be classified based on their contours, but that ART descriptors perform better in the case of complex ROIs, i.e., ROIs that consist of multiple contours, which can be classified only by region-based techniques [101].

2.5.1.4 Generic Fourier Descriptors

A one-dimensional Fourier transform has been used successfully in image analysis to derive shape descriptors from shape contours. Zhang and Lu [163] adopted the 2D Fourier transform to derive a set of invariant descriptors called Generic Fourier descriptors (GFD). In this method, the 2D ROI is transformed to the polar coordinates, and the 2D Fourier transform is then applied in order to derive shape descriptors. The rotation of the original ROI corresponds to a shift in the normal Cartesian coordinates. This property makes it possible to derive rotation invariant features by applying the 2D Fourier transform on the polar image and then taking the magnitude while ignoring the phase. The 2D Fourier transform of a polar image is give by [163]:

$$GFD(\rho, \phi) = \sum_{r} \sum_{i} f(r, \theta_i) e^{-j2\pi\left(\frac{r}{R}\rho + \frac{2\pi i}{T}\phi\right)} \tag{2.16}$$

where $0 \leq r = \sqrt{(x - x_c)^2 + (y - y_c)^2} < R$ and $\theta_i = i(2\pi/T), (0 \leq i < T)$; (x_c, y_c) is the center of mass of the ROI; $0 \leq \rho < R, 0 \leq \phi < T$. R and T are the radial and angular resolutions.

The experiments conducted by Zhang and Lu [163] showed that GFD outperformed the use of ZM in retrieving ROIs based on the content of a region. Li and Lee [91] proposed a technique which utilizes the magnitude of the Fourier transform as well as phase coefficients in order to derive a set of invariant features.

2.5.1.5 Fourier-Mellin Descriptors

The Fourier-Mellin transform takes advantage of the properties of the Fourier and Mellin transforms in order to define a new set of image invariants called Fourier-Mellin Descriptors (FMDs). The Fourier-Mellin transform for $f(r, \theta)$ is defined as follows [133]:

$$FM_{sl} = \frac{1}{2\pi} \int_{-\pi}^{\pi} \int_{0}^{\infty} r^{s-1} . f(r, \theta) . e^{-jl\theta} \, r \, dr \, d\theta \tag{2.17}$$

This transformation shows a radial-Mellin transform with parameter s and an explicit circular-Fourier transform with parameter l [133]. The rotation invariant can be achieved by taking the magnitude of the transform. Translation invariance is conventionally achieved by placing the origin of the coordinates at the image centroid.

Sheng and Duvernoy [133] employed the Mellin transform and the angular Fourier complex componential factor to drive invariant Fourier-Mellin descriptors. The problem associated with Fourier-Mellin descriptors is that the kernel function of the Mellin transform is not orthogonal; hence, these invariants suffer from a high degree of information redundancy. To overcome this problem, Sheng and Shen [134] applied the Gram-Schmidt orthogonalization process to orthogonalize the kernel function of the Mellin transform and used the resultant orthogonal polynomial to derive a set of orthogonal Fourier-Mellin moments. Their experiments demonstrated that, for small images, the description produced by orthogonal Fourier-Mellin moments is better than that produced by Zernike moments in terms of image-reconstruction errors and signal-to-noise ratio.

2.5.1.6 Grid Descriptors

The grid-based method has attracted interest because of its simplicity with respect to representations [97]. In this technique, the given ROI is overlaid by a grid space of a fixed size. A value of one is assigned to cells if they are at least 15% covered, and a zero is assigned to each of the other cells [97]. Then the 1s and 0s are scanned from left to right and top to bottom to obtain a binary sequence for the ROI. It is also evident that the smaller the cell size, the more accurate the representation of the ROI, but the greater the storage and computation requirements. It is evident that the representation is translation invariant, but it is not invariant to scale and rotation. Rotation and scale normalization are thus necessary when grid descriptors are used to compare two ROIs. To achieve scale normalization, all ROIs are scaled proportionally so that the major axes have the same fixed length. For rotation invariance, the given ROI is rotated so that its major axis is in parallel with the x-axis. The key problem associated with grid descriptors is the problematic major axis normalization. The major axis is sensitive to noise and can be unreliable even in the absence of noise effects. Moreover, online classification usually involves extremely complex computations due to the high degree of dimensionality of the feature vectors.

2.5.1.7 Shape Decomposition

This approach assumes that shape description is a hierarchical process and decomposes a ROI into a union of primitives that comprise the simplest elements which form the region. Given the decomposition, a graph representation is constructed. Syntactic pattern recognition techniques are, then, applied. Shape decomposition methods generally use mathematical morphology. A morphological shape decomposition technique is proposed in [116] where the binary ROIs are decomposed into a union of simple regions. A structuring element (disk) is defined as the simplest ROI component and the image is analysed as a union of the disks. The representation is shown to be unique and invariant under rotation, translation and scaling. Another morphological decomposition method, which is called Morphological Signature Transform (MST) was developed in [94]. The MST method utilizes multiresolution morphological image processing by multiple structuring elements. The idea of this approach is to process decomposed, multiple shapes instead of the original one. The decomposed shapes, called signature shapes, contain substantial information about the whole shape. The method calculates the area of the shape signatures obtained from multiple structuring elements and multiple ROI scales to generate shape descriptors. Multiple structuring elements are obtained by rotating single or multiple structuring elements. One of the earliest types of shape decomposition of image data is the quad-tree [92]. It is a tree-like representation of image data, where the image is recursively divided into smaller regions. A quad-tree is a tree data structure in which each internal node has exactly four children. The quad-tree decomposition is based on a recursive subdivision of the image block into four quadrants according to the complexity of the block. If a subimage is not a homogeneous block, it is subdivided into four equal sized subimages again until all the subimages are homogeneous blocks. A subimage is called a homogeneous block if the grey-level of each of the pixels in the block is the same with respect to some specified constant. More details concerning the quad-tree representation coupled with weighted frequent subgraph mining is given in Chapter 5.

One of the problems in shape decomposition is the definition of the components. The result of the decomposition does not always correspond to a human intuitive shape representation. Furthermore, the results are not always unique. The decomposition of similar shapes may result in different elements. In many cases, the derivation of the decomposition is rather tedious and the computational complexity is relatively high compared to the other region based shape description methods such as ART and moments.

2.5.1.8 Medial Axis Transform

The idea of the Medial Axis Transform (MAT) is to represent the shape by a graph in which the important shape features are preserved [35]. The shape graph is based on the region skeleton and the first step is the skeleton construction. The skeleton is the set of all region points, which have the same minimum distance from the region boundary for at least two separate boundary points. Generally, MAT techniques use the region of the shape skeleton in order to derive shape descriptors. The idea behind obtaining the skeleton of the region of a shape is to preserve the topological information of the shape and to eliminate redundant information. In other words, the skeletonization extracts a region-based shape feature that represents the general form of a ROI. The shape's skeleton can be obtained by several techniques such as thinning algorithms, mathematical morphologic-based algorithms, and distance map-based algorithms [59]. After skeletonization, the skeleton is decomposed into parts and represented as a graph. Matching shapes then becomes a graph-matching problem. The difficulty with skeleton-based techniques is that a small amount of noise or a variation in the boundary often generates redundant skeleton branches that may seriously disturb the topology of the skeleton's graph [9]. Therefore, one of the weaknesses in the medial axis transform is its sensitivity to noise in the shape boundary.

2.5.2 Boundary Based Methods

Boundary based shape description methods exploit only shape boundary information. The shape properties of a ROI boundary are crucial to human perception in judging shape similarity and recognition. Many authors who have studied the human visual perception systems, agree on the significance of high curvature points of the shape boundary in visual perception [6]. In the psychological experiments, it is suggested that corners have high information content and, for the purpose of shape description, corners are used as points of high curvature. Therefore, the shape boundary contains more information than the shape interior, in terms of perception.

The previous sections have provided a review of several descriptors that are based on the internal content of the shape. However, in many applications, the internal content of the shape is not as important as its boundary. Boundary-based techniques tend to be more efficient for handling shapes that are described according to their contours [101]. From the literature we can identify a number of techniques for generating boundary based shape descriptors, examples include: (i) polygonal approximation, (ii) Hough transform, (iii) stochastic representation, (iv) boundary approximation, (v) Fourier descriptors, (vi) coding, (vii) Curvature Scale Space Descriptors and (viii) simple boundary descriptors. Each is discussed in further detail below.

2.5.2.1 Polygon Approximation

Polygon approximation is one of the most popular shape representation methods, where the continuous shape is represented by a set of vertices of a polygon [93]. The main idea is to eliminate the redundant and insignificant shape features by reducing the number of boundary points. This is performed by searching the break points on the boundary, based on an approximation criteria, such as minimal error, minimal polygon perimeter or maximal internal polygon area. One of the most widely used polygonal approximation algorithm is a heuristic method called the Douglas-Peucker algorithm [37]. This iterative procedure repeatedly splits the curve into smaller and smaller curves until the maximum of the perpendicular distances of the points on the curve from the line segment is smaller than the error tolerance ϵ. In the approaches which use the split and merge algorithm [113], where the curve is split into segments until some acceptable error is reached, the split segments are merged if the resulting segment approximates the curve within some maximum error. In [88] curve evolution is used as a polygonal approximation method. Curve evolution reduces the influence of noise and simplifies the shapes by removing the irrelevant features, keeping relevant ones. In

this method, a digital curve is regarded as a polygon, where each boundary point is assumed to be a vertex, at the beginning of the evolution. In every evolution step, a pair of consecutive line segments is substituted with a line segment, joining the end points. The evolution process halts when the difference between the evolved polygon and the original curve is higher than a given threshold. Curve evolution methods assume that the shape boundary consists of various sources of distortion, which should be removed by smoothing. The process of smoothing depends on the predefined threshold value, which halts the evolution.
Corner detection is another approach for polygonal approximation. Popular techniques for corner detection use Wavelet Transform Modulus Maxima (WTMM) [121]. First, the shape boundary is represented by a 1D signal such as the contour's orientation profile. The singularities on that signal are then detected by determining the local maxima of the wavelet transform of the signal.

2.5.2.2 Hough Transform

The Hough Transform (HT) is a widespread technique in image analysis. Its main idea is to transform the image to a parameter space where clusters or particular configurations identify instances of a shape under detection. HT based techniques are used for shape detection, either parametrized or generalized. The HT was first introduced by Paul Hough in 1962 [67] with the aim of detecting alignments in T.V. lines. It became later the basis of a great number of image analysis applications. The HT is mainly used to detect parametric shapes in images. It was first used to detect straight lines and later extended to other parametric models such as circles or ellipses, being finally generalized to any parametric shape [12].

One major advantage offered by the HT is that it is highly robust against image noise and degradation. The HT is used for extracting *shape signatures* which can be used as a feature vector in the classification process. The HT is suitable for this task because it maintains the spatial information associated with an image ROI (feature). The "classic" HT performs a mapping between the X-Y image space onto a $\rho - \theta$ space. The transformation is $\rho = xcos\theta + ysin\theta$, where (x, y) are the coordinates of the pixel to be transformed, and (ρ, θ) are the parameters of a corresponding line passing through the pixel. The parameter space is suitably quantized into bins and represented by means of an accumulator matrix initially set to zeros. Each pixel (x, y) can be conceptualised as a sinusoidal (parametric) curve in the new $\rho - \theta$ space,where θ varies from the minimum to the maximum values, giving the corresponding ρ values. The corresponding sinusoidal positions can be stored in an accumulator matrix A, where each row corresponds to one value of ρ, and each column to one value of θ. The cells in A are then incremented by the parametric curve. The local maxima within A then correspond to the dominant boundary lines of the ROI. Further details about the HT are presented in Chapter 4.

2.5.2.3 Stochastic Representation

stochastic representation methods are based on the stochastic modelling of a one dimensional function obtained from the shape boundary [93]. The idea is to interpret the one dimensional function as a stochastic process realization and use the model parameters obtained by estimation, as shape descriptors. For example the Autoregressive (AR) model proposed in [82] to represent the closed shape boundary. The one dimensional representation is obtained using a centroid distance function. The AR model is, then, characterized by a set of unknown parameters and an independent noise sequence. Given the function $u(s)$, the stochastic process is defined by:

$$u(s) = \alpha + \sum_{j=1}^{m} \theta_j u(s-j) + \sqrt{\beta}\omega_s \tag{2.18}$$

where θ_j is the AR coefficients to be estimated, α is a constant to be estimated, $\sqrt{\beta}$ is the variance of prediction noise and ω_s is the independent random noise source. $\theta_1, ..., \theta_m, \alpha, \beta$ are called the model parameters. The shape descriptor vector is constructed using these parameters estimated by the Maximum Likelihood Method. The same AR model is used in [39] with additional methods for improving classification performance. In [33], the AR model is extended to the bivariate case and the classification results are further improved. The disadvantage of the AR model is the sensitivity to shape occlusion [66]. The reason for this drawback is that it models the whole shape with only one set of predictive parameters. If the shape contains a large number of sample points and the contour varies radically, the shape may seem unpredictable. Therefore, an AR model with a finite number of parameters is not adequate for the whole shape. In order to overcome this drawback, the AR model is combined with the Hidden Markov Model in [66]. This approach segments closed shapes into segments, describes each segment by AR modeling and finally analyzes the resulting vectors using a Hidden Markov Model.

2.5.2.4 Boundary Approximation

Boundary approximation methods represent the curves by piecewise polynomial interpolation, which results in a set of smooth curves inflected at control points. Splines are used for the interpolation of functions to approximate shape segments. The power of splines comes from the approximation of a given function with a curve having the minimum average curvature. The main disadvantage of splines is that the local function value modification changes the complete spline representation [93]. For this reason, B-splines are constructed so that the local function value change does not spread to the rest of the intervals. Bsplines are piecewise polynomial curves, whose shape is closely related to their control polygon which is a chain of vertices giving a polynomial representation of a curve. If a control polygon vertex changes its position, a resulting change of the spline curve occur only in a small neighbourhood of that vertex. In [25], curve representation and matching is performed by B-splines. Another method, described in [26], use splines for ROI modelling and shape estimation. Shape preserving approximation based on splines is proposed in [68].

2.5.2.5 Fourier Descriptors

The Fourier representation decomposes a shape contour into its frequency components (Fourier descriptors) obtained via its Fourier transform. The Fourier transform is applied to the boundary function and the resulting coefficients are used for shape description. For a given closed curve, which in turn is represented by a one dimensional function $u(s)$, the discrete Fourier transform is defined by:

$$a_n = \frac{1}{N}\sum_{s=0}^{N-1} u(s)exp(-j2\pi ns/N) \tag{2.19}$$

The coefficients a_n, $n = 0, 1, ..., N-1$, are used to derive Fourier descriptors. In order to achieve translation and rotation invariance the phase information of

a_n is ignored and only the magnitude $|a_n|$ is used. The magnitudes are divided by the DC component $|a_0|$, to achieve the scale invariance. In order to obtain one dimensional function from the shape boundary, various methods have been suggested such as tangent angle [160] and centroid distance [162]. The "classical method" is to express the shape as a sequence of coordinates in the complex plane, namely $u(s) = x(s) + jy(s)$. Modified Fourier descriptors are used in [126] to efficiently compute the feature matching. The Fourier descriptors represent global information about the boundary. Therefore, local spatial information about the shape is not readily available and the level of shape detail can only be controlled on a global basis.

2.5.2.6 Coding

Coding methods describe a ROI by a sequence of unit size line segments with a given orientation. One of the most popular coding scheme is Freeman's chain code [51], which is essentially obtained by mapping the shape boundary into a 2D parameter space, which is made up of codes. The chain code is defined as the direction of the ROI's contour from a starting point. This representation is typically based on 4- or 8-connectivity, and the resulting chain code is a sequence of numbers. There are many variations of Freeman chain codes. A generalized chain code is proposed in [52], where the nodes surrounding a center node are enumerated counter-clockwise in ascending order from inside out.

2.5.2.7 Curvature Scale Space Descriptors

Scale space representations are based on tracking the position of inflection points in a boundary, filtered by low-pass Gaussian functions of variable widths [93]. The inflection points, remaining in the representation are expected to be significant object characteristics [93]. The Curvature Scale Space (CSS) approach proposed in [102] is the most popular one in this class of methods. It has been selected as the MPEG-7 contour based shape descriptor. Mathematically speaking, let Γ be a closed planar curve and u be the normalized arc length parameter on Γ:

$$\Gamma = \{(x(u), y(u))\,|u \in [0,1]\}. \tag{2.20}$$

In order to smooth the curve, functions x(u) and y(u) is convolved with a one dimensional Gaussian kernel at different levels:

$$
\begin{aligned}
X(u,\sigma) &= x(u) * g(u,\sigma), \\
X(u,\sigma) &= y(u) * g(u,\sigma), \qquad (2.21)
\end{aligned}
$$

$g(u,\sigma)$ is a Gaussian kernel of width σ. The curvature of the smoothed curve is then computed as:

$$
k(u,\sigma) = \frac{\dot{X}(u,\sigma)\ddot{Y}(u,\sigma) - \ddot{X}(u,\sigma)\dot{Y}(u,\sigma)}{\left(\dot{X}^2(u,\sigma) + \dot{Y}^2(u,\sigma)\right)^{3/2}}, \qquad (2.22)
$$

where $\dot{X}$, $\dot{Y}$ and $\ddot{X}$, $\ddot{Y}$ are the first and second derivatives of $x(u,\sigma)$ and $y(u,\sigma)$. As σ increases, the shape of Γ_σ changes. This process of generating ordered sequences of curves is referred to as the evolution of Γ. During evolution, the locations of curvature zero crossings of every Γ_σ is determined. The points are then plotted in (u,σ) plane. The result of this process is represented as a binary image, called a CSS image of the curve. Finally, shapes are described by the positions of their CSS contour maxima. These positions projected onto the simplified object contours give the positions of the mid points of the maximal convex/concave arcs, obtained during the curve evolution. Since the small contours on the CSS image represent some information about the existing noise on the actual object, those maxima which are lower than a threshold are discarded. The shape similarity measure between two shapes is computed by relating the positions of the maxima of the corresponding CSSs. The CSS image representation is invariant to scale, rotation and translation. It is also robust to significant non-rigid deformations and perspective deformations. The basic drawback of this representation is the difficulty in the determination of a threshold value in order to remove small contours in CSS image. This process results in a decreased resolution, depending on the predefined threshold value. Therefore, it requires procedures, which find the necessary level of detail or use empirical parameters for sufficient resolution of the shape contour.

2.5.2.8 Simple Boundary Descriptors

Boundary descriptors are mostly based on the geometric properties of the boundary. Because of the discrete character of digital images, all of them are sensitive to image resolution. In the following, popular geometric descriptors are provided for the sake of completeness:

Bending Energy: Given a plane curve $\Gamma = (x(u), y(u))$ and its curvature function $C(u)$ is given by:

$$C(u) = \frac{\dot{X}(u)\ddot{Y}(u) - \ddot{X}(u)\dot{Y}(u)}{\left(\dot{X}^2(u) + \dot{Y}^2(u)\right)^{3/2}}, \tag{2.23}$$

where $\dot{X}$, $\dot{Y}$ and $\ddot{X}$, $\ddot{Y}$ are the first and second derivatives of $x(u)$ and $y(u)$. The bending energy is defined as:

$$E = \frac{1}{N}\sum_{u=1}^{N} C(u)^2 \tag{2.24}$$

Centroid Distance: The centroid distance function is expressed by the distance of the boundary points from the centroid (x_c, y_c) of the ROI:

$$D_{centroid}(s) = \sqrt{(x(s) - x_c)^2 + (y(s) - y_c)^2} \tag{2.25}$$

Convexity(CX): A convex hull is the minimal covering of an ROI. A ROI convexity can be defined as the ratio of perimeters of the convex hull to that of the original contour (P_0). The convexity is represented as [115]:

$$CX = \frac{\text{Convex perimeter}}{P_0} \tag{2.26}$$

Aspect Ratio (AR): The aspect ratio is defined as the height of the ROI divided by its width and is expressed as:

$$AR = \frac{\text{Height of the ROI}}{\text{Width of the ROI}} \tag{2.27}$$

2.6 Summary

This chapter has presented the background and previous work with respect to the research described in this thesis. Image classification, as a sub-domain of image mining, and the challenges of medical image categorization were described. In the context of image pre-processing prior to the application of image classification, several image segmentation techniques that may be applied to medical images were introduced. A review of the literature concerned with ROIBIC was presented. This review indicated that the number of types of shape descriptors for image classification has been rapidly increasing over the last decade; however, each technique has a number of shortcomings. In the next chapter the medical brain MRI scan datasets that were used for the performance evaluation of the proposed techniques are described. The process of preparing these images for image classification, including image registration and image segmentation, will also be presented.

Chapter 3

MRI Datasets: Preprocessing and Segmentation

3.1 Introduction

There have been major advances in the field of medical imaging over the past two decades. New medical imaging technologies have provided physicians with powerful, non-invasive techniques to analyse the structure, function, and pathology of the human body. In more recent years the improvement in (and the development of) many image acquisition techniques, the enhancement of the general quality of the acquired images, advances in image processing and the development of large computational capacities; have considerably enhanced the analysis task. The acquisition of medical images in 2D or 3D has become a routine task for clinical research applications. Image acquisition techniques include Magnetic Resonance Imaging (MRI), Computed Tomography (CT), Positron Emission Tomography (PET) and functional MRI (fMRI). The corresponding increase in the quantity and detail of the available imagery has highlighted the need for more efficient and more effective computer automated, or semi-automated, techniques to support the interpretation of this data in order to provide better diagnosis and treatment options.

The analysis of the increasingly detailed amount of information available constitutes a great challenge for the medical imaging community, and requires significant innovations in all aspect of image processing. One particular challenge is related to the delineations of anatomical structures from medical images, this is seen as a critical step for many clinical and research applications. As noted in the introduction to this thesis the anatomical structure of interest is the corpus callosum, a distinctive feature in MRI brain scans. Some background concerning this application domain is therefore presented in Section 3.2.

The automated recognition of meaningful image components, anatomical structures, and other regions of interest, such as the corpus callosum, is typically achieved using some kind of *registration* and *segmentation* techniques. Some background concerning the registration of brain MRI scans is therefore considered in Section 3.3 as well as mechanisms to align collections of MRI scans to some standard coordinates system. Some background concerning MRI brain scan segmentation techniques is then presented in Section 3.4. In this section a variation of the Normalized Cut segmentation algorithm is proposed, an additional contribution of this thesis, to identify the corpus callosum regions within brain MRI scans. The section commences with some details concerning the original "standard" normalized cuts algorithm, and the multiscale normalized cuts algorithm. The latter was introduced to overcome the computational complexity problem encountered when the standard normalized cuts algorithm is applied to large images. Although, the multiscale normalized cuts produces good results with respect to many image segmentation applications it was found not work efficiently with respect to the application domain considered in this thesis. Therefore, a variation of the multiscale normalized cuts was proposed to deal with this problem. This is fully described at the end of Section 3.4.

This chapter is concluded (Section 3.5) with some details concerning the image data sets used for evaluation purposes with respect to the work described in the reminder of this thesis.

3.2 Application Domain

MRI brain scans underpin the diagnosis and management of patients suffering from various neurological and psychiatric conditions. Analysis of MRI data relies on the expertise of specialists (radiologists) and is therefore subjective. The focus of the research work described in this thesis is brain MR images, and in particular a specific structure in these images called the corpus callosum which connects the two hemispheres of the brain. Figure 3.1 gives an example of a brain MRI scan, the corpus callosum is located in the centre of the image. The corpus callosum was selected to evaluate the work described because it is of interest to medical researchers for a number of reasons. The size and shape of the corpus callosum has been shown to be correlated to sex, age, neurodegenerative diseases (e.g. epilepsy, multiple sclerosis and schizophrenia) and various lateralized behaviour in people (such as handedness). It is also conjectured that the size and shape of the corpus callosum reflects certain human characteristics (such as a mathematical or musical ability). Within neuroimaging research, considerable effort has been directed at quantifying parameters such as length, surface area and volume of structures in living adult brains, and investigating differences in these parameters between sample groups. Several studies indicate that the size and shape of the corpus callosum, in humans, is correlated to sex [4, 34, 128], age [128, 151], brain growth and degeneration [61, 98], handedness [31], epilepsy [27, 124, 149], special skills (e.g.musical ability) [111, 132] and brain disfunction [38, 74].

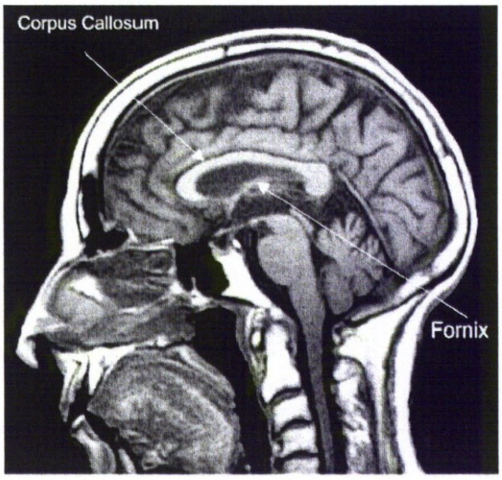

Figure 3.1: The location of the corpus callosum in a brain MR image.

3.3 Image Preprocessing and Registration

Each MRI scan comprised a sequence of "image slices", we refer to this as a *bundle*. The raw dataset used to evaluate the techniques described in this thesis consist of collections of MRI scan bundles. For our experiment we only required the middle slice from each bundle. This is referred to as *midsagittal slice* and is the slice that separates the left and the right hemispheres of the brain.

It should be noted that as a part of the collection process, all slices in all bundles were aligned so that each bundle was centered on the same axes. The alignment (registration) was conducted manually by trained physicians using the Brain Voyager QX software package [56]. Figure 3.2 shows a typical MRI brain scan registered to a "standard" coordinate system using the Brain Voyager QX software package.

BrainVoyager uses several different coordinate systems: the internal axes, the standard Dicom and Talairach axes and the OpenGL axes. The Talairach transformation is at present the most widespread method for brain normalization and registration. The Talairach transformation is based on the 8 Talairach point landmarks that have to be specified: the anterior commissure (AC) and posterior commissure (PC) located on the midsagittal plane (MSP); and 6 cortical landmarks determining the extents of the brain in the anterior (A), posterior (P), left (L), right (R), superior (S), and inferior (I) directions. The AC is taken to be the origin of the coordinate system, the AC-PC line to be the y axis, the vertical line passing through the interhemispheric fissure to be the z-axis, and the line passing through the AC and at right angles to the y and z axes to be the x-axis. The three axes, along with a line parallel to the x-axis passing through the PC, divide the brain into 12 cubic rectangular regions. An appropriate translation parameters (in x, y and z directions) will be specified manually to determine these 8 points. The image bundle is then transformed using a trilinear interpolation. Once the image registration is completed, the midsagittal slice is extracted to delineate the ROI (the corpus callosum with respect to the work described here).

3.4 Brain MR Image Segmentation

As noted in the previous chapter the objective of image segmentation is to partition images into meaningful regions. The segmentation of medical MRI scans is a difficult task for a variety of reasons. Firstly segmentation algorithms tend to operate on the intensity or texture variations of a given image and are therefore sensitive to artifacts produced by the image acquisition process such as: image noise, image intensity inhomogeneity or non-uniformity, and partial volume av-

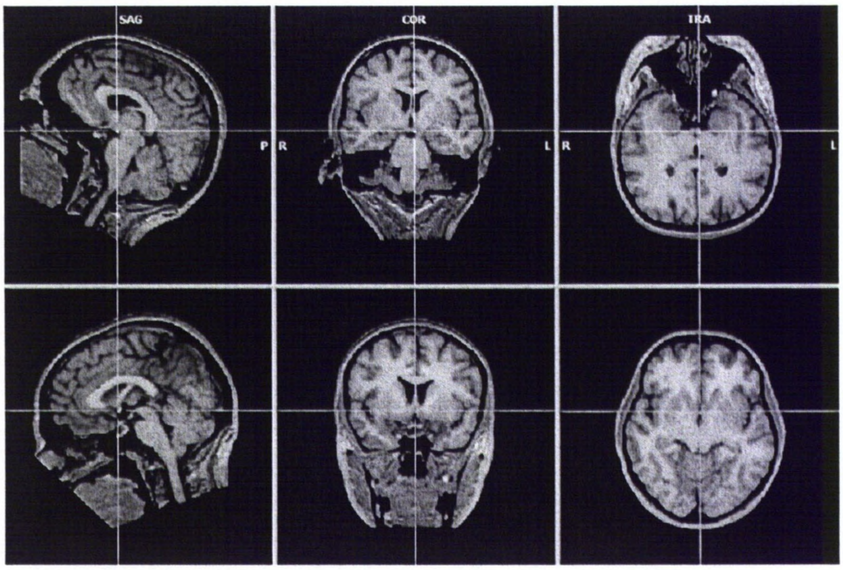

Figure 3.2: A typical brain MRI scan, (a) before the registration (first row scans), and (b) after the registration (second row scans).

eraging effect(as described in Chapter 2). Recall that if only a single tissue type is present in a voxel, the signal intensity will be characteristic of that tissue type. However, if more than one tissue type is present, the signal will be a combination of the contributions of the different tissues. This is known as the *partial volume effect*. Consequently, it blurs the intensity distinction between tissue classes at the border of the two tissues. In the case of brain MRI segmentation the partial volume effect makes it particularly difficult to accurately locate the boundaries of features such as the corpus callosum boundary. For example, if we consider the MRI brain scan given in Figure 3.1 the corpus callosum is located in the centre of the image. A related structure, the fornix, is also indicated. The fornix often blurs into the corpus callosum and thus presents a particular challenge in the context of the segmentation of these images so as to isolate the corpus callosum.

In this section, we discuss the segmentation of the midsagittal brain MRI slice to delineate the corpus callosum. To this end a variation of the Normalized Cuts (NCut) segmentation technique is proposed. NCut formulates segmentation as a graph-partitioning problem. The basic NCut algorithm, proposed by Shi and Malik [135], is presented in the Section 3.4.1. An illustration of the computation of the optimal partitioning of a graph using NCuts, as proposed by Shi and Malik, is presented in Subsection 3.4.2. The basic NCuts algorithm does not operate well when applied to large images such as MRI brain scan images. An established enhancement to the basic NCuts algorithm, the multiscale normalized cuts algorithm proposed by Cour et al. [30], is therefore presented in Section 3.4.3. In the context of the corpus callosum application it was found that the multiscale normalized cuts algorithm could be improved upon so as to reduce the computational resource required to achieve the segmentation. A variation of the multiscale normalized cuts algorithm, proposed by the author of this thesis, is therefore presented in Section 3.4.4.

3.4.1 Normalized Cuts Criterion

In the image segmentation problem based on graph theory, an image is represented by an undirected graph $G = (V, E)$ where V is the set of nodes and E is the set of edges. A weighting matrix W is then defined to measures the similarity between nodes. Each node $v_i \in V$ corresponds to a locally extracted image pixel and each edge $e_i \in E$ connects pairs of nodes. The edges are determined by the proximity of pixels: each pair of pixels (nodes) is connected by an edge if they are located within a distance r from each other. An edge e_i has a weight proportional to the similarity of the properties of the connected nodes (e.g. pixel intensities). Given such a graph representation, image segmentation becomes equivalent to partitioning the nodes of the graph into disjoint sets. Formally, the graph $G = (V, E)$ can be partitioned into two disjoints sets of nodes V_1, V_2, where $V_1 \cup V_2 = V$ and $V_1 \cap V_2 = \phi$. The degree of dissimilarity between these two sets can be expressed as:

$$Cut(V_1, V_2) = \sum_{u \in V_1, v \in V_2} w(u, v). \tag{3.1}$$

where $w(u, v)$ is the similarity between nodes u and v. The weight of the edges that stay within the same set should be as high as possible and the weight of the edges that connect the two sets should be as low as possible. The optimal bipartitioning of a graph is one that minimizes this cut value. Finding the minimum cut is a well-studied problem and there exist efficient algorithms for solving it. Despite the merits of the graph cut formulation and its proposed algorithms, it is biased towards producing cuts that contain a small number of nodes. Therefore Shi and Malik [135] proposed the normalized cuts algorithm (NCuts) as a new measure of disassociation, the normalized cut (NCut) is defined as follows:

$$NCut(V_1, V_2) = \frac{cut(V_1, V_2)}{SumCon(V_1, V)} + \frac{cut(V_1, V_2)}{SumCon(V_2, V)} \tag{3.2}$$

where $SumCon(V_1, V)$ is the total weights of the edges connecting nodes from a set V_1 to all nodes in the original set V and $SumCon(V_2, V)$ is the total weights of the edges connecting nodes from a set V_2 to all nodes in the original set V. The weight of the edges that stay within the same set are contained in $SumCon(V_1, V)$ and $SumCon(V_2, V)$, the weight of the edges that connect the two sets are contained in $cut(V_1, V_2)$. By minimizing this criterion the similarity across partitions is minimized and the similarity within partitions is maximized simultaneously. Unfortunately, minimizing this criterion constitutes an NP-complete problem but Shi and Malik showed that when the normalized cut problem is embedded in a real valued domain an approximate discrete solution can be found efficiently. The details of solving this minimization problem is described in next section.

3.4.2 Optimal Graph Partition Computation

Shi and Malik [135] developed an efficient computational technique based on a generalized eigenvalue problem to minimize the normalized cut. First, W is defined as the affinity matrix of the graph which determines the connectivity of the graph and defines the edges weights. Then the edges weights need to be determined based on the similarity and distance between pixels. This is done by applying the following formula for each edge:

$$w_{i,j} = \begin{cases} exp^{\frac{-\|I_i - I_j\|^2}{\sigma_I^2}} \cdot exp^{\frac{-\|X_i - X_j\|^2}{\sigma_X^2}} & if\ \|X_i - X_j\| \leq r \\ 0 & \text{otherwise} \end{cases} \tag{3.3}$$

where: (i) $w_{i,j}$ is the weight of the edge that connects node i with node j, (ii) I_i is the intensity of pixel i, (iii) X_i is the spatial location of pixel i, (iv) I_j is the intensity of pixel j and (v) X_j the spatial location of pixel j. If there is no edge between node i and node j then $w_{i,j} = 0$ where the distance between node i and node j is greater than distance r. The effect of this procedure is that the pixels that are located very close to each other and that have a very small difference in intensity get a high weight on the edge that connects them. The pixels that are located very far from each other and that have a very big difference in intensity get a low weight on the edge that connects them. All the weights $w_{i,j}$ are saved in a matrix W.

By using matrices Shi and Malik reformulated $NCut(V_1, V_2)$ to:

$$\frac{(1+x)^T(\mathbf{D}-\mathbf{W})(1+x)}{k\mathbf{1}^T\mathbf{D}\mathbf{1}} + \frac{(1-x)^T(\mathbf{D}-\mathbf{W})(1-x)}{(1-k)\mathbf{1}^T\mathbf{D}\mathbf{1}} \tag{3.4}$$

where x is an indicator vector, $x_i = 1$ if node i is in set V_1 and $x_i = -1$ if node i is in set V_2, $\mathbf{D}$ is a diagonal matrix with $d_i = \sum_j w_{i,j}$ on its diagonal and $k = \frac{\sum_{x_i=1} d_i}{\sum_i d_i}$. After some transformations, defining $b = k/(1-k)$ and setting $y = (1+x) - b(1-x)$, the normalized cut problem can be translated into the following formula:

$$min_x NCut(x) = min_y \frac{y^T(\mathbf{D}-\mathbf{W})y}{y^T\mathbf{D}y} \tag{3.5}$$

with the condition $y_i \in \{1, -b\}$ and $y^T\mathbf{D}\mathbf{1} = 0$. This formula is known as the Rayleigh quotient, if y is relaxed to take on real values, it can be minimized by solving the generalized eigenvalue problem:

$$(\mathbf{D}-\mathbf{W})y = \lambda\mathbf{D}y \tag{3.6}$$

The eigenvector corresponding to the second smallest eigenvalue is the real valued solution of the normalized cut problem. The approximate Lanczos method is often used to compute such an eigenvalue problem [58].

In the ideal case, the eigenvector components y_i corresponding to node i should only take on two discrete values. For example, if $y_i = 1$ or -1 then the signs tell us exactly how to partition the graph nodes V into V_1 and V_2 as follows: node i is in V_1 if the eigenvector components y_i, corresponding to node i, equals to 1 and node i is in V_2 if the eigenvector components y_i, corresponding to node i, equals to -1. i.e. the splitting point is 0 and the sign tells us exactly how to partition this graph ($V_1 = \{Vi|yi > 0\}, V_2 = \{Vi|yi <= 0\}$). However, eigenvector y is relaxed to take real values, therefore, a splitting point is needed to determine the two sets of nodes. To finally get the approximate discrete solution the eigenvector is split into two parts by mapping the real values to the discrete set of values over the interval $\{1, -b\}$. This mapping is done by sorting the real values of this eigenvector and evaluating $NCut(V_1, V_2)$ for a few evenly spaced splitting points. The split point that produces the lowest $NCut(V_1, V_2)$ will then finally give us the approximate solution: the disjoint sets V_1 and V_2 together with their $NCut(V_1, V_2)$ value. The algorithm is recursively applied to every subgraph until the value of $NCut$ exceeds a certain threshold or the total number of nodes in the partition is smaller than a pre-specified threshold value.

From the above, the procedure for image segmentation based on normalized cuts can be summarized as follows:

1. Given an image I, construct an $N \times N$ symmetric similarity matrix $\mathbf{W}$ according to Equation 3.3 and $\mathbf{D}$ as a diagonal matrix with $d_i = \sum_j w_{i,j}$ on its diagonal.
2. Solve the generalized eigenvalue problem
   $(\mathbf{D} - \mathbf{W})\, y = \lambda \mathbf{D} y$
   and get the eigenvector with the second smallest eigenvalue.
3. Find the splitting point of eigenvector y, where $y_i \in \{1, -b\}$, that minimizes the $NCut$
4. Bipartition the graph nodes V into V_1 and V_2 according to this splitting point.
5. Repeat the bipartition recursively, stop if the $NCut$ value is larger than a pre-specified threshold value or the total number of nodes in the partition is smaller than a pre-specified threshold value.

The normalized cuts algorithm is computationally expensive when the dimension of the weight matrix is large because the pixel-based weight matrix required to compute the $N \times N$ weight matrix becomes very dense. Consequently the derivation of the eigenvalues becomes computationally expensive even though the approximate eigenvalue method and associated algorithm are designed to optimize this process.

3.4.3 Multiscale Normalized Cuts

Cour et al. [30] proposes a Normalized Cut adaptive technique, the Multiscale Normalized Cuts algorithm, that focuses on the computational problem created by large graphs, which yields a better segmentation than the original Normalized Cuts. Cour et al. suggested the use of multiscale segmentations, decomposing a large graph into independent subgraphs. The main contribution of this technique is that larger images can be better segmented with linear complexity. In this technique, a graph representation of the image is again used as well as in the original normalized cuts segmentation approach described above. Basically this representation again comprises an undirected weighted graph $G = (V, E)$ where each node $v_i \in V$ corresponds to a locally extracted image pixels and the edges e_i in E connect pairs of nodes. The edges are determined by the proximity of pixels: each pair of pixels (nodes) is connected by an edge if they are located within a distance r from each other; also called the graph connection radius. A larger graph radius r generally makes segmentation better and facilitates the detection of objects described by faint contours against a cluttered background, but it is computationally expensive because the similarity matrix W becomes denser. In the multiscale normalised cuts algorithm, two cues are used to determine the connectivity of the graph; the intensity and position grouping cue and the intervening contours grouping cue. The edge weights can then be determined based on the similarity and distance between pixels. The intensity and position grouping cue of each edge is given by:

$$w_{IP}(i,j) = \begin{cases} exp^{\frac{-\|I_i - I_j\|^2}{\sigma_I^2}} \cdot exp^{\frac{-\|X_i - X_j\|^2}{\sigma_X^2}} & if\ \|X_i - X_j\| \leq r \\ 0 & \text{otherwise} \end{cases} \tag{3.7}$$

where $w_{IP}(i,j)$ is the weight of the edge that connects node i with node j, I_i is the intensity of pixel i, X_i is the spatial location of pixel i, I_j is the intensity of pixel j and X_j is the spatial location of pixel j. If there is no edge between node i and node j then $w_{i,j} = 0$. This grouping cue, used separately; often gives bad segmentations because some natural images (including medical images) are affected by "texture clutter". The intervening contours grouping cue evaluates the affinity between two pixels by measuring the image edges between them. The measure of similarity regarding this grouping cue is given by[30]:

$$w_C(i,j) = exp - \left(\frac{max_{(x \in line(i,j))\varepsilon^2}}{\sigma_c} \right) \tag{3.8}$$

where $line(i,j)$ is a straight line joining pixels i and j and $\varepsilon = \|Edge(x)\|$ is the image strength at location x. These two cues can be combined as shown by[30]:

$$w(i,j) = \sqrt{w_{IP}(i,j)\, w_C(i,j)} + w_C(i,j) \tag{3.9}$$

The multiscale normalized cut algorithm [30] works on multiple scales of the image so as to capture both coarse and fine levels of details. The construction of the image segmentation graph is given according to their spatial separation, as in:

$$W = W_1 + W_2 + \ldots + W_s, \tag{3.10}$$

where W represents the graph weights $w(i,j)$ and s the scale, i.e. W_s contains similarity measure between pixels with certain scale s. Two pixels i, j are connected only if $r_{s-1} < \|X_i - X_j\| \leq r_s$. The r value is a tradeoff between the computation cost and the segmentation result. The decomposition graph above can alleviate this situation. W_s can be compressed using recursive sub-sampling of the image pixels. Cour et al. determine representative pixels at each scale s as follows. First they sample representative pixels at $(2r+1)^{s-1}$ distance apart on the original image grid, and denote the representative pixels at each scale s by I_s and denote W_s^c as a compressed similarity matrix with connections between representative pixels in I_s, i.e. for the first graph scale, every pixel is a graph node and two nodes are connected with a graph edge if the two pixels are within r distance apart. They then construct W_1^c as a compressed similarity matrix with connections between representative pixels in I_1. For the second graph scale, they consider pixels at distance $2r+1$ apart in the original grid as representative nodes, I_2 and construct W_2^c as a compressed similarity matrix with connections between representative pixels in I_2. For the third graph scale, they consider pixels at distance $(2r+1)^2$ apart in the original grid as representative nodes, I_3 and construct W_3^c as a compressed similarity matrix with connections between representative pixels in I_3. In general, they consider pixels at distance $(2r+1)^{(s-1)}$ apart in the original grid as representative nodes, I_s. Then the full multiscale similirity matrix W can be expressed as:

$$W = \begin{pmatrix} W_1^c & & 0 \\ & \ddots & \\ 0 & & W_s^c \end{pmatrix} \tag{3.11}$$

Cour et al. reformulated the constrained multiscale normalized cut into the following formula:

$$\begin{aligned} maximize\ \varphi(X) &= \frac{1}{K}\sum_{l=1}^{K}\frac{X_l^T W X_l}{X_l^T D X_l} \\ subject\,to:\ CX &= 0 \end{aligned} \tag{3.12}$$

where X is an indicator vector s.t. $X \in \{0,1\}^{N^* \times K}$, $N^* = \sum_s N_s$, N_s is the number of representative pixels in I_s. The cross-scale constraint matrix C:

$$C = \begin{pmatrix} C_{1,2} & -I_2 & & 0 \\ & \ddots & \ddots & \\ 0 & & C_{S-1,S} & -I_S \end{pmatrix} \tag{3.13}$$

where $C_{s,s+1}(i,j) = \frac{1}{|N_i|}\quad if\quad j \in N_i$ and N_i is the neighbourhood which specifies the projection of $i \in I_{s+1}$ on the finer layer I_s.

The NP-complete constrained normalized cut is thus transformed into the following eigenvalue problem:

$$\bar{W}\bar{X} = \lambda\bar{X} \tag{3.14}$$

where:

$$\bar{W} = QD^{-1/2}WD^{-1/2}Q \tag{3.15}$$

and

$$Q = I - D^{-1/2}C^T(CD^{-1}CT)^{-1}CD^{-1/2} \tag{3.16}$$

The K first eigenvectors of $\bar{W}$ is used to find the indicator vectors X to segment the image into K partitions.

From the above, the image segmentation procedure based on multiscale normalized cuts can be summarized as follows:

1. Given an $m \times n$ image I, for $s = 1..S$ (S = number of scales):
   (a) Sample $\frac{m}{\rho} \times \frac{n}{\rho}$ pixels $i \in I_s$ from I_{s-1}, where ρ is the sampling factor.
   (b) Compute constraint $C_{s,s+1}(i,j) = \frac{1}{|N_i|}$, $j \in N_i$ sampling neighbourhood of i.

   (c) Compute the similarity matrix W_s^c for the representative pixels I_s.

2. Compute W, C from $(W_s, C_{s-1,s})$ as in (3.11),(3.13).
3. Solve the eigensystem $\bar{W}\bar{X} = \lambda\bar{X}$ as in (3.15), (3.16).
4. Use the first k eigenvectors of $\bar{W}$ to partition the image into k segments.

The multiscale normalized cuts algorithm has been shown to work well in many studies; however it was found that, in the context of the corpus callosum application, the algorithm did not work as well as expected with respect to all brain MRI scans in the test data sets. This was because: (i) MRI brain scans include a lot of noises, (ii) the intensity-level distributions between different soft tissues were not widely distributed and (iii) the complexity of tissue boundaries caused many pixels to contain mixtures of tissues. Although one can visually recognize the outline of the corpus callosum (Figure 3.1), portions of its boundary are indistinct, which can make it difficult to apply segmentation algorithms based on edge information alone. A further problem is that, quite often, intensity variations within the corpus callosum can be comparable or exceed the difference with the surrounding tissues. For these reasons it is desirable to enhance the contrast of the MR images. A variation of the multiscale normalized cuts algorithm was therefore developed. This is described in the following Subsection 3.4.4.

3.4.4 Proposed Approach

As noted above, the multiscale normalized cuts algorithm when applied to brain MRI scans to delineate the corpus callosum within these scans did not give satisfactory results with respect to all brain MRI scans in the test data. In the case of some scans the corpus callosum region can be clearly identified as shown in Figure 3.3 but blurred into other surrounding tissues in some other scans. Therefore a variation of the multiscale normalized cuts algorithm was developed that applied a threshold interval to extract objects with the same intensity values (such as the corpus callosum) during the application of the segmentation. This was found to give a much improved result.

The proposed variation of the multiscale normalized cuts algorithm was founded on the observation that the corpus callosum, which is located at the centre of the

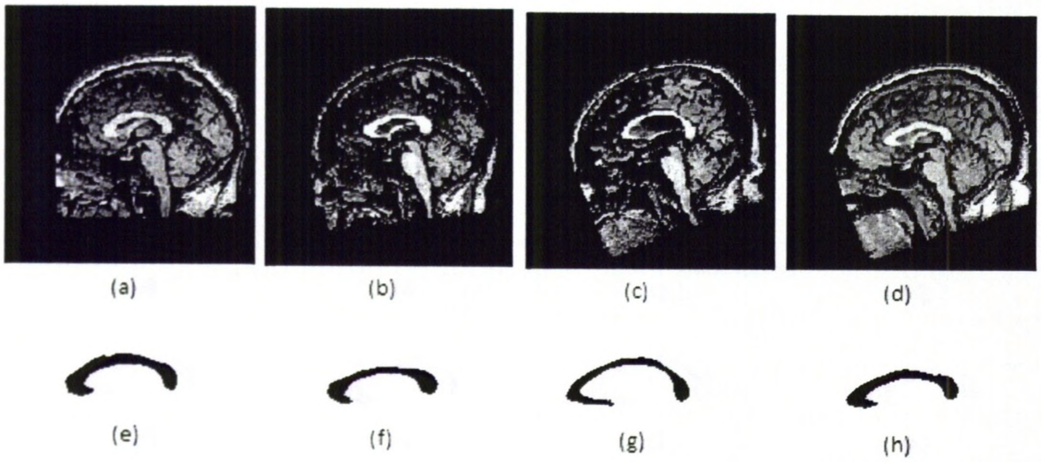
(a) (b) (c) (d)

(e) (f) (g) (h)

Figure 3.3: The results obtained by the multiscale normalized cuts algorithm, (a-d) the original brain MRI scans, (e-h) the corpus callosum obtained by the multiscale normalized cuts.

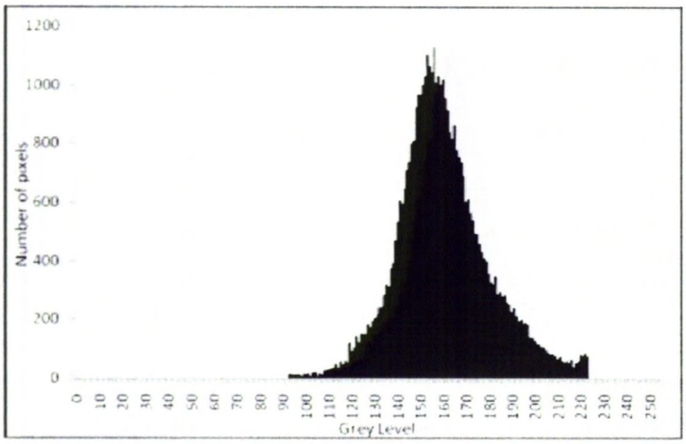

Figure 3.4: Histogram of the pixel greyscale values of the corpus callosum.

brain, comprises *white matter tissue* (i.e. the pixel represented corpus callosum have high intensity values). Figure 3.4 shows a pixel intensity value histogram of the corpus callosum derived from 30 selected MR images (256 grey levels were used) where the corpus callosum was very well defined and easy to detect using the multiscale normalized cuts algorithm. From the figure it can be seen that:

- The corpus callosum tends to have relatively high intensity values, and
- The distribution of intensity values seems to follow the normal distribution.

The latter is demonstrated in Figure 3.5 where it can be seen that the corpus callosum pixel values follow the normal distribution with mean $\bar{X} = 160$ and standard deviation $S = 20$. Figure 3.6a shows that with a threshold interval of $\bar{X} \pm S$, the corpus callosum can barely be recognized. With a threshold interval $\bar{X} \pm 2S$ a relatively distinct callosum shape is evident with a few other non-adjacent structures visible as shown in Figure 3.6b. With the threshold interval set at $\bar{X} \pm 3S$, the corpus callosum is clearly defined, although additional non-adjacent structures are also visible (Figure 3.6c). In Figure 3.6d, the corpus callosum starts to "blur" into the surrounding tissues using a threshold interval wider than $\bar{X} \pm 3S$. The significance here is that although the threshold values may differ depending on individual images, the high intensity property of the corpus callosum can be exploited to yield a segmentation algorithm that is both effective and efficient across the input image set. Therefore the interval $\bar{X} \pm 3S$ was chosen, so as to exclude intensity values outside the interval. This strategy was incorporated into multiscale normalized cuts algorithm and used to successfully extract the corpus callosum (and other incidental objects with the same intensity values).

The operation of the proposed image segmentation approach can be summarized as follows:

1. Apply the multiscale normalized cuts algorithm to the brain MRI scans datasets.
2. Calculate the sample mean $\bar{X}$ and standard deviation S corresponding to the fully segmented corpus callosum regions.

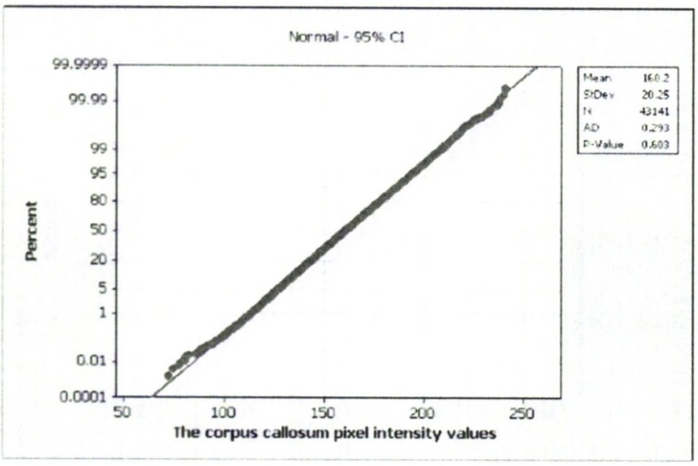

Figure 3.5: Probability plot of the corpus callosum pixel values.

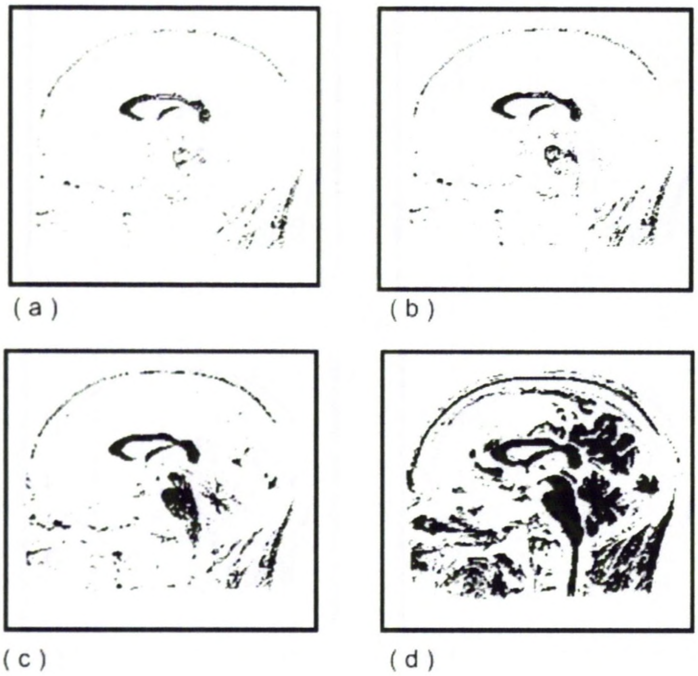

Figure 3.6: Thresholding with various threshold intervals.

3. Apply the threshold interval $\bar{X} \pm 3S$ to the reminder of the brain MRI scans where the corpus callosum is not delineated correctly.
4. Apply the multiscale normalized cut algorithm to the brain MRI scans resulting in step 3

For evaluation purposes the proposed approach was applied to brain MRI scans where the corpus callosum was not completely identified using the multiscale normalized cuts algorithm. Figure 3.7 presents a comparison between results obtained using the Multiscale Normalised Cuts algorithm (Figure 3.7(e) to (h)) and the proposed approach (Figure 3.7(i) to (j)). From the figure it can be seen that better results were obtained using the proposed approach.

Some *data cleaning* was also undertaken to remove the "incidental objects" discovered during segmentation. The heuristic used was that the object representing the corpus callosum can be identified using statistical measures (it is the largest object and is locate in roughly the centre of the brain). Having identified the corpus callosum object any other high intensity objects could be removed.

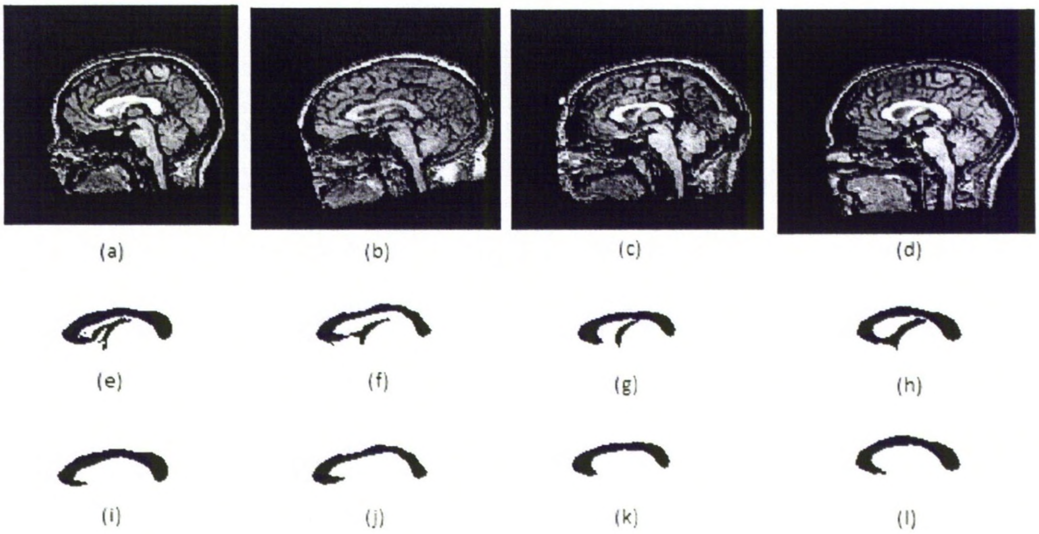

Figure 3.7: The results obtained by the multiscale normalized cuts algorithm and the proposed approach, (a-d) the original brain MRI scans, (e-h) the corpus callosum obtained by the multiscale normalized cuts, (i-l) the corpus callosum obtained by the proposed algorithm.

3.5 Medical Image Datasets

To evaluate the ROIBIC techniques described in this thesis to classify medical images according to a particular object that features across the data sets a number of data sets were used. As already noted the data sets were generated by extracting the *midsagittal slice* from MRI brain scan data volumes (bundles), one image per volume. Each data set thus comprised a number of brain MRI scans each measuring 256 × 256 pixels, with 256 greyscale levels and each describing a midsagittal slice. To support the evaluation the data sets were grouped as follows: (i) musicians, (ii) handedness and (iii) epilepsy. Each group is described in some further detail as follows:

Musicians datasets. For the musicians study the data set comprising 106 MRI scans, 53 representing musicians and 53 non-musicians (i.e. two equal classes). The study was of interest because of the conjecture that the size and shape of the corpus callosum reflects human characteristics (such as a musical or mathematical ability) [111, 132].

Handedness datasets. For the handedness study a data set comprising 82 MRI scans was used, 42 representing right handed individuals and 40 left handed individuals. The study was of interest because of the conjecture that the size and shape of the corpus callosum reflects certain human characteristics (such as handedness) [31].

Epilepsy datasets. For the epilepsy study three data sets (Ep_{106}, Ep_{159} and Ep_{212})were used. The first data set, Ep_{106},comprised the control group from the musicians study (the non-musicians) and 53 MRI scans from epilepsy patients so as to give a balanced data set. The second data set, Ep_{159}, used all 106 MRI scans from the musicians study and 53 epilepsy scans. The third data set, Ep_{212} was the same as the second but augmented with a further 53 epilepsy cases to create a balanced data set. The objective was to seek support for the conjecture that the shape and size of the corpus callosum is influence by conditions such as epilepsy [27, 124, 149].

All three brain MRI datasets were preprocessed using the variation of the multiscale normalized cuts algorithm described above (Subsection 3.4.4) to extract the corpus callosum feature. On completion of data cleaning a "local" registration process was undertaken by fitting each identified corpus callosum into a Minimum Bounding Rectangle (MBR) so that each identified corpus callosum was founded upon the same origin.

3.6 Summary

This chapter has provided the necessary context to the preprocessing of the brain MRI scan data so as to detect and extract the desired ROI (the corpus callosum). A variation of the multiscale normalized cuts algorithm was proposed to achieve the desired segmentation. A description of the medical image datasets, used for evaluation purposes later in this thesis, was also given. In the following four chapters the four different techniques, whereby MRI brain scan data can be classified according to a particular ROI (namely the corpus callosum), considered in this thesis are described and evaluated. The first technique considered is the Hough Transform technique which is presented in the following chapter.

Chapter 4

Region Of Interest Image Classification Using a Hough Transform Signature Representation

4.1 Introduction

As noted in Chapter 2 the Hough transform was first introduced by Paul Hough in 1962 [67]. It later became the basis for a great number of image analysis techniques with respect to many applications. The Hough transform is mainly used to detect parametric shapes in images. It was first used to detect straight lines and later extended to other parametric models such as circles or ellipses, being finally generalized to detect any parametric shape [12]. The key idea of the Hough transform is that spatially extended patterns are transformed into a parameter space where they can be represented in a spatially compact way. Thus, a difficult global detection problem in the image space is reduced to an easier problem of peak detection in a parameter space. A set of collinear image points (x, y) can be represented by the equation:

$$y - mx - c = 0 \tag{4.1}$$

where m and c are the standard parameters slope and intercept, which characterize the line equations. Equation 4.1 maps each value of the parameter combination (m, c) to a set of image points. But Equation 4.1 can be "read" as a backprojection, i.e. it represents the set of straight lines, each defined by a point (m, c)

in the parameter space, passing through an image point (x, y). From this point of view, each image point (x, y) defines a straight line in the parameter space which represents all possible combinations of (m, c) that defining a line passing through (x, y). Points which are *collinear* in the image space all intersect at a common point in the parameter space and the coordinates of this point characterizes the straight line connecting the image points. Thus, the problem of line detection in the image space is transformed to the problem of finding intersection points (peaks) in the parameter space, a much simpler problem to resolve. The straight line Hough transform can easily be extended to detect other parametrically defined curves that may be contained in an image. Image points of a curve characterized by n parameters $\alpha_1, ..., \alpha_n$ can be defined by an equation of the form:

$$f(\alpha_1, ..., \alpha_n, x, y) = 0 \tag{4.2}$$

Following the same idea, an image point (x, y) can be used to define a hypersurface in some n-dimensional parameter space $(\alpha_1, ..., \alpha_n)$. The intersections of such hypersurfaces indicate the parameters which are likely to characterize instances of the searched curves in the image space. The Hough transform offers several advantages:

1. Each image point is treated independently and therefore parallel processing is possible, consequently the method is suitable for real-time applications, such as CCTV surveillance analysis.

2. The method is robust to the presence of noise since noisy image points are very unlikely to contribute to a peak in the parameter space.

3. Since each image point contributes independently to the set of parameter space points, the algorithm is able to work even if the shape is occluded.

4. The Hough transform is able to detect different instances of the desired shape at the same time, depending on the number of peaks which are considered in the parameter space.

The main drawbacks of the Hough transform are its large storage and computational requirements. The computational load can be reduced by using information from the image to restrict the range of parameters which must be calculated from each image point. For example, Ballard [12] described how to optimize circle detection by the use of gradient information. The storage requirements can also be reduced by multistage processing so as to decompose a high dimensional problem into separate lower dimensional ones; parameter reduction techniques also involve a reduction of the computational load. A similar approach to reducing the storage requirements and computational load is to analyze the parameter space at different scales using a *coarse-to-fine* technique which focuses the analysis on those areas of the parameter space that have a high density.

In the rest of this chapter we first, Section 4.2, further describe the Straight Line Hough Transform (SLHT) as this is the basis for the proposed Hough transform based method for image classification according to the nature of region of interest. In Section 4.3 the most common extensions of the Hough transform are reviewed. The review is not exhaustive because these extensions are outside of the scope of the research direction of concern; however they are considered because the Vlachos approach described in this section provides the basis for the proposed method. The proposed Hough transform based approach is presented in section 4.4, the novel element of this approach is the polygonal approximation technique included in the classification process. The evaluation of the proposed approach is described and discussed in sections 4.5 and 4.6 respectively. The chapter is then concluded with a summary in section 4.7.

4.2 The Straight Line Hough Transform

The Straight Line Hough Transform (SLHT) was the first, and probably the most used, of the parameter-based transformations derived from the Hough concept [67]. The SLHT was introduced in the previous section starting from Equation 4.1. However, a problem arises when lines have large slopes, i.e. $m \to \infty$. Duda and Hart [40] solved the problem of an unbounded parameter space suggesting that straight lines might be more usefully parametrized by the use of polar coordinates, i.e. the length ρ and the orientation θ of the normal vector to the line from the image origin. Thus, a straight line can be represented by the following equation:

$$\rho = x cos\theta + y sin\theta \tag{4.3}$$

In the conventional implementation, the Hough transform essentially consists of three stages:

1. **Characteristic point detection.** Not all the image points (pixels) are mapped to the parameter space. An information reduction process is first applied to the image in such a way that it preserves the shapes to be detected. To achieve this some image pixels are selected according to certain local properties (e.g. gradient magnitude and gradient orientation). Usually the information reduction process comprises local edge detection.

2. **Transform mapping.** Each *characteristic point* of the image space is mapped to the parameter space. This parameter space is represented by a two-dimensional accumulator array (n-dimensional for detection of higher-order shapes). A voting rule usually underlies the transform mapping. This voting rule determines how the transform mapping affects the contents of the accumulator array. The simplest voting rule is to increment the polar parameter points (ρ, θ) mapped from an image point (x, y).

3. **Peak detection.** The final stage is to extract the corresponding parameter values of the detected shape from the accumulator array. The simplest method is to apply some form of global thresholding on the accumulator array. The threshold is chosen either using prior knowledge, or it can be automatically selected by analysing the distribution of counts in the accumulator array, e.g. a fixed fraction of the maximum count on any single accumulator bin. Since the presence of noise and distortion may result in true peaks being split between several accumulator cells and, thus causing them not to be detected, different kinds of clustering procedures are also applied.

Two types of Hough transform are usually distinguished depending on the representation which is used:

- **One to many (1-m).** Each characteristic point (x, y) of the image space is mapped to m points in the parameter space which represent the m possible straight lines which passes through the point (x, y). Thus, in an ideal case, a straight line in the image space formed by n points will be mapped to a point (ρ, θ) in the parameter space with an accumulation value equal to n.

- **Many to one (m-1).** In this case m represents the number of points necessary to define, without ambiguity, the parametric shape to be detected. As for straight lines, m is equal to 2 since in the R^2 space a straight line can be defined from two points. Hence, each pair of points of the image space is mapped to one point (ρ, θ) in the parameter space which defines the straight line passing through both image points. Therefore, in an ideal case, a straight line in the image space formed by n points will be mapped to an accumulation point with value equal to $(n(n-1))/2$.

Figure 4.1 illustrates the 1-m and m-1 SLHT. It can be observed, when the transformation is 1-m, that four collinear image points result in four sinusoidal functions in the parameter space. These functions intersect at point (ρ, θ) defining the straight line shared by the four image points. On the other hand, when the m-1 transformation is computed, each pair of image points give a "vote" in the accumulator array. Thus, the peak (ρ, θ) which defines the straight line will have a value of 6 in the accumulator array.

4.3 Extensions of the Basic Hough Transform

The basic Hough transform has been extended to more complex shapes. Two examples are considered in this section. The first is concerned with higher-dimensional parametrized shapes, such as circles and ellipses; these can be detected using a similar approach to that of the SLHT but with a parameter space with more dimensions. The main drawback of this method is the increase in the number of dimensions, which in turn results in a larger storage requirement. The second example is concerned with approaches which use the Hough transform to detect more arbitrary shapes; shapes which can not be analytically represented.

4.3.1 Circles and Ellipses

The use of the Hough transform to detect circles was first proposed by Duda and Hart [40]. The points (x, y) belonging to a circle characterized by its centre

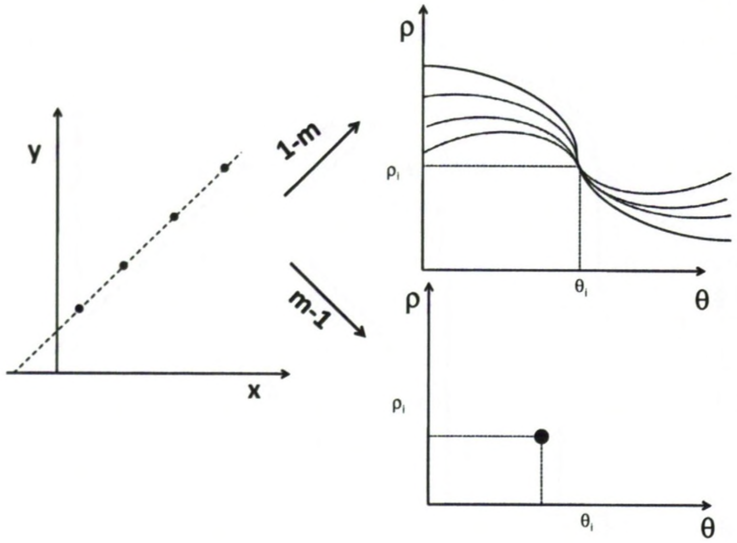

Figure 4.1: The 1-m and m-1 SLHT.

coordinates (x_c, y_c) and its radius r can be represented by the equation:

$$(x - x_c)^2 + (y - y_c)^2 = r^2 \tag{4.4}$$

This equation indicates that point (x, y) of the image space can be mapped to a cone surface in the (x_c, y_c, r) parameter space which represents all possible circles passing through (x, y). If the cones corresponding to many edge points intersect at a single point, then all the image points lie on the circle defined by those three parameters. The Hough transform for circle detection can also be computed as a $1 - m$ or $m - 1$ transform. Figure 4.2 illustrates these two possible transformations. Similarly an ellipse can be parametrized by its centre coordinates, major and minor radii, and orientation, i.e. (x_c, y_c, a, b, θ). Thus, the Hough transform for ellipse detection requires a 5-dimensional parameter space. In general, a circle can be considered as a particular case of an ellipse where $a = b = r$, and θ is not considered. However, circles have specially designed algorithms. The conventional Hough transform for circle finding requires a 3-dimensional accumulator array of $O(mnR)$ cells, where $m \times n$ is the image size and R is the number of possible radii. The method is of course extremely computationally intensive. The use of the gradients of the image points can reduce the memory requirements and the computational load. Davies [35] used a standard Sobel operator to estimate the gradient for each image point. A normal to the tangent to the circle at the point (x, y) will then pass through the centre of the circle and make an angle θ with the horizontal axis. The data triples (x, y, θ) are mapped into a two dimensional parameter space (x_c, y_c) as straight lines representing all possible centres. The intersection between many straight lines in this parameter space then determines the centre coordinates of the circle. These coordinates are then used to calculate a histogram of possible radius values. A similar method was developed by Kierkegaard [84] to detect circular arcs in images of industrial environments. Circular arc detection requires the computation of two additional parameters which define the angular orientation and size. It is performed using a histogramming procedure which accumulates the angles of the vectors from the image points to the center of the circle to which they belong. Yip et al. [158] proposed a variation of the Hough transform for circle and ellipse detection which only requires a 2-dimensional accumulator array. They use five geometric properties of symmetric points of an ellipse to reduce the dimension of the accumulator array. Each pair of image points with the same gradient defines two parallel lines which may be considered as tangents to an ellipse. The parameters (x_c, y_c, a, b, θ) are computed from these two image points with respect to the five geometric properties. A technique which transforms the ellipse's parameters (x_c, y_c, a, b, θ) to a 2-dimensional format is used. This technique consists of transforming the parameters (x_c, y_c, a, b, θ) to the four vertex positions of the corresponding ellipse (i.e. the intersections between the ellipse and the major and minor radii, respectively) which are accumulated in a 2-dimensional array. Hence, the ellipse parameters can be recovered by detecting the four vertex positions in the 2-dimensional array. For further discussion regarding a variety of circle detection methods based on variations of the Hough transform the interested reader is referred to the comparative study by Yuen et al. [159].

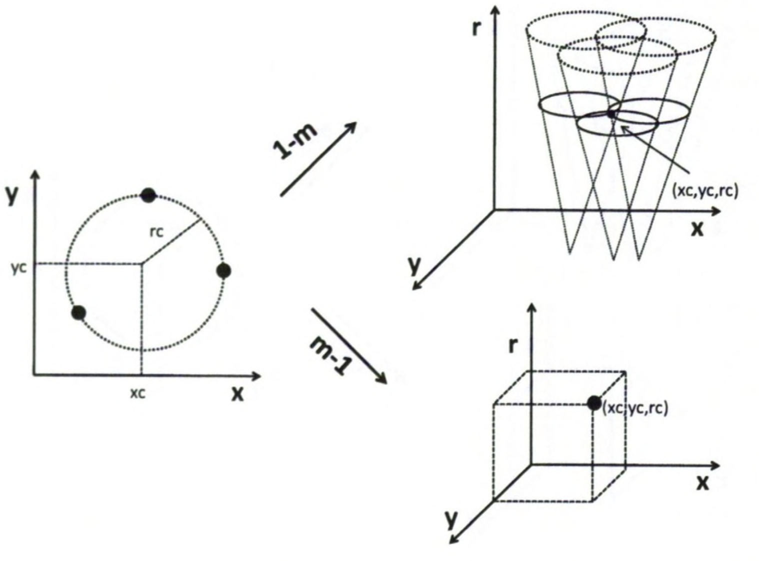

Figure 4.2: 1-m and m-1 Hough transforms for circle detection.

4.3.2 Generalized Shapes

Various authors have developed variations on the Hough transform to detect shapes other than straight lines, circles and ellipses. The Hough transform has been extended to detect arbitrary shapes which can not be analytically represented. The work of Ballard [12] is a standard reference concerning generalized shape detection using what is known as the Generalized Hough Transform (GHT). Ballard uses the directional information associated with each characteristic point, computed by an edge detection preprocessing, to detect arbitrary shapes. Given an random shape (see Figure 4.3), a reference point P is selected within it. Each boundary point of the shape can be represented by the distance r and the direction ϕ the line connecting the boundary point and the reference point. These two values are represented as a functions of the local edge normal direction θ, i.e. $r(\theta)$ and $\phi(\theta)$, and stored in a lookup table, called an R-table. Given an image in which we wish to detect a shape, each edge point has associated with it an attribute describing the direction θ computed by a gradient operator. Using θ to index into the R-table, each point gives a "vote" for an hypothetic reference point P. Thus, peaks will localize the shape under detection. This method works when shapes are of fixed orientation and scale, otherwise more than two parameters must be used for the description of the shape. For further information interested readers are referred to Davies [35] who conducted a comprehensive study of the GHT and its computation.

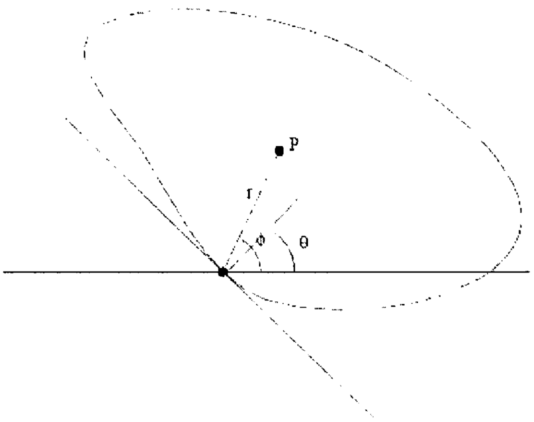

Figure 4.3: An example of generalized Hough transform for arbitrary shapes.

The detection of shapes combining the SLHT with the information reported by the lines tangent to the boundary shape is a widespread task. Using this idea of obtaining the tangents of a shape from its corresponding (ρ, θ) space after computing the SLHT, Leavers [89] proposed an alternative method of shape detection which uses the Hough transform to decompose an edge image into its constituent shape primitives (straight lines and circular arcs). The parameters associated with these primitives are then used to build a symbolic representation of the shape to be detected. This method uses the SLHT iteratively in order to extract straight line features first and then circular arcs. Another outstanding work concerning the use of the SLHT to generalized shape detection was developed by Pao et al. [112]. First, they analyzed how translation, rotation and scaling of an image space affects the parameter space. Consequently, they proposed to decompose the SLHT parameter space into three subspaces, namely, the translation space, rotation space, and the intrinsic space. A second transform, referred to as the signature of the shape, is performed on the SLHT parameter space by computing the distances between pairs of points in the (ρ, θ) space that have the same θ value. This is equivalent to computing the perpendicular distances between pairs of parallel tangents to the curves. This signature has the following properties: (i) it is invariant to translation, (ii) rotations in the image space correspond to circular shiftings of the signature, and (iii) it can be easily normalized. The recognition of a shape is performed by a one-dimensional correlation between the candidate signature and the normalized model signature. The peak of this correlation also indicates the orientation of the object. Finally, the location of the shape is obtained by an inverse transform from the (ρ, θ) space to the (x, y) space. In [145], Vlachos et al. adopted the SLHT to extract a region signature to be used in the image classification process. They use the projection of the accumulator array from $\rho - \theta$ space to θ space. Then the region signature can be expressed as one dimensional vector in terms of θ after the normalization of that vector by dividing it by its mean value. The significance of Vlachos approach with respect to this thesis is that it has been adopted for the proposed Hough transform based ROIBIC process.

4.4 Proposed Image Classification Method

The proposed image classification based on the Hough transform focuses primarily on the extracting of *shape signatures* which can be used as a feature vector in the classification process. Therefore, it is assumed that the input image is a binary representation of a region of interest (i.e. the corpus callosum with respect to the focus of the work described in this thesis), that has been appropriately segmented from "source" MRI brain scans of the form previously described in Chapter 3. The proposed shape signature extraction method is founded on that first presented in Vlachos et al. [145] which was briefly described in Subsection 4.3.2. This method gives good results when classifying simple line drawn symbol images according to their shapes. However, Vlachos approach was found to perform consistently badly with respect to the classification of brain MRI scans according to the nature of the corpus callosum. Therefore the proposed method commences by simplifying the shape of the region of interest within the MRI brain scans using a polygonal approximation method. Then the signature extraction process, using Vlachos approach, was applied.

The proposed image classification technique based on the Hough transform is

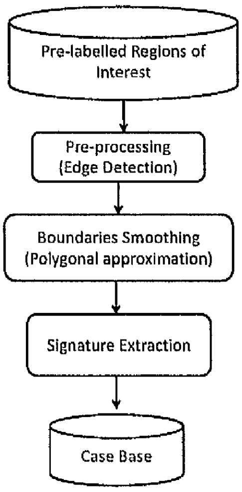

Figure 4.4: The framework of the proposed approach based on Hough transform.

thus composed of three majors steps as depicted in Figure 4.4. Referring to the figure, we start with a data set of pre-labelled images. Then (Step 1), for each image, the region of interest, i.e. the corpus callosum, is pre-processed using a *Canny edge detector* to determine its boundary. Secondly (Step 2), a polygonal approximation technique is applied to reduce the complexity of the boundaries and approximate these boundaries with a minimum number of line segments. Thirdly (Step 3), signature extraction using the SLHT is applied to extract the feature vector which is then placed in a Case Base (CB). The CB ultimately comprises feature vectors extracted from all the images in the given training set and their corresponding class labels. This CB was then used, in the context of a Case Based Reasoning (CBR) framework, to classify unseen MRI brain scans according to the nature of the corpus callosum. Steps 1, 2 and 3 are discussed in further detail in the following three sub-sections.

4.4.1 Step 1: Preprocessing

The extraction of the desired shape signatures (one per region of interest within each image) commences by applying the Canny edge detector technique [20]. The Canny operator detects the edge pixels of an object using a multi-stage process.

First of all, the region boundary is smoothed by applying a Gaussian filter. Then the edge strength is calculated by applying a simple 2D first derivative operator. The region is then scanned along the region gradient direction, and if pixels are not part of the local maxima they are set to zero, a process known as non-maximal suppression. Finally, a threshold is applied to select the correct edge pixels. When the edge detection technique is applied to the corpus callosum each region will be represented by its boundaries.

4.4.2 Step 2: Polygonal Approximation

The aim of the region boundary simplification step is to obtain a smooth curve over a minimum number of line segments describing the region's boundary. This process is referred to as the polygonal approximation of a polygonal curve which consists of a set of vertices. The approximation of polygonal curves aims at finding a subset of the original vertices so that a given objective function is minimized. The problem can be formulated in two ways:

- min-ϵ problem: Given N-vertex polygonal curve C, approximate it by another polygonal curve C_a with a given number of straight line segments M so that the approximation error is minimized.
- min-# problem: Given N-vertex polygonal curve C, approximate it by another polygonal curve C_a with a minimum number of straight line segments so that the error does not exceed a given maximum tolerance ϵ.

One of the most widely used polygonal approximation algorithm is a heuristic method called the Douglas-Peucker (DP) algorithm [37]. This algorithm considers the case of the min-# problem. In this work, the Douglas-Peucker (DP) algorithm is used to simplify the boundaries of the regions of interest before the application the Hough transform to extract signatures. The DP algorithm uses the closeness of a vertex to an edge segment. This algorithm works from the top down by starting with a crude initial guess at a simplified polygonal curve, namely the single edge joining the first and last vertices of the polygonal curve. Then the remaining vertices are tested for closeness to that edge. If there are vertices further than a specified tolerance, $\epsilon > 0$, away from the edge, then the vertex furthest from it is added to the simplification. This creates a new guess for the simplified polygonal curve. Using recursion, this process continues for each edge of the current guess until all vertices of the original polygonal curve are within tolerance of the simplification.

More specifically, in the DP algorithm, the two extreme endpoints of a polygonal curve are connected with a straight line as the initial rough approximation of the polygonal curve. Then, how well it approximates the whole polygonal curve is determined by computing the perpendicular distances from all intermediate polygonal curve vertices to that (finite) line segment. If all these distances are less than the specified tolerance ϵ, then the approximation is good, the endpoints are retained, and the other vertices can be discarded without the smoothed curve being worse than ϵ . However, if any of these distances exceeds the ϵ tolerance, then the approximation is not good enough. In this case, the point that is furthest away is chosen as a new vertex subdividing the original polygonal curve into two (shorter) polygonal curves. The procedure is repeated recursively on these two shorter polygonal curves. If at any time, all of the intermediate distances are less than the ϵ threshold, then all the intermediate points are discarded. The routine continues until all possible points have been discarded.

In the case of the approximation of the corpus callosum boundary as a closed curve, we have to find an optimal allocation of all approximation vertices including the starting point. A straightforward solution is to try all vertices as the starting points, and choose the one with minimal error. The complexity of this straightforward algorithm for a N-vertex curve is N times that of the algorithm for an open curve. There exist a number of heuristic approaches for selecting the starting point. In this work we adopted a heuristic approach founded on that presented in Sato [131]. In this approach, the farthest point from the centroid of the region of interest is chosen as the starting point.

The value of the tolerance ϵ affects the approximation of the original polygonal curves. For smaller values of tolerance, the polygonal curve is approximated by a large number of line segments M which means that the approximation is very similar to the original curve. While the larger values give a much coarser approximation of the original curve with smaller number of line segments M. Figure 4.5 shows an example of a simplification of the boundaries of a corpus callosum corresponding to tolerance $\epsilon = 0.9$ and number of line segments $M = 17$

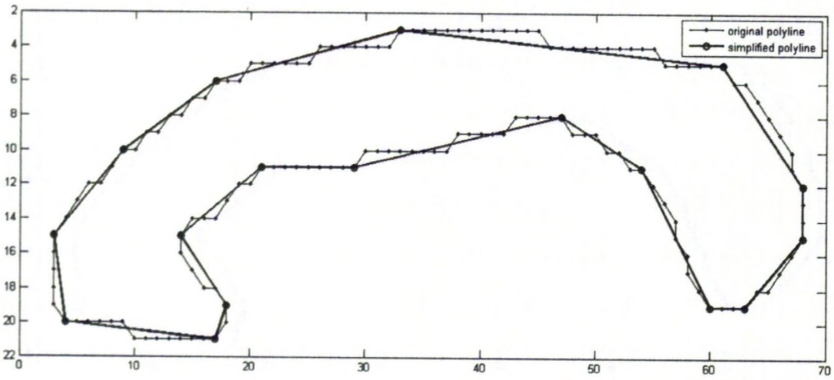

Figure 4.5: Polygonal approximation of corpus callosum corresponding to $\epsilon = 0.9$ and $M = 17$.

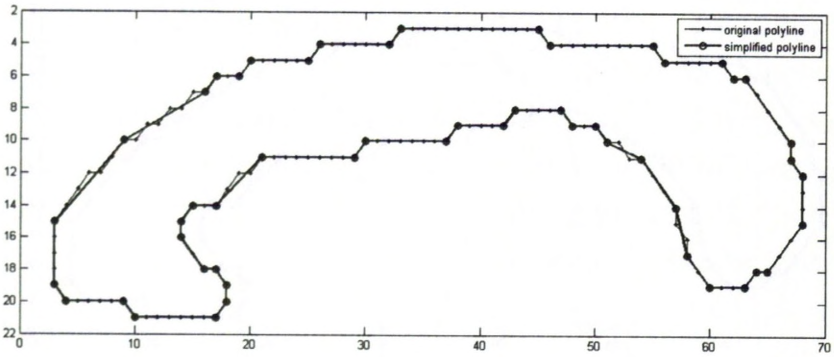

Figure 4.6: Polygonal approximation of corpus callosum corresponding to $\epsilon = 0.4$ and $M = 52$.

and Figure 4.6 shows another example of a simplification of the boundaries of the corpus callosum corresponding to tolerance $\epsilon = 0.4$ and number of line segments $M = 52$.

4.4.3 Step 3: Shape Signature Extraction

The generation of the shape signature based on the Straight Line Hough Transform (SLHT) relies on creating the $M \times N$ accumulator matrix A, where each row corresponds to one value of ρ, and each column to one value of θ. The procedure for generating the feature vector from the accumulator matrix is founded on that presented in Vlachos et al. [145] and is as follows:

1. Determine the set of boundary pixels corresponding to the region of interest.
2. Transform each pixel in the set into a parametric curve in the parameter space.
3. Increment the cells in the accumulator matrix A determined by the parametric curve.
4. Calculate a preliminary feature vector:
$$F_j = \sum_{i=1}^{M} A_{ij}^2(\rho, \theta), \quad j = 1..N$$
5. Calculate vector mean
$$\hat{\mu} = \frac{1}{N} \sum_{j=1}^{N} F_j$$
6. Normalize the feature vector:
$$FV_j(\theta) = \frac{F_j}{\hat{\mu}}, \quad j = 1..N$$

In (2) the transformation can be as in Equation 4.1, where (x, y) are the coordinates of the pixel to be transformed, and ρ and θ are the parameters of the corresponding line. Thus, every pixel (x, y) can be seen as a curve in the (ρ, θ) parameter space, where θ varies from the minimum to the maximum value, giving the corresponding ρ values. By transforming every point (x, y) in the image into the parameter space, the line parameters can be found in the intersections of the parametrized curves in the accumulator matrix as show in Figure 4.1. In step 4, the accumulator matrix is projected to a one-dimensional θ vector by summing up the ρ values in each column. Finally the feature vector is normalized according to its mean (5) and (6). The extracted feature vector describing the ROI within each image can then be used as an image signature.

4.4.4 Classification

The signatures from a labelled training set can thus be collected together and stored in a Case Base (CB) within a Case Based Reasoning (CBR) framework. Euclidean distance may then be used as a similarity measure in the context of a CBR framework. Let us assume that we have the feature vector T for a prelabelled image and the feature vector Q for the test image (both of size N). Their distance apart is calculated as:

$$dist(T,Q) = \sum_{j=1}^{N}(T_j - Q_j)^2$$

Here $dist = 0$ indicates identical images and $dist = dist_{max}$ indicates two images with maximum dissimilarity.

To categorise "unseen" MRI brain scans, according to the nature of the corpus callosum, signatures describing the unseen cases were compared with the signatures of labelled cases held in the CB. The well established K-Nearest Neighbour (KNN) technique was used to identify the most similar signature in the CB from which a class label was then be extracted.

4.5 Evaluation

The evaluation of the proposed image classification approach was undertaken in terms of classification accuracy, sensitivity and specificity. The three studies introduced in Chapter 3 were used for the investigation: (i) a comparison between musician and non-musician MRI scans, (ii) a comparison between left handedness and right handedness, and (iii) an epilepsy screening process. A description of the datasets was presented in Chapter 3.

As noted above, euclidean distance was used to calculate the similarity between the test image signature and the pre-labelled image signatures. The KNN

Table 4.1: TCV classification results for musicians study

	ϵ	Acc	Sens	Spec
V-HT	-	83.02	84.91	81.13
Poly-HT	0.1	83.02	84.91	81.13
Poly-HT	0.2	83.02	84.91	81.13
Poly-HT	0.3	83.02	84.91	81.13
Poly-HT	0.4	85.85	86.79	84.91
Poly-HT	0.5	87.74	88.68	86.79
Poly-HT	0.6	**91.51**	**92.45**	**90.57**
Poly-HT	0.7	86.79	88.68	84.91
Poly-HT	0.8	80.19	83.02	77.36
Poly-HT	0.9	77.36	75.47	79.25
Poly-HT	1	77.36	75.47	79.25

Table 4.2: TCV classification results for handedness study

	ϵ	Acc	Sens	Spec
V-HT	-	78.05	80.00	76.19
Poly-HT	0.1	79.27	82.50	76.19
Poly-HT	0.2	79.27	82.50	76.19
Poly-HT	0.3	81.71	87.50	76.19
Poly-HT	0.4	84.15	90.00	78.57
Poly-HT	0.5	84.15	90.00	78.57
Poly-HT	0.6	87.80	92.50	83.33
Poly-HT	0.7	**90.24**	**92.50**	**88.1**
Poly-HT	0.8	86.59	92.50	80.95
Poly-HT	0.9	75.61	82.50	69.05
Poly-HT	1	75.61	82.50	69.05

technique was used to identify the most similar signature in the CB from which a class label could be extracted. In the experiments, 1-NN was used to identify the most similar image signatures. Thus an unseen record is classified according to the "best match" discovered in the CB.

Tables 4.1 to 4.5 show the performance results, for the different datasets, obtained using the proposed approach compared to the original approach founded on Vlachos et al. [145]. Poly-HT refers to the proposed approach and V-HT refers to Vlachos. The performance of the Poly-HT approach is tested with different values of tolerance (ϵ). There is no value of the tolerance ϵ associated with the V-HT technique because it was applied to the original boundaries of the corpus callosum without the application of polygonal approximation. In the tables, Acc,

Table 4.3: TCV classification results for Ep_{106}

	ϵ	Acc	Sens	Spec
V-HT	-	66.98	69.81	64.15
Poly-HT	0.1	66.98	69.81	64.15
Poly-HT	0.2	66.98	69.81	64.15
Poly-HT	0.3	66.98	69.81	64.15
Poly-HT	0.4	68.87	71.70	66.04
Poly-HT	0.5	68.87	71.70	66.04
Poly-HT	0.6	69.81	71.70	67.92
Poly-HT	0.7	**72.64**	**71.70**	**73.58**
Poly-HT	0.8	65.09	67.92	62.26
Poly-HT	0.9	63.21	66.04	60.38
Poly-HT	1	63.21	66.04	60.38

Sens and Spec refer to accuracy, sensitivity and specificity respectively. Values indicated in bold font show the best results obtained in each case.

Inspection of Tables 4.1 and 4.5 indicates that the best classification accuracy achieved, using the proposed approach, was 91.51% coupled with a tolerance of $\epsilon = 0.6$ with respect to musician study, and 90.24% coupled with a tolerance of $\epsilon = 0.7$ with respect to handedness study. The proposed approach did not perform as well for the epilepsy study; the best classification accuracy was achieved using $\epsilon = 0.6$

Tables 4.1 to 4.5 indicate that the trend of the classification accuracy, for all datasets, improved as the value of ϵ was increased up to specific value (0.6 for the musician study, and 0.7 for the handedness and epilepsy studies), after which the classification accuracy begin to fall.

The time complexity of the image classification approach based on the Hough transform, using the three datasets (musician, handedness and Ep_{212}), is presented in Figure 4.7. All the experiments were performed with 1.86 GHz Intel(R) Core(TM)2 PC with 2GB RAM. The code was designed using Matlab 7. The run time includes the time required for the signature extraction process using the Hough transform coupled with a polygonal approximation, as well as the KNN classification.

Table 4.4: TCV classification results for Ep_{159}

	ϵ	Acc	Sens	Spec
V-HT	-	66.67	67.92	66.04
Poly-HT	0.1	66.67	67.92	66.04
Poly-HT	0.2	66.67	67.92	66.04
Poly-HT	0.3	66.67	67.92	66.04
Poly-HT	0.4	69.81	71.70	68.87
Poly-HT	0.5	71.70	73.58	70.75
Poly-HT	0.6	71.70	73.58	70.75
Poly-HT	0.7	**74.84**	**77.36**	**73.58**
Poly-HT	0.8	63.52	64.15	63.21
Poly-HT	0.9	63.52	64.15	63.21
Poly-HT	1	63.52	64.15	63.21

Table 4.5: TCV classification results for Ep_{212}

	ϵ	Acc	Sens	Spec
V-HT	-	67.92	73.58	62.26
Poly-HT	0.1	67.92	73.58	62.26
Poly-HT	0.2	67.92	73.58	62.26
Poly-HT	0.3	67.92	73.58	62.26
Poly-HT	0.4	70.75	76.42	65.09
Poly-HT	0.5	73.11	78.30	67.92
Poly-HT	0.6	73.11	78.30	67.92
Poly-HT	0.7	**76.42**	**81.13**	**71.70**
Poly-HT	0.8	67.45	72.64	62.26
Poly-HT	0.9	65.09	69.81	60.38
Poly-HT	1	65.09	69.81	60.38

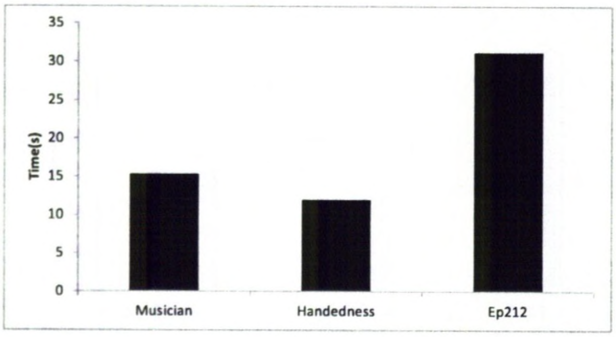

Figure 4.7: Run time complexity for the classification of different datasets.

4.6 Discussion

The overall performance accuracies presented in Section 4.5 above indicate that the proposed approach, based on the Hough transform coupled with the application of a polygonal approximation, outperformed the Vlachos approach.

The tolerance ϵ affected the performance of the proposed approach. The effectiveness of the classification of the proposed approach is nearly similar to the Vlachos approach when ϵ is small, because of the conjecture that a small ϵ produces a polygonal approximation of the corpus callosum that is nearly the same as the original, as shown in Figure 4.5. Consequently, the proposed approach acts like the Vlachos approach. When the value of ϵ is increased, the application of the polygonal approximation tends to simplify the boundary description of the corpus callosum. The results obtained indicate that the polygonal approximation maintains the necessary boundary details describing a corpus callosum. The amount of detail in the boundary description becomes coarser as the value of ϵ is further increased and the consequent classification performance starts to decrease (reference to medical domain experts has indicated that this is the case).

4.7 Summary

In this chapter a new approach to ROIBIC using the Hough transform, coupled with a polygonal approximation, has been described. The Hough transform is a popular technique used in image processing and analysis. Essentially it allows the translation of an image into a higher dimension which in turn facilitates the automated detection of objects. A number of variations of the Hough transform, directed at different types of shape, were considered. The technique of interest was that of Vlachos et al. which was used as the foundation for the proposed Hough transform classification process. The distinction between the two techniques is that the proposed technique adopted a polygonal approximation of the region of interest. The reported evaluation indicated that the proposed technique outperformed the Vlachos approach (which did not use any polygonal approximation). Reasonable classification results were obtained. However, in the following Chapter an alternative approach to classifying images according to a common image feature, founded on a tree representation, that outperforms the proposed Hough transform technique will be described.

Chapter 5

Region Of Interest Image Classification Using a Weighted Frequent Subgraph Representation

5.1 Introduction

As already noted, the application of techniques to classify image data according to some common object that features across an image set requires the representation of the image objects in question using some appropriate format. The previous chapter consider representing image objects using a signature generation process founded on the Hough transform. In this chapter an image decomposition method is considered whereby the ROIs are represented using a quad-tree representation. More specifically the Minimum Bounding Rectangles (MBR) surrounding the ROIs are represented using a quad-tree representation. The conjectured advantage offered is that a quad-tree representation will maintain the structural information (shape and size) of the ROI contained in the MBR. By applying a weighted frequent subgraph mining algorithm, gSpan-ATW [79], to this representation, frequent subgraphs that occur across the tree represented set of MBR can be identified. The identified frequent subgraphs each describing, in terms of size and shape, some part of the MBR, can then be used to form the fundamental elements of a feature space. Consequently, this feature space can be used to describe a set of feature vectors, one per image, to which standard classification processes can be applied (e.g. decision tree classifiers, SVM or rule based classifiers). A schematic of the graph based approach is given in Figure

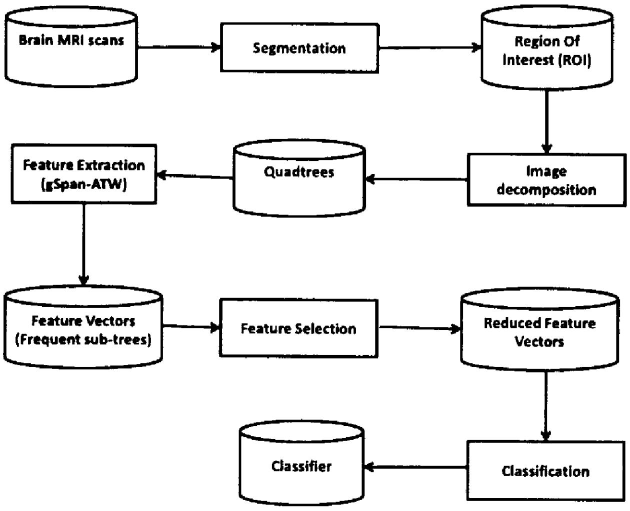

Figure 5.1: Framework of graph based approach.

From the Figure the graph based approach for image classification commences with segmentation and registration to isolate the Region Of Interest (ROI) as described in Chapter 3. Secondly, image decomposition takes place to represent the details of the identified ROI in terms of a quad-tree data structure. Feature extraction using a weighted frequent subgraph mining approach (gSpan-ATW) is then applied to the tree represented image set (one tree per image) to identify frequent subgraphs. The identified subtrees (subgraphs) then form the fundamental elements of a feature space, i.e. a set of attributes with which to describe the image set. Finally, due to a substantial number of features (frequent subgraphs) being generated, *feature selection* takes place to select the most relevant and discriminatory features. Standard classifier generation techniques can then be applied to build a classifier that can be applied to unseen data.

The rest of this chapter is organised as follows. Image decomposition using the quad tree generation process is presented in Section 5.2. Feature extraction, using the proposed weighted frequent subgraph mining algorithm (gSpan-ATW), is then described in Section 5.3. Feature selection and the final classification is then considered in Section 5.4. The evaluation of the proposed approach is presented in Section 5.5, followed by some discussion in Section 5.6 and a summary and some conclusions in Section 5.7.

5.2 Image Decomposition

Image decomposition methods are commonly used in image analysis, compression, and segmentation. There are different types of image decomposition methods, including quad-tree, pyramids, and the scale-space representation [29]. In this chapter, a quad-tree representation is proposed to characterize the ROI. A quad-tree is a tree data structure which can be used to represent a 2D area (such as images) which have been recursively subdivided into "quadrants" [92]. In the context of the representation of ROIs in terms of quad-tree, the pixels represented the MBR surrounding each ROI are tessellated into homogeneous sub-regions [43, 45]. The tessellation can be conducted according to a variety of image features such as colour or intensity. With respect to the corpus callosum a binary encoding was used, the "tiles" included in the corpus callosum were allocated a "1" (black) and the tiles not included a "0" (white). A tile was deemed to be sufficiently homogeneous if it was 95% black or white. As already noted, the tessellation process entails the recursive decomposing of the ROI, into quadrants. The tessellation continues until either sufficiently homogeneous tiles are identified or some user specified level of granularity is reached. The result is then stored in a quad-tree data structure such that each leaf node represent tiles. Leaf nodes nearer the root of the tree represent larger tiles than nodes further away. Thus the tree is "unbalanced" in that some leaf nodes will cover larger areas of the ROI than others. It is argued that tiles covering small regions are of greater interests than does covering large regions because they indicate a greater level of detail (they are typically located on the boundary of the ROI). The advantage of the representation is thus that it maintains information about the relative location and size of groups of pixels (i.e. the shape of the corpus callosum). The decomposition process is illustrated in Figures 5.2 and 5.3. Figure 5.2 illustrates the decomposition (in this case down to a level of 3), and Figure 5.3 illustrates the resulting quad-tree.

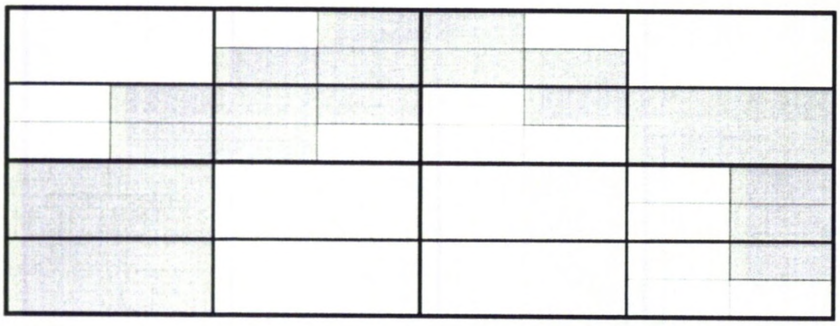

Figure 5.2: Hierarchical decomposition (tessellation) of the corpus callosum.

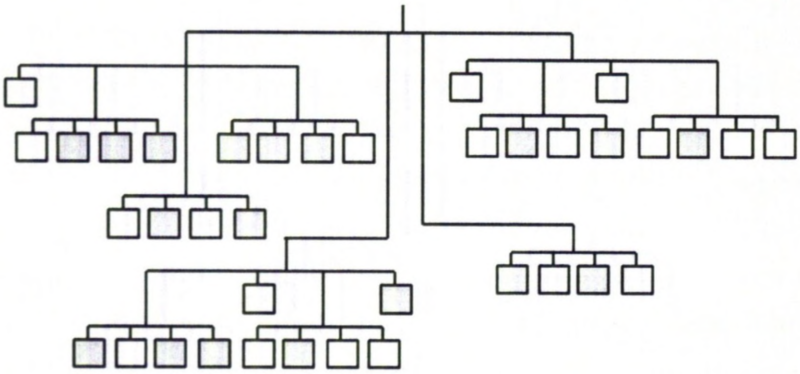

Figure 5.3: Tree representation of the hierarchical decomposition given in Figure 5.2.

5.3 Feature Extraction Using gSpan-ATW Algorithm

This section provides an overview of the weighted frequent subgraph mining algorithm, gSpan-ATW, adopted for use with the quad-tree representation described in Section 5.2. The section is divided into a number of sub-sections. Sub-section 5.3.1 first presents some necessary preliminary definitions. This is followed by Sub-section 5.3.2 that presents an overview of frequent subgraph mining and the gSpan algorithm on which gSpan-ATW is founded. The adopted weighted frequent subgraph mining process is then described in Sub-section 5.3.3.

5.3.1 Definitions

The necessary definitions to support the discussion on frequent subgraph mining presented in Sub-section 5.3.2 are introduced in this section. The definitions are presented as follows.

Labelled Graph: A labelled graph can be represented as $G(V, E, l_V, l_E, f_V, f_E)$, where V is a set of nodes, $E \subseteq V \times V$ is a set of edges; l_V and l_E are node and edge labels respectively, and f_V and f_E are the corresponding functions that define the mappings $V \rightarrow l_V$ and $E \rightarrow l_E$.

Subgraph: Given two graphs $G_1(V_1, E_1, l_{V_1}, l_{E_1}, f_{V_1}, f_{E_1})$ and $G_2(V_2, E_2, l_{V_2}, l_{E_2}, l_{V_2}, l_{E_2})$, G_1 is a subgraph of G_2, if G_1 satisfies the following conditions.

$$V_1 \subseteq V_2, \quad \forall v \in V_1, f_{V_1}(v) = f_{V_2}(v),$$

$$E_1 \subseteq E_2, \quad \forall (u,v) \in E_1, f_{E_1}(u,v) = f_{E_2}(u,v) \ .$$

G_2 is also called a supergraph of G_1 [76].

Graph Isomorphism: A graph $G_1(V_1, E_1, l_{V_1}, l_{E_1}, f_{V_1}, f_{E_1})$ is isomorphic to another graph $G_2(V_2, E_2, l_{V_2}, l_{E_2}, f_{V_2}, f_{E_2})$, if and only if a bijection $\psi : V_1 \rightarrow V_2$ exists such that:

$$\forall u \in V_1, \quad f_{V_1}(u) = f_{V_2}(\psi(u)),$$

$$\forall u, v \in V_1, (u,v) \in E_1 \Leftrightarrow (\psi(u), \psi(v)) \in E_2,$$

$$\forall (u,v) \in E_1, f_{E_1}(u,v) = f_{E_2}(\psi(u), \psi(v)).$$

The bijection ψ is an isomorphism between G_1 and G_2. A graph G_1 is *subgraph isomorphic* to a graph G_2, denoted by $G_1 \subseteq_{sub} G_2$, if and only if there exists a subgraph g of G_2 such that G_1 is isomorphic to g [72].

5.3.2 Frequent Subgraph Mining

From the literature (see also Chapter 2) two separate problem formulations for Frequent Subgraph Mining (FSM) can be identified: (i) *transaction graph based*, and (ii) *single graph based*. In transaction graph based mining, the input data comprises a collection of relatively small graphs, whereas in single graph based mining the input data comprises a very large single graph. The graph mining based approach described in this thesis focuses on transaction graph based mining. Table 5.1 lists the notation, in relation to transaction graph based mining, which will be employed through out the rest of this section (and where appropriate the rest of this thesis).

Table 5.1: Notation used throughout this chapter.

Notation	*Description*
$\mathcal{D}$	A graph database.
G_i	A transaction graph such that $G_i \in \mathcal{D}$.
k-(sub)graph	A (sub)graph of size k in terms of nodes, or edges, or paths.
g_k	A k-(sub)graph.
C_k	A set of subgraph candidates of size k .
F_k	A set of frequent k-subgraphs.
$\lvert \cdot \rvert$	The cardinality of a set.

In the context of transaction graph based mining, FSM aims to discover all the subgraphs whose occurrences in a graph database are over a user defined threshold. Formally, given a database $\mathcal{D}$ comprised of a collection of graphs and a threshold $\sigma (0 < \sigma \leq 1)$, the occurrence of a subgraph g in $\mathcal{D}$ is defined by $\delta_{\mathcal{D}}(g) = \{G_i \in \mathcal{D} | g \subseteq_{sub} G_i\}$. Thus, the *support* of a graph g is defined as the fraction of the graphs in $\mathcal{D}$ to which g is subgraph isomorphic:

$$sup_{\mathcal{D}}(g) = |\delta_{\mathcal{D}}(g)|/|\mathcal{D}| \tag{5.1}$$

A subgraph g is **frequent** if and only if $sup_{\mathcal{D}}(g) \geq \sigma$. The **frequent subgraph mining problem** is to find all the frequent subgraphs in $\mathcal{D}$. Frequent subgraph mining has been widely studied. A number of FSM algorithms have been proposed these include: (i) AGM [75], (ii) FSG [87], (iii) gSpan [155], (iv) FFSM [72]. The weighted frequent subgraph mining algorithm used with respect to the representation described here was founded on gSpan [155]. An outline of the gSpan algorithm is given in Algorithm 5.1, note that the algorithm recursively calls the "subGM" procedure. In the procedure, when subGM runs each time, it grows one edge from c and discovers all frequent children of c (lines 6 to 12). The recursive procedure in subGM follows the pre-order traversal as described in [155].

```
Algorithm 5.1: gSpan($c$, $\sigma$, $\mathcal{D}$, $F$)
   Input: $c$ = a subgraph represented by a DFS code, $\sigma$ = minimum
          support, $\mathcal{D}$ = a graph dataset
   Output: $\mathcal{F}$, a set of frequent subgraphs
 1 Sort labels of the nodes and edges in $\mathcal{D}$ by their frequency
 2 Remove infrequent nodes and edges
 3 Relabel the remaining nodes and edges in descending frequency
 4 $F_1 \leftarrow$ {all frequent 1-edge subgraphs in $\mathcal{D}$}
 5 Sort $F_1$ in DFS lexicographic order
 6 $\mathcal{F} \leftarrow \emptyset$
 7 foreach $c \in F_1$ do
 8     subGM($c, \mathcal{D}, \sigma, \mathcal{F}$)
 9     $\mathcal{D} \leftarrow \mathcal{D} - c$
10     if $|\mathcal{D}| < \sigma$ then
11         break
12     end
13 end
```

Frequent subgraph mining is computationally expensive because of the candidate generation and support computation processes that are required. The first process is concerned with the generation of candidate subgraphs in a non-redundant manner such that the same graph is not generated more than once. Thus graph isomorphism checking is required to remove duplicate graphs. The second process is to compute the support of a graph in the graph database. This also requires subgraph isomorphism checking in order to determine the set of graphs where a given candidate occurs. As mentioned in [155], using an efficient canonical labelling and a lexicographical ordering in graphs, gSpan was designed to reduce the generation of duplicate graphs. As shown in Procedure subGM, $c \neq min(c)$ (line 1) guarantees that gSpan does not extend any duplicate graph

Procedure subGM(c, $\mathcal{D}$, σ, $\mathcal{F}$)

```
1  if $c \neq min(c)$ then
2      return
3  end
4  $\mathcal{F} \leftarrow \mathcal{F} \cup \{c\}$
5  $C_k \leftarrow \emptyset$
6  Scan $\mathcal{D}$ once, find every edge $e$ such that $c$ can be right-most extended to
   $c \cup e$, $C_k \leftarrow c \cup e$
7  Sort $C_k$ in DFS lexicographic order
8  foreach $g_k \in C_k$ do
9      if $support(g_k) \geq \sigma$ then
10         subGM($g_k$, $\mathcal{D}$, $\sigma$, $\mathcal{F}$)
11     end
12 end
```

because the candidate generation process adheres to a canonical labelling. Further, the rightmost extension shown at line 6 in Procedure subGM guarantees that the complete set of frequent subgraphs will be discovered. Although gSpan can achieve competitive performance compared with other FSM algorithms, its performance degrades considerably when the graph size is relatively large or the graph features few node and/or edge labels. One mechanism for addressing this issue is to use weighted frequent subgraph mining.

5.3.3 Weighted Frequent Subgraph Mining

Given the quad-tree representation advocated in Section 5.2, a weighted frequent subgraph mining algorithm (gSpan-ATW) was applied to identify frequently occurring subgraphs (subtrees) within this tree representation. The Average Total Weighting (ATW) scheme weights nodes according to their occurrence count. The nodes in the tree (see for example Figure 5.3) are labelled as being either: "black", "white" or "nothing". The black and white labels are used for the leaf nodes and represent the shape of the corpus callosum. These should therefore be weighted more highly than the "nothing" nodes. It can also be argued that these should be weighted more highly because they are further away (on average) from the root than the "nothing" nodes, and therefore the leaf nodes can be said to provide more detail. The ATW scheme achieves this and is described in more detail in the following sub-section.

5.3.3.1 The Average Total Weighting (ATW) Scheme

The weighting scheme adopted in the gSpan-ATW algorithm is the Average Total Weighting (ATW) scheme [79], which in turn is inspired by the work of [140]. Given a graph data set $\mathcal{D} = \{G_1, G_2, \cdots, G_t\}$, the weight for a subgraph g is calculated by dividing the sum of the average weights in the graphs that contain g with the sum of the average weights across the entire graph data set $\mathcal{D}$. Thus:

Definition 5.3.1. *Given a graph data set $\mathcal{D} = \{G_1, G_2, \cdots, G_t\}$, if G_i is node weighted by assigning $\{w_1, w_2, \cdots, w_k\}$ to a set of nodes $\{v_1, v_2, \cdots, v_k\}$ respectively, then the average weight associated with G_i is defined as:*

$$W_{avg}(G_i) = \frac{\sum_{j=1}^{k} w_j}{k} \ . \tag{5.2}$$

Where w_j can be determined using an appropriate weighting function described as follows:

$$w_j = \frac{occ(v_j)}{\sum_{1 \le i \le t} size(G_i)} \ . \tag{5.3}$$

Where $occ(v_j)$ denotes the number of times v_j occurs in $\mathcal{D}$, and $size(G_i)$ denotes the size of G_i in terms of the number of nodes in G_i. Thus, the total weight of $\mathcal{D}$ is further defined as:

$$W_{sum}(\mathcal{D}) = \sum_{i=1}^{t} W_{avg}(G_i) \ . \tag{5.4}$$

Using both (5.2) and (5.4), the weight of a subgraph can be calculated by (5.5).

Definition 5.3.2. *Given a graph data set $\mathcal{D} = \{G_1, G_2, \cdots G_t\}$ and an arbitrary subgraph g, let the set of graphs where g occurs equal $\delta_{\mathcal{D}}(g)$. Then, the weight of g with respect to $\mathcal{D}$ is:*

$$W_{\mathcal{D}}(g) = \frac{\sum_{G_i \in \delta_{\mathcal{D}}(g)} W_{avg}(G_i)}{W_{sum}(\mathcal{D})} \ . \tag{5.5}$$

$W_{\mathcal{D}}(g)$ is used to quantify the actual importance of each discovered subgraph g in a graph database. According to (5.1), the weighted support of a subgraph g is then defined as the product of the support of g and the importance factor of g:

$$wsup_{\mathcal{D}}(g) = W_{\mathcal{D}}(g) \cdot sup_{\mathcal{D}}(g) = \frac{W_{\mathcal{D}}(g) \cdot |\delta_{\mathcal{D}}(g)|}{|\mathcal{D}|} \ . \tag{5.6}$$

Definition 5.3.3. *A subgraph g is weighted frequent with respect to* $\mathcal{D}$, *if* $wsup_{\mathcal{D}}(g) \geq \tau$, *where* $0 < \tau \leq 1$ *is a weighted support threshold.*

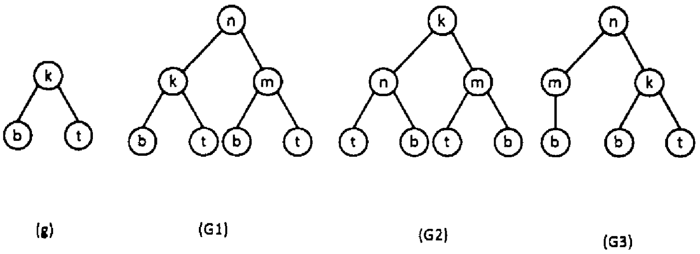

Figure 5.4: An example of calculating weights by the ATW scheme.

Example: Considering the graph data set $\mathcal{D} = \{G_1, G_2, G_3\}$ shown in Figure 5.4, where the symbol inside each node indicates the node label (the edge labels are not included in the figure). Given a node with a label 'b' in the candidate subgraph g (in Figure 5.4), $occ(b) = 6$, and $\sum_{i=1}^{3} size(G_i) = 20$. Thus $w_{\mathcal{D}}(b) = 6/20 = 0.3$. Similarly, for nodes with labels 't', 'n', 'm' and 'k' in $\mathcal{D}$, the nodes weights are $w_{\mathcal{D}}(t) = 5/20 = 0.25$, $w_{\mathcal{D}}(n) = 3/20 = 0.15$, $w_{\mathcal{D}}(m) = 3/20 = 0.15$, $w_{\mathcal{D}}(k) = 3/20 = 0.15$ respectively. Given a subgraph g, which occurs in G_1 and G_3, $W_{avg}(G_1) = \frac{0.15+0.15+0.15+0.25+0.3+0.3+0.25}{7} \approx 0.2214$, $W_{avg}(G_2) = \frac{0.15+0.15+0.15+0.25+0.3+0.25+0.3}{7} \approx 0.2214$, $W_{avg}(G_3) = \frac{0.15+0.15+0.15+0.3+0.3+0.25}{6} \approx 0.2167$. Thus, $W_{sum}(\mathcal{D}) = 0.2214 + 0.2214 + 0.2167 \approx 0.6595$, $W_{\mathcal{D}}(g) = \frac{0.2214+0.2167}{0.6595} \approx 0.6643$, $wsup_{\mathcal{D}} = 2/3 \times W_{\mathcal{D}}(g) \approx 0.4429$

5.3.3.2 The gSpan-ATW Algorithm

The ATW weighting scheme was incorporated into the gSpan algorithm to produce gSpan-ATW. Since only the procedure 'subGM' as described in Section 5.3.2 needed to be modified, the procedure of integrating ATW into the revised version of gSpan required this procedure to be replaced with 'subgSpan-ATW'. The procedure is presented below. In the procedure, a weighted support threshold τ is introduced to replace the threshold σ used in Algorithm 5.1. The input to gSpan-ATW is a collection of graphs $\mathcal{D}$ (in our case $\mathcal{D}$ comprises a collection of trees each representing a corpus callosum). The gSpan-ATW algorithm operates in a depth first manner, level by level, following a "generate, calculate support, and prune" loop. A candidate subgraph, g, is considered to be frequent if its weighted support, $wsup_{\mathcal{D}}(g)$, is greater than some user specified threshold, τ; otherwise it is pruned. Note that the lower the value of τ the greater the number of frequent subgraphs that will be identified.

Procedure subgSpan-ATW(c, $\mathcal{D}$, τ, $\mathcal{F}$)

```
if $c \neq min(c)$ then
    return
end
if $W_{\mathcal{D}}(c) \times sup_{\mathcal{D}}(c) \geq \tau$ then
    $\mathcal{F} \leftarrow \mathcal{F} \cup \{c\}$
else
    return
end
$C \leftarrow \emptyset$
Scan $\mathcal{D}$ once, find every edge $e$ such that $c$ can be right-most extended to
  $c \cup e$, $C \leftarrow c \cup e$
Sort $C$ in DFS lexicographic order
foreach $g_k \in C$ do
    if $W_{\mathcal{D}}(g_k) \times sup_{\mathcal{D}}(g_k) \geq \tau$ then
        subgSpan-ATW($g_k$, $\mathcal{D}$, $\tau$, $\mathcal{F}$)
    end
end
```

The identified frequent subgraphs (i.e. subtrees) each describing, in terms of size and shape, some part of a ROI that occurs regularly across the data set, are then used to form the fundamental elements of a feature space. In this context a feature space is an N dimensional shape where N is equivalent to the number of features identified. Using this feature space each image (ROI) can be described in terms of a feature vector of length N, with each element having a value equal to the frequency of that feature.

5.4 Feature Selection and Classification

As noted above the graph mining process typically identifies a great many frequent subgraphs; more than required for the desired classification. Therefore a feature selection strategy was applied to the feature space so that only those subgraphs that serve as good discriminators between cases are retained. A straightforward wrapper method was adopted whereby a decision tree generator was applied to the feature space. Features included as "choice points" in the decision tree were then selected, while all remaining features were discarded. For the work described here, the well established C4.5 algorithm [122] was adopted, although any other decision tree generator would have sufficed. On completion of the feature selection process each image was described in terms of a reduced feature vector indicating the selected features (subgraphs) that appear in the image. Once the image set had been represented in this manner any appropriate classifier generator could be applied. With respect to the work described here two classification techniques were used for the evaluation: (i) Decision Trees (C4.5) [122] and (ii) Support Vector Machines (SVMs) [28], to examine the performance of the graph based approach. For the C4.5 classifiers, the WEKA implementations [60] were used, and for the SVM classifier, the LIBSVM implementation [22] was used. In the experiments, all the classification results were computed using Ten-fold Cross Validation (TCV).

5.5 Evaluation

The proposed graph based image classification approach was evaluated with respect to the corpus callosum application. This section describes the evaluation. The evaluation was undertaken in terms of classification accuracy, sensitivity and specificity. The three studies introduced earlier were used for the evaluation: (i) comparison between musician and non-musician MRI scans, (ii) comparison between left handedness and right handedness, and (iii) epilepsy screening. The description of these datasets was presented in Chapter 3. The result of three evaluations are discussed in detail in Sub-sections 5.5.1, 5.5.2 and 5.5.3 below. The effect of the feature selection technique is considered in Subsection 5.5.4. The run time analysis of the proposed approach is presented in Subsection 5.5.5

5.5.1 Musicians Study

For the musicians study four graph datasets were generated: QT-D4, QT-D5, QT-D6, and QT-D7. These four datasets represent the same collection of brain

Table 5.2: TCV classification results for QT-D4 data of musician study.

τ			SVM			C4.5		
%	F_{before}	F_{after}	Acc.	Sens.	Spec.	Acc.	Sens.	Spec.
20	24549	15	71.70	69.81	73.58	70.75	71.70	69.81
30	4264	16	71.70	69.81	73.58	69.81	71.70	67.92
40	1193	18	**73.58**	**71.70**	**75.47**	68.87	71.70	66.04
50	639	19	69.81	71.70	67.92	**71.70**	**73.58**	**69.81**
60	262	16	66.98	69.81	64.15	68.87	71.70	66.04
70	151	21	61.32	62.26	60.38	61.32	62.26	60.38
80	86	16	62.26	66.04	58.49	52.83	56.60	49.06
90	54	17	58.49	62.26	54.72	50.94	54.72	47.17

MRI scans but with different levels of quad-tree decomposition (4, 5, 6 and 7 respectively). The number of trees in each of the dataset is of course the same (one tree per image). However, the trees in QT-D7 have more nodes and edges than those in QT-D6 which have more nodes and edges than those in QT-D5. QT-D4 have the least number of nodes and edges compared to the other datasets: QT-D5, QT-D6, and QT-D7.

Tables 5.2 to 5.5 show the TCV results obtained using the musician dataset. The SVM and C4.5 columns indicate the results using the SVM and C4.5 classification techniques respectively. Acc, Sens and Spec refer to accuracy, sensitivity and specificity respectively. The F_{before} and F_{after} indicate the number of features before and after the application of feature selection. τ indicates the support threshold which is the minimum frequency with which a subgraph must occur across the dataset for the subgraph to be considered "frequent". Results indicated in bold font show the best results obtained in each case.

Inspect of tables 5.2 to 5.5 indicates that the best accuracies achieved were 91.51% (SVM) and 95.28% (C4.5). The best sensitivity and specificity were 92.45% and 90.57% (SVM) and 96.23% and 94.34% (C4.5). The best accuracy obtained using the two classifier SVM and C4.5 occurred when using QT-D6 coupled with a support threshold of $\tau = 30$.

From the tables it can also be observed that the best classification accuracies obtained using SVM were 73.58%, 82.08%, 91.51% and 89.62% corresponding to the different quad-tree levels of 4, 5, 6, and 7 respectively. While the best classification accuracy obtained using C4.5 were 71.70%, 90.57%, 95.28% and 89.62% corresponding to quad-tree levels of 4, 5, 6, and 7 respectively.

Table 5.3: TCV classification results for QT-D5 data of musician study.

τ			SVM			C4.5		
%	F_{before}	F_{after}	Acc.	Sens.	Spec.	Acc.	Sens.	Spec.
20	16094	12	76.42	79.25	73.58	**90.57**	**92.45**	**88.68**
30	4630	12	**82.08**	**84.91**	**79.25**	83.96	86.79	81.13
40	2100	10	80.19	83.02	77.36	80.19	83.02	77.36
50	1155	13	79.25	83.02	75.47	85.85	86.79	84.91
60	637	14	78.30	81.13	75.47	80.19	83.02	77.36
70	405	14	78.30	81.13	75.47	81.13	83.02	79.25
80	252	18	73.58	67.92	79.25	80.19	83.02	77.36
90	130	17	67.92	69.81	66.04	70.75	73.58	67.92

Table 5.4: TCV classification results for QT-D6 data of musician study.

τ			SVM			C4.5		
%	F_{before}	F_{after}	Acc.	Sens.	Spec.	Acc.	Sens.	Spec.
20	35223	11	85.85	86.79	84.91	85.85	86.79	84.91
30	9461	10	**91.51**	**92.45**	**90.57**	**95.28**	**96.23**	**94.34**
40	4059	12	86.79	92.45	81.13	84.91	86.79	83.02
50	2260	11	82.08	84.91	79.25	83.96	86.79	81.13
60	1171	11	84.91	88.68	81.13	90.57	92.45	88.68
70	741	13	79.25	86.79	71.70	83.96	86.79	81.13
80	433	13	78.30	81.13	75.47	77.36	75.47	79.25
90	232	14	74.53	71.70	77.36	75.47	73.58	77.36

Table 5.5: TCV classification results for QT-D7 data of musician study.

τ			SVM			C4.5		
%	F_{before}	F_{after}	Acc.	Sens.	Spec.	Acc.	Sens.	Spec.
20	48683	13	88.68	90.57	86.79	83.96	86.79	81.13
30	34440	12	**89.62**	**92.45**	**86.79**	85.85	86.79	84.91
40	11998	11	86.79	92.45	81.13	**89.62**	**90.57**	**88.68**
50	6402	10	83.96	86.79	81.13	86.79	88.68	84.91
60	3317	13	82.08	84.91	79.25	87.74	88.68	86.79
70	2032	13	78.30	81.13	75.47	75.47	73.58	77.36
80	1117	13	73.58	67.92	79.25	76.42	79.25	73.58
90	476	12	71.70	73.58	69.81	78.3	81.13	75.47

Table 5.6: TCV classification results for QT-D4 data of handedness study.

τ			SVM			C4.5		
%	F_{before}	F_{after}	Acc.	Sens.	Spec.	Acc.	Sens.	Spec.
20	9245	22	68.29	75.00	61.90	67.07	72.50	61.90
30	2875	14	70.73	77.50	64.29	68.29	75.00	61.90
40	1424	13	**73.17**	**80.00**	**66.67**	69.51	75.00	64.29
50	745	14	71.95	77.50	66.67	**70.73**	**77.50**	**64.29**
60	324	15	68.29	75.00	61.90	67.07	72.50	61.90
70	278	19	63.41	70.00	57.14	59.76	65.00	54.76
80	167	15	62.20	65.00	59.52	51.22	57.50	45.24
90	42	16	57.32	62.50	52.38	48.78	52.50	45.24

From these results it can also be observed that accuracy increases as the quad-tree levels are increased, up to level 6, and then begins to fall of. It is conjectured that this is because "over fitting" starts to take place as the quad-tree representation starts to get to be too detailed.

Regardless of the quad-tree level, the trend of the classification accuracy improved as the threshold support decreased. This is because more frequent subgraphs are identified as can be seen from the F_{before} column. It is likely that as the support threshold increases, significant subgraphs are no longer discovered by the graph mining algorithm.

5.5.2 Handedness Study

For the handedness study four graph datasets were again generated: QT-D4, QT-D5, QT-D6, and QT-D7. These four datasets represent the same collection of brain MRI scan but with different levels of quad-tree decomposition (4, 5, 6 and 7 respectively).

Tables 5.6 to 5.9 show the TCV results obtained using the handedness dataset. The column headings should be interpreted in the same way as for Table 5.2. From tables 5.6 to 5.9 it can be seen that the best accuracy achieved was 91.46% (SVM) and 93.90% (C4.5). The best sensitivity and specificity were 92.50% and 90.48% (SVM) and 95.00% and 92.86% (C4.5). The best accuracy obtained using the SVM classifier occurred when using QT-D6 coupled with support threshold of $\tau = 20$. While The best accuracy obtained using C4.5 occurred when using QT-D6 coupled with a support threshold of $\tau = 30$.

Tables 5.6 to 5.9 indicate that the best classification accuracy obtained using

Table 5.7: TCV classification results for QT-D5 data of handedness study.

τ			SVM			C4.5		
%	F_{before}	F_{after}	Acc.	Sens.	Spec.	Acc.	Sens.	Spec.
20	14223	25	73.17	77.50	69.05	78.05	80.00	76.19
30	3974	16	**87.80**	**92.50**	**83.33**	82.93	87.50	78.57
40	1997	14	85.37	87.50	83.33	**89.02**	**95.00**	**83.33**
50	975	17	82.93	87.50	78.57	84.15	90.00	78.57
60	592	19	78.05	80.00	76.19	79.27	82.50	76.19
70	387	22	75.61	82.50	69.05	78.05	80.00	76.19
80	235	14	73.17	80.00	66.67	78.05	80.00	76.19
90	77	16	68.29	75.00	61.90	69.51	75.00	64.29

Table 5.8: TCV classification results for QT-D6 data of handedness study.

τ			SVM			C4.5		
%	F_{before}	F_{after}	Acc.	Sens.	Spec.	Acc.	Sens.	Spec.
20	26341	28	**91.46**	**92.50**	**90.48**	84.15	90.00	78.57
30	8362	15	85.37	92.50	78.57	**93.90**	**95.00**	**92.86**
40	3861	17	81.71	87.50	76.19	89.02	95.00	83.33
50	1870	14	84.15	90.00	78.57	84.15	90.00	78.57
60	963	16	78.05	80.00	76.19	82.93	87.50	78.57
70	602	14	78.05	80.00	76.19	79.27	82.50	76.19
80	367	13	71.95	72.50	71.43	75.61	82.50	69.05
90	137	17	69.51	75.00	64.29	74.39	80.00	69.05

SVM were 73.17%, 87.80%, 91.46% and 85.37% corresponding to different quad-tree levels of 4, 5, 6, and 7 respectively. While the best classification accuracy obtained using C4.5 were 70.73%, 89.02%, 93.90% and 87.80% corresponding to quad-tree levels of 4, 5, 6, and 7 respectively.

From these results, as in the case of the musicians study, it can again be observed that accuracy increases as the number of quad-tree levels are increased, up to a level of 6, and then begins to fall of. As noted previously it is conjectured that this is because "over fitting" starts to take place as the quad-tree representation starts to get to be too detailed. Also as noted before, regardless of the quad-tree level, the trend of the classification accuracy improved as the threshold support decreased because more frequent subgraphs are identified (as can be seen from the F_{before} columns).

Table 5.9: TCV classification results for QT-D7 data of handedness study.

τ			SVM			C4.5		
%	F_{before}	F_{after}	Acc.	Sens.	Spec.	Acc.	Sens.	Spec.
20	36781	25	82.93	87.50	78.57	82.93	87.50	78.57
30	28744	22	**85.37**	**92.50**	**78.57**	84.15	90.00	78.57
40	9456	17	81.71	87.50	76.19	**87.80**	**92.50**	**83.33**
50	4207	15	76.83	77.50	76.19	86.59	92.50	80.95
60	2421	12	74.39	80.00	69.05	85.37	92.50	78.57
70	1611	14	67.07	72.50	61.90	76.83	77.50	76.19
80	936	13	64.63	70.00	59.52	74.39	80.00	69.05
90	255	15	62.20	67.50	57.14	71.95	77.50	66.67

Table 5.10: TCV classification results for QT-D4 data of Ep_{106}.

τ			SVM			C4.5		
%	F_{before}	F_{after}	Acc.	Sens.	Spec.	Acc.	Sens.	Spec.
20	6471	35	61.32	62.26	60.38	56.60	62.26	50.94
30	2411	32	**64.15**	**66.04**	**62.26**	59.43	58.49	60.38
40	1721	28	60.38	60.38	60.38	**61.32**	**62.26**	**60.38**
50	1193	29	56.60	62.26	50.94	58.49	62.26	54.72
60	476	25	54.72	58.49	50.94	59.43	58.49	60.38
70	282	19	54.72	58.49	50.94	56.60	62.26	50.94
80	127	17	51.89	54.72	49.06	53.77	58.49	49.06
90	87	15	50.94	56.60	45.28	51.89	54.72	49.06

5.5.3 Epilepsy Study

For the epilepsy study three data collections (Ep_{106}, Ep_{159}, Ep_{212}) with different sizes (106, 159 and 212 respectively) were used. Each of these three collections was used to generate four datasets (QT-D4, QT-D5, QT-D6, and QT-D7) giving a total of 12 datasets.

Tables 5.10 to 5.21 show the TCV results obtained using the three epilepsy collections. The column headings should be interpreted in the same way as for Table 5.2. From tables 5.10 to 5.21 it can be seen that the best accuracy of achieved was 84.91% (C4.5), 86.16 (SVM) and 86.32% (C4.5) for the three collections Ep_{106}, Ep_{159}, and Ep_{212} respectively. High sensitivity and specificity were also achieved, associated with the corresponding best accuracies obtained. The best accuracy obtained using the SVM and C4.5 occurred when using QT-D6 coupled with a support threshold of $\tau = 30$. Best results were obtained using the larger, 212 Epilepsy MRI scan data collection because this included many more

Table 5.11: TCV classification results for QT-D5 data of Ep_{106}.

τ			SVM			C4.5		
%	F_{before}	F_{after}	Acc.	Sens.	Spec.	Acc.	Sens.	Spec.
20	3567	37	79.25	86.79	71.70	73.58	71.70	75.47
30	1944	35	**83.02**	**86.79**	**79.25**	78.30	81.13	75.47
40	849	37	82.08	86.79	77.36	**81.13**	**83.02**	**79.25**
50	478	29	79.25	86.79	71.70	79.25	81.13	77.36
60	312	27	73.58	69.81	77.36	72.64	71.70	73.58
70	165	20	69.81	71.70	67.92	66.04	69.81	62.26
80	102	19	67.92	69.81	66.04	62.26	66.04	58.49
90	78	21	64.15	67.92	60.38	57.55	60.38	54.72

Table 5.12: TCV classification results for QT-D6 data of Ep_{106}.

τ			SVM			C4.5		
%	F_{before}	F_{after}	Acc.	Sens.	Spec.	Acc.	Sens.	Spec.
20	16934	39	82.08	86.79	77.36	76.42	79.25	73.58
30	9841	33	**84.91**	**88.68**	**81.13**	**84.91**	**86.79**	**83.02**
40	6104	28	81.13	83.02	79.25	79.25	81.13	77.36
50	4201	27	78.30	81.13	75.47	72.64	71.70	73.58
60	983	19	73.58	69.81	77.36	66.04	69.81	62.26
70	755	16	69.81	71.70	67.92	66.04	69.81	62.26
80	503	14	66.98	69.81	64.15	62.26	66.04	58.49
90	212	12	64.15	67.92	60.38	60.38	60.38	60.38

Table 5.13: TCV classification results for QT-D7 data of Ep_{106}.

τ			SVM			C4.5		
%	F_{before}	F_{after}	Acc.	Sens.	Spec.	Acc.	Sens.	Spec.
20	38712	43	71.70	73.58	69.81	74.53	71.70	77.36
30	19837	35	**76.42**	**79.25**	**73.58**	**77.36**	**75.47**	**79.25**
40	10798	37	68.87	75.47	62.26	73.58	71.70	75.47
50	6499	37	66.04	69.81	62.26	69.81	73.58	66.04
60	4634	39	68.87	75.47	62.26	62.26	66.04	58.49
70	2100	26	62.26	66.04	58.49	57.55	60.38	54.72
80	1586	18	61.32	62.26	60.38	58.49	62.26	54.72
90	622	15	56.60	62.26	50.94	54.72	58.49	50.94

Table 5.14: TCV classification results for QT-D4 data of Ep_{159}.

τ			SVM			C4.5		
%	F_{before}	F_{after}	Acc.	Sens.	Spec.	Acc.	Sens.	Spec.
20	6723	36	57.23	58.49	56.60	59.12	60.38	58.49
30	2405	32	**60.38**	**62.26**	**59.43**	61.01	62.26	60.38
40	1657	29	58.49	56.60	59.43	**62.26**	**66.04**	**60.38**
50	1203	29	55.35	56.60	54.72	59.12	60.38	58.49
60	498	25	57.23	58.49	56.60	55.97	56.60	55.66
70	286	22	50.94	49.06	51.89	52.20	50.94	52.83
80	135	17	50.31	49.06	50.94	52.20	50.94	52.83
90	92	16	50.31	49.06	50.94	50.94	49.06	51.89

Table 5.15: TCV classification results for QT-D5 data of Ep_{159}.

τ			SVM			C4.5		
%	F_{before}	F_{after}	Acc.	Sens.	Spec.	Acc.	Sens.	Spec.
20	9435	43	81.13	86.79	78.30	76.10	79.25	74.53
30	3870	38	81.13	86.79	78.30	**79.87**	**84.91**	**77.36**
40	1978	32	**82.39**	**88.68**	**79.25**	74.21	75.47	73.58
50	911	32	77.36	81.13	75.47	70.44	71.70	69.81
60	523	27	73.58	75.47	72.64	64.15	64.15	64.15
70	334	24	75.47	77.36	74.53	65.41	67.92	64.15
80	182	18	69.81	71.70	68.87	61.64	62.26	61.32
90	124	15	65.41	67.92	64.15	59.12	60.38	58.49

Table 5.16: TCV classification results for QT-D6 data of Ep_{159}.

τ			SVM			C4.5		
%	F_{before}	F_{after}	Acc.	Sens.	Spec.	Acc.	Sens.	Spec.
20	17736	39	83.02	88.68	80.19	79.25	84.91	76.42
30	10005	32	**86.16**	**94.34**	**82.08**	**84.91**	**92.45**	**81.13**
40	6430	26	84.91	92.45	81.13	81.13	86.79	78.30
50	4309	24	83.02	88.68	80.19	82.39	88.68	79.25
60	1012	16	80.50	86.79	77.36	78.62	83.02	76.42
70	874	13	73.58	75.47	72.64	74.21	75.47	73.58
80	551	15	71.07	73.58	69.81	69.18	69.81	68.87
90	244	16	67.92	69.81	66.98	68.55	69.81	67.92

Table 5.17: TCV classification results for QT-D7 data of Ep_{159}.

τ			SVM			C4.5		
%	F_{before}	F_{after}	Acc.	Sens.	Spec.	Acc.	Sens.	Spec.
20	39008	45	76.73	79.25	75.47	69.81	71.70	68.87
30	20905	38	**79.25**	**84.91**	**76.42**	71.07	73.58	69.81
40	11988	42	76.73	79.25	75.47	**77.99**	**81.13**	**76.42**
50	6959	37	74.21	75.47	73.58	75.47	77.36	74.53
60	4814	41	69.81	71.70	68.87	75.47	77.36	74.53
70	2165	29	65.41	67.92	64.15	67.92	69.81	66.98
80	1602	19	61.01	62.26	60.38	62.26	66.04	60.38
90	638	17	58.49	56.60	59.43	57.86	58.49	57.55

Table 5.18: TCV classification results for QT-D4 data of Ep_{212}.

τ			SVM			C4.5		
%	F_{before}	F_{after}	Acc.	Sens.	Spec.	Acc.	Sens.	Spec.
20	6814	38	62.26	66.98	57.55	59.43	62.26	56.60
30	2454	34	**66.04**	**69.81**	**62.26**	61.32	65.09	57.55
40	1692	29	64.15	68.87	59.43	**63.21**	**67.92**	**58.49**
50	1265	31	62.26	66.98	57.55	60.38	64.15	56.60
60	514	23	58.49	62.26	54.72	60.38	64.15	56.60
70	293	19	56.60	59.43	53.77	52.36	53.77	50.94
80	141	15	51.89	53.77	50.00	44.34	46.23	42.45
90	99	13	51.89	53.77	50.00	42.45	44.34	40.57

training examples.

Inspection of tables 5.10 to 5.21 again indicates that accuracy increases as the quad-tree levels are increased, up to level of 6, and then begins to fall of as "over fitting" starts to take place. The overall accuracy results obtained using the epilepsy data collection is less than those obtained using musician and handedness datasets. This was also observed with respect to the Hough transform technique described in Chapter 4. It is suggested that the reason for this is that epilepsy is also infulenced by other conditions in addition to the size and shape of the corpus callosum.

5.5.4 The Effect of Feature Selection

The results where feature selection was not applied were not as good as those obtained using the proposed feature selection technique. Table 5.22 shows the results with and without the use of the proposed feature selection technique for all five datasets. The parameters were set to QT-D6 and a support threshold

Table 5.19: TCV classification results for QT-D5 data of Ep_{212}.

τ			SVM			C4.5		
%	F_{before}	F_{after}	Acc.	Sens.	Spec.	Acc.	Sens.	Spec.
20	10001	47	75.94	81.13	70.75	76.89	82.08	71.7
30	4681	39	**79.25**	**83.96**	**74.53**	**82.08**	**86.79**	**77.36**
40	2103	36	78.77	83.02	74.53	77.36	82.08	72.64
50	947	35	74.53	80.19	68.87	75.47	80.19	70.75
60	582	31	70.75	76.42	65.09	72.17	77.36	66.98
70	364	27	68.87	75.47	62.26	68.4	74.53	62.26
80	201	19	65.09	69.81	60.38	62.26	66.98	57.55
90	154	16	56.6	59.43	53.77	59.43	62.26	56.6

Table 5.20: TCV classification results for QT-D6 data of Ep_{212}.

τ			SVM			C4.5		
%	F_{before}	F_{after}	Acc.	Sens.	Spec.	Acc.	Sens.	Spec.
20	18440	42	81.60	84.91	78.30	82.08	86.79	77.36
30	10597	37	**83.02**	**85.85**	**80.19**	**86.32**	**87.74**	**84.91**
40	6933	28	78.77	83.02	74.53	80.19	84.91	75.47
50	4602	24	77.36	82.08	72.64	76.42	81.13	71.70
60	1341	18	69.81	75.47	64.15	73.11	78.30	67.92
70	923	16	67.45	72.64	62.26	67.45	72.64	62.26
80	602	14	64.62	69.81	59.43	65.09	69.81	60.38
90	298	15	64.62	69.81	59.43	62.26	66.98	57.55

Table 5.21: TCV classification results for QT-D7 data of Ep_{212}.

τ			SVM			C4.5		
%	F_{before}	F_{after}	Acc.	Sens.	Spec.	Acc.	Sens.	Spec.
20	39414	48	76.42	81.13	71.70	75.00	80.19	69.81
30	21342	42	**78.30**	**81.13**	**75.47**	77.36	82.08	72.64
40	12301	44	72.17	77.36	66.98	79.25	83.96	74.53
50	7240	39	70.28	76.42	64.15	**80.19**	**84.91**	**75.47**
60	5201	43	68.40	74.53	62.26	78.30	81.13	75.47
70	2201	27	64.15	68.87	59.43	70.28	76.42	64.15
80	1881	23	59.43	62.26	56.60	63.21	67.92	58.49
90	703	19	58.02	60.38	55.66	60.38	64.15	56.60

Table 5.22: The effect of feature selection for different datasets.

Datasets	F_b	F_a	Acc_b	Acc_a
Musician	9461	10	66.98	95.28
Handedness	8362	15	62.20	93.90
Ep_{106}	9841	33	58.49	84.91
Ep_{159}	10005	32	56.60	84.91
Ep_{212}	10597	37	59.43	86.32

of $\tau = 30\%$. F_a and F_b indicate the number of feature with and without the application of feature selection. Acc_a and Acc_b indicate the classification accuracy with and without the application of the feature selection. From the table it can clearly be seen that feature selection improves the classification performance.

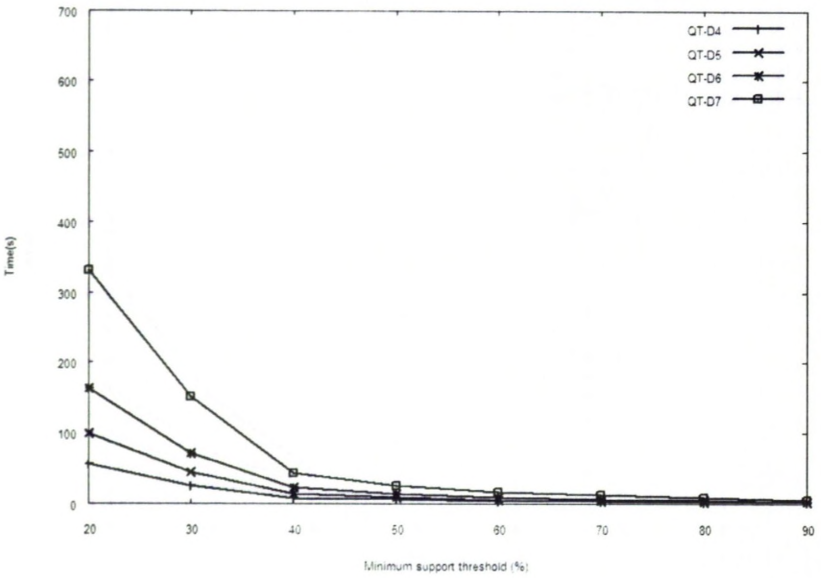

Figure 5.5: Run time complexity of image classification using musician dataset.

5.5.5 Time Complexity of the Proposed Graph Based Image Classification Approach

The computation time required by the graph based ROI image classification approach using the musician, handedness, and $Ep212$ datasets with different quad-tree levels (QT-D4, QT-D5, QT-D6, and QT-D7) are illustrated in Figures 5.5, 5.6, and 5.7 respectively. All the experiments were performed with 1.86 GHz Intel(R) Core(TM)2 PC with 2GB RAM. From the figures it can be observed that

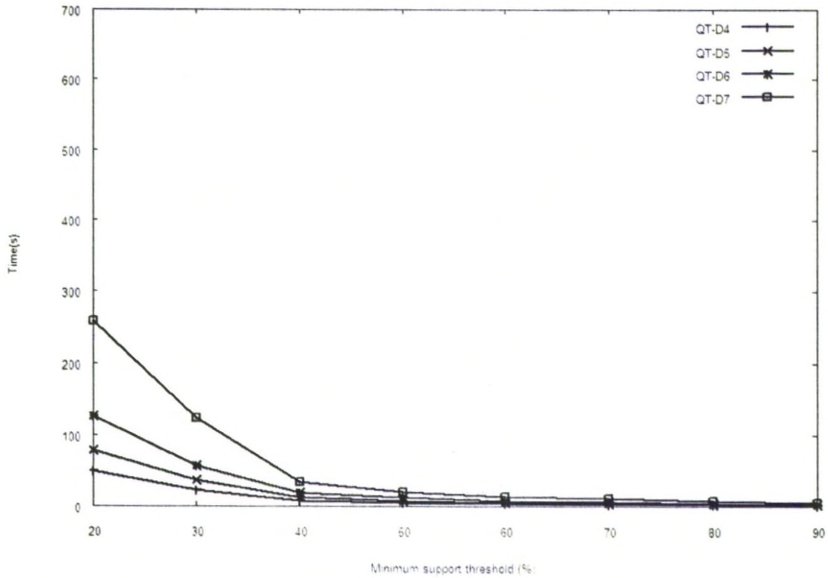

Figure 5.6: Run time complexity of image classification using handedness dataset.

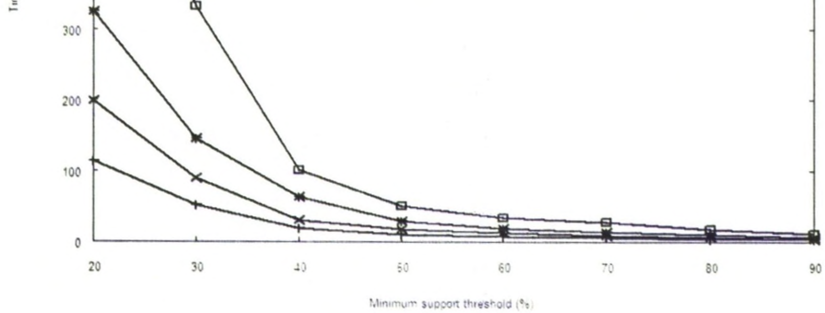

Figure 5.7: Run time complexity of image classification using *Ep*212 dataset.

the computation time increases as the quad-tree level increases because quad-trees with higher levels contain many more nodes and edges. Regardless of the quad-tree level used, the computational time also increases as the support threshold decreases. This is because the number of discovered frequent subgraphs increases as the support threshold decreases.

Experiments were also conducted using an unweighed FSM algorithm (gSpan), however the memory and runtime requirements were such that they were deemed to be unacceptable.

5.6 Discussion

The overall classification accuracies presented in Section 5.5 above indicate that the proposed graph based approach, using a tree representation to which weighted frequent subgraph mining was applied, performed well over different brain MRI datasets. However, The proposed graph based approach did not perform as well for the epilepsy study (but was still reasonable). As noted above the suspicion here is that the results reflect the fact that although the nature of the corpus callosum may play a part in the identification of epilepsy there are also other factors involved. Two parameter affect the overall classification accuracy: the depth of the quad-tree and the support threshold. The classification accuracy increases when the quad-tree level increases till a specific level is reached and then starts to fall of. This is because "overfitting" starts to take place as the quad-tree representation starts to get to be too detailed. Regardless the quad-tree level, the classification accuracy trend improved as the support threshold decreased. This was because more frequent subgraphs were identified as the support threshold decreased. It is likely that as the support threshold increases, significant subgraphs are overlooked by the graph mining algorithm.

5.7 Summary

In this chapter a new ROIBIC approach has been described. The technique was directed at classifying Magnetic Resonance Image (MRI) brain scans according to the nature of a ROI (the corpus callosum with respect to the focus application considered in this thesis). The approach used a hierarchical decomposition whereby each MRI scan was decomposed into a hierarchy of "tiles" which could then be represented as a quad-tree structure (one quad-tree per scan). A weighted frequent subgraph mining mechanism was then applied so that subgraphs that occurred frequently across the image set could be identified. These frequent subgraphs could be viewed as describing a feature space; as such the input images could be translated, according to this feature space, into a set of feature vectors (one per image). A feature selection mechanism was applied to the feature vectors so as to select the most significant features to which standard classification techniques could be applied. The reported evaluation indicates that high classification accuracy results were obtained when using higher quad-tree levels of decomposition, coupled with low support threshold, although if the level of decomposition gets too high "over fitting" starts to take place. In the following chapter an alternative approach for classifying images according to a common image feature, founded on Zernike moments, is described.

Chapter 6

Region Of Interest Image Classification Using a Zernike Moment Signature Representation

6.1 Introduction

Moments are scalar quantities used to characterize a function and to capture its significant features. They have been widely used for hundreds of years in statistics for the description of the shape of probability density functions and in classic "rigid-body" mechanics to measure the mass distribution of a body. From the mathematical point of view, moments are "projections" of a function onto a polynomial basis. The general moment G_{pq} of an image function $f(x, y)$, where p, q are non-negative integers and $r = p + q$ is called the order of the moment, defined as:

$$G_{pq} = \iint_{D} P_{pq}(x, y)\, f(x, y)\, dx\, dy, \tag{6.1}$$

where $P_{00}(x, y), P_{10}(x, y), ..., P_{kj}(x, y), ...$ are polynomial basis functions defined on D. Depending on the polynomial basis used, various systems of moments may be defined. The most common is a standard power basis $P_{kj}(x, y) = x^k y^j$ that leads to geometric moments, M_{pq}:

$$M_{pq} = \int_{-\infty}^{\infty} \int_{-\infty}^{\infty} x^p y^q f(x, y)\, dx\, dy. \tag{6.2}$$

Geometric moments of low orders have an intuitive meaning - M_{00} is a "mass" of the image (for binary images, M_{00} is an area of the object), M_{10}/M_{00} and M_{01}/M_{00}

define the centroid of the image. Another popular choice of the polynomial basis $P_{kj}(x,y) = (x+iy)^k(x-iy)^j$, where $i = \sqrt{-1}$, leads to complex moments, C_{pq}:

$$C_{pq} = \int_{-\infty}^{\infty}\int_{-\infty}^{\infty} (x+iy)^p\,(x-iy)^q\, f(x,y)\,dx\,dy. \tag{6.3}$$

If the polynomial basis $\{P_{kj}(x,y)\}$ is orthogonal, i.e. if its elements satisfy the condition of orthogonality for any indexes $p \neq m$ or $q \neq n$ then:

$$\iint_D P_{pq}(x,y).P_{mn}(x,y)\,dx\,dy \;=\; 0 \tag{6.4}$$

The advantage of orthogonal moments is their ability to capture the image features in an improved, nonredundant way. Zernike moments are a class of *orthogonal moments* (moments produced using orthogonal basis sets) that can be used as an effective image descriptor. Zernike moments were first introduced by Teague [141]. Teh and Chin [142] evaluated various image moments in terms of their image description capabilities and noise sensitivity, The evaluation included: (i) geometric, (ii) Legendre, (iii) Zernike, (iv) pseudo-Zernike, (v) rotational, and (vi) complex moments. They showed that Zernike moments outperformed the other moments. Unfortunately, direct computation of Zernike moments from the Zernike polynomial is computationally expensive. This makes it impractical for many applications. This limitation has prompted considerable study of algorithms for fast evaluation of Zernike moments [15, 86, 105, 119]. Several algorithms have been proposed to speed up the computation. Belkasim et al. [15] introduced a fast algorithm based on the series expansion of radial polynomials. Parta et al. [119] and Kintner [86] have proposed recurrence relations for fast computation of radial polynomials of Zernike moments. However, these techniques are not applicable in many cases for the computation of Zernike moments where $((p = q)\, and\, (q = 0))$, and $(p - q < 4)$ respectively. Chong et al. [23] modified Kintners method so that it would be applicable for all cases. Unfortunately, all of these methods approximated Zernike moment polynomials and consequently, produced inaccurate sets of Zernike moments. On the other hand, Wee et al. [150], proposed a new algorithm that computed exact Zernike moments through a set of exact geometric moments. Their method is accurate, but it is time consuming. In this chapter, we introduce a new method for exact Zernike Moment computation based on the observation that exact Zernike moments can be expressed as a function of geometric moments. Wu et al. [152] describe a fast algorithm that accelerates the computation of geometric moments. The algorithm is based on a quad-tree representation of images (similar to that described in Chapter 5) whereby a given pixel represented region is decomposed into a number of non-overlapping tiles. Since the geometric moment computation for each tile is easier than that for the whole region, the algorithm proposed by Wu reduces the computational complexity significantly.

In this chapter a mechanism for fast Zernike moment calculation, based on the work of Wu [152], is proposed. The resulting Zernike moments are used to define a feature vector (one per image) which can be input to a standard classification mechanism (a SVM and C4.5 were used for evaluation). The rest of this chapter is organized as follows. In Section 6.2 a review of Zernike moments is presented in terms of their general application to image analysis. In Section 6.3 the calculation of Zernike moments in terms of geometric moments is presented. Section 6.4 then presents a mechanism, first proposed in [152], for the fast calculation of geometric moments using the quad-tree decomposition. The proposed mechanism for the fast calculation of Zernike moments is presented in Section 6.5. In Section 6.6 feature extraction based on Zernike moments, to support ROI based image classification, is introduced. The evaluation of the proposed approach is presented in Section 6.7. Finally, Some discussion and summary is then presented in Section 6.8.

6.2 Zernike Moments

The complex 2D Zernike moments of order p and repetition q of an image intensity function $f(r,\theta)$ are defined as:

$$Z_{pq} = \frac{p+1}{\pi} \int_0^{2\pi} \int_0^1 \left[V_{pq}(r,\theta) \right]^* f(r,\theta)\, r\, dr\, d\theta \tag{6.5}$$

where $p = 0, 1, 2, ..., \infty$ and q is an integer such that $p - |q| = even, |q| \leq p$. $*$ is the complex conjugate. The p-th order Zernike polynomials with repetition q are defined as:

$$V_{pq}(r,\theta) = R_{pq}(r) e^{iq\theta} \tag{6.6}$$

where $r = \sqrt{x^2+y^2}$, $r \in [-1,1]$ is the length of the vector from the image pixel (x,y) to the origin, $\theta = arctan(y/x)$ is the angle between vector r and the principle x-axis and $i = \sqrt{-1}$. These Zernike polynomials describe a complete set of complex-valued orthogonal functions defined on the unit circle, $x^2+y^2 \leq 1$. The real-valued radial polynomials $R_{pq}(r)$ are defined as:

$$R_{pq}(r) = \sum_{\substack{k=q \\ p-k=even}}^{p} B_{p|q|k} r^k \tag{6.7}$$

where the polynomial coefficients, $B_{p|q|k}$, are defined as:

$$B_{p|q|k} = \frac{(-1)^{\left(\frac{p-k}{2}\right)} \left(\frac{p+k}{2}\right)!}{\left(\frac{p-k}{2}\right)! \left(\frac{k+q}{2}\right)! \left(\frac{k-q}{2}\right)!} \tag{6.8}$$

The Zernike polynomial coefficients can be computed using the recurrent relations proposed in [105] as follows:

$$\begin{aligned}
B_{ppp} &= 1 \\
B_{p(q-2)p} &= \frac{p+q}{p-q+2} B_{pqp} \\
B_{pq(k-2)} &= -\frac{(k+q)(k-q)}{(p+k)(p-k+2)} B_{pqk}
\end{aligned} \tag{6.9}$$

Zernike polynomials satisfy the orthogonality relationship:

$$\int_0^{2\pi}\int_0^1 V_{nm}(r,\theta) V_{pq}(r,\theta)\, r\, dr\, d\theta = \begin{cases} \frac{\pi}{p+1}, & p = n, q = m \\ 0, & \text{otherwise} \end{cases} \tag{6.10}$$

Zernike moments are by nature rotation invariant, therefore the magnitudes of Zernike moments are unaffected and remain constant with respect to an image function regardless of any rotation. If an image function $f(r,\theta)$ with a Zernike moment Z_{pq} is rotated counter-clockwise by angle α, the transformed image function is $g(r,\theta) = f(r, \theta - \alpha)$. The Zernike moment of the rotated image is given by:

$$Z_{pq}^{\alpha} = e^{-iq\alpha} Z_{pq}. \tag{6.11}$$

This leads to the well-known rotational invariance property $\left|Z_{pq}^{\alpha}\right| = |Z_{pq}|$.

In the case of digital images the calculation becomes discrete because we are working at the pixel level. Therefore to compute Zernike moments of a digital (discrete) image intensity function of size $N \times N$, the integrals are replaced by summations to obtain:

$$Z_{pq} = \frac{p+1}{\pi} \sum_{i=0}^{N-1} \sum_{j=0}^{N-1} V_{pq}^{*} f(x,y), \quad x_i^2 + y_j^2 \leq 1 \tag{6.12}$$

Consequently, the latter generates approximation Zernike moments which in turn gives rise numerical errors.

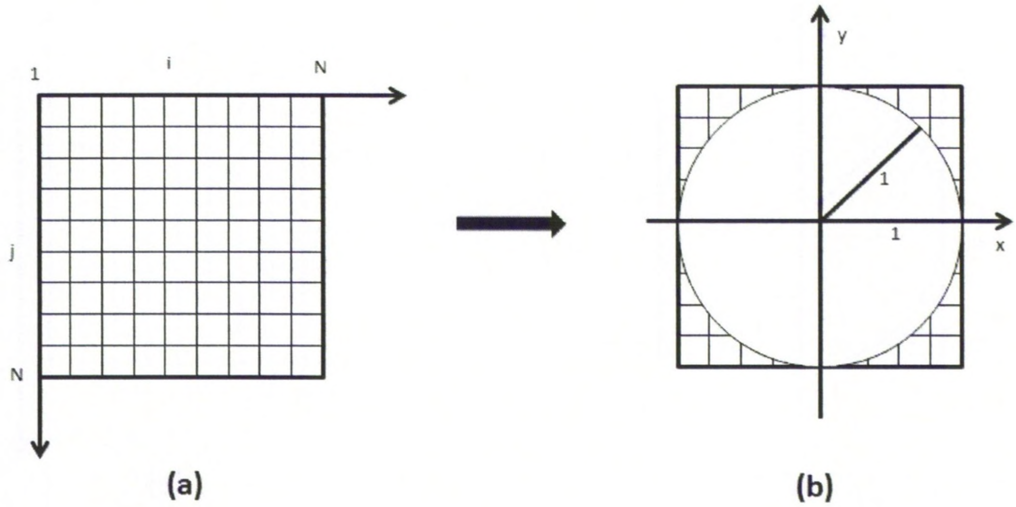

Figure 6.1: (a) Digital image, (b) Mapping the digital image onto the unit circle.

Zernike polynomials can thus be defined in terms of polar coordinates (r, θ) over a unit circle, while the image intensity function is typically defined in terms of Cartesian coordinates (x, y), therefore, the computation of Zernike moments requires an image transformation. There are two traditional mapping approaches [23]. In the first approach, the square image plan (Figure 6.1(a)) is mapped onto a unit circle, where the centre of the image is assumed to be the origin of the coordinate system (Figure 6.1(b)). In this approach, all pixels outside the unit circle are ignored, which results in a loss of some image information as shown in Figure 6.1. In the second approach, the whole square image plan is mapped inside a unit circle such that the centre of the image is assumed to be the coordinate origin. In the work described here, the second approach is used to avoid loss of information as illustrated in Figure 6.2. Then the transformed image of size $N \times N$ is defined in the square $[-1/\sqrt{2}, 1/\sqrt{2}] \times [-1/\sqrt{2}, 1/\sqrt{2}]$, and the transformed image coordinates are defined as:

$$x_i = \frac{2i - N - 1}{N\sqrt{2}}, \quad y_j = \frac{2j - N - 1}{N\sqrt{2}} \tag{6.13}$$

with $i = 1, 2, ..., N$ and $j = 1, 2, ..., N$.

The transformed sampling intervals are:

$$\Delta x_i = \sqrt{2}/N, \ \Delta y_j = \sqrt{2}/N \tag{6.14}$$

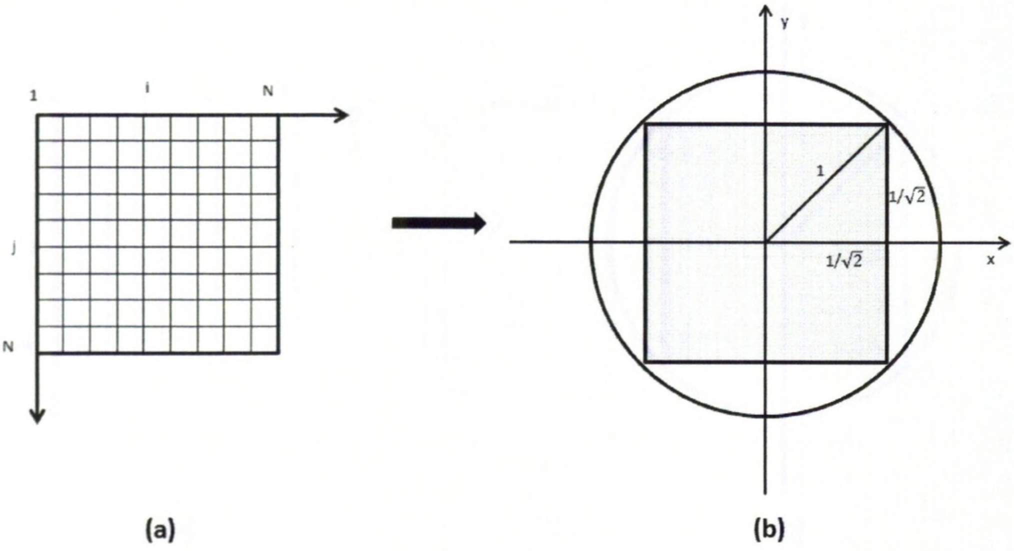

Figure 6.2: (a) Digital image, (b) Mapping the digital image into the unit circle.

6.3 Calculation of Zernike moments in terms of Geometric Moments

Zernike moments can be expressed in terms of geometric moments [142] using the following relationship:

$$Z_{pq} = \frac{p+1}{\pi} \sum_{\substack{k=|q| \\ p-k=even}}^{p} \sum_{n=0}^{s} \sum_{m=0}^{|q|} (-w)^m \binom{s}{n} \binom{|q|}{m} B_{p|q|k} M_{k-2n-m,2n+m} \tag{6.15}$$

where $s = (k - |q|)/2, w = \sqrt{-1}$, and M is a geometric moment computed inside the unit circle.

Geometric moments M_{pq} with the order $(p+q)$ of a two dimensional function $f(x, y)$ are defined as:

$$M_{pq} = \int_{-\infty}^{\infty} \int_{-\infty}^{\infty} f(x, y)\, x^p\, y^q\, dx\, dy \tag{6.16}$$

In a digital domain, the approximated moments M_{pq} of a digital $f(x, y)$ with a resolution of $N \times N$ is given by:

$$M_{pq} = \sum_{x=1}^{N} \sum_{y=1}^{N} f(x, y)\, x^p\, y^q \tag{6.17}$$

The substitution of double integrals by double summations introduces a numerical error. Consequently, computing Zernike moments using approximated geometric moments yields an approximation of Zernike moments. Exact Zernike moments can be computed by using exact geometric moments [150]. For exact geometric moments GM_{pq}, Equation (6.17) is written as

$$GM_{pq} = \sum_{i=1}^{N} \sum_{j=1}^{N} f(x_i, y_j)\, h_{p,i}\, g_{q,j} \tag{6.18}$$

where $h_{p,i}$ and $g_{q,j}$ can be expressed by using the normal mathematical integration rule:

$$\begin{aligned} h_{p,i} &= \int\limits_{x_i-\Delta x_i/2}^{x_i+\Delta x_i/2} x^p dx = \left[\frac{x^{p+1}}{p+1} \right]_{x_i-\Delta x_i/2}^{x_i+\Delta x_i/2} \\ g_{q,j} &= \int\limits_{y_j-\Delta y_j/2}^{y_j+\Delta y_j/2} y^q dy = \left[\frac{y^{q+1}}{q+1} \right]_{y_j-\Delta y_j/2}^{y_j+\Delta y_j/2} \end{aligned} \tag{6.19}$$

Using the image transformation into a unit circle approach (as demonstrated in Figure 6.2). (6.19) can be rewritten as:

$$h_{p,i} = \left[\frac{U_{i+1}^{p+1} - U_i^{p+1}}{p+1} \right]$$

$$g_{q,j} = \left[\frac{U_{j+1}^{q+1} - U_j^{q+1}}{q+1} \right] \tag{6.20}$$

with

$$U_{i+1} = \frac{2i - N}{N\sqrt{2}}$$

$$U_i = \frac{2(i-1) - N}{N\sqrt{2}} \tag{6.21}$$

Then the numerical error introduced by replacing the double integrals with double summations can be eliminated by calculating exact Zernike moments in terms of exact geometric moments. Thus:

$$Z_{pq} = \frac{p+1}{\pi} \sum_{\substack{k=|q| \\ p-k=even}}^{p} \sum_{n=0}^{s} \sum_{m=0}^{|q|} (-w)^m \binom{s}{n} \binom{|q|}{m} B_{p|q|k} GM_{k-2n-m,2n+m} \tag{6.22}$$

Therefore the above mechanism was adopted for use with the ROIBIC method suggested in this chapter. On the other hand, computation of exact geometric moments as described above is time consuming. Therefore, in the next section, a method to speed up this computation is described.

6.4 Fast Calculation of Geometric Moments

To speed up the calculation of Zernike moments in terms of geometric moments as described in the foregoing, we use a quad-tree decomposition similar to that used in the graph based approach described in Chapter 5. Wu et al. [152] also proposed using the quad-tree decomposition as the first stage of their geometric moment computation method. The decomposition operates using square images, ideally with a size of power of two. The image is iteratively divided into four quadrants (tiles). The homogeneity of each quadrants is checked and if the whole quadrants lies either in the region or in the background, it is not further divided. If it contains both region and background pixels it is divided into further quadrants and the process is repeated until all tiles are homogeneous.

After the decomposition, the ROI will be represented by a quad-tree of k non-overlapping square tiles $B_1, B_2, ..., B_k$. Then the computational complexity of the geometric moments can be decreased by computing the geometric moments of these k tiles. For each tile B_i, the coordinate indices of its upper left corner are (a, b) and the length of tile side is w. The geometric moments $GM_{pq,i}$ for the block B_i can then be calculated using equations 6.18, 6.19 and 6.20, as:

$$\begin{aligned} GM_{pq,i} &= \int\limits_{x_a-\frac{\Delta x}{2}}^{x_{a+w-1}+\frac{\Delta x}{2}} x^p dx \int\limits_{y_b-\frac{\Delta y}{2}}^{y_{b+w-1}+\frac{\Delta y}{2}} y^q dy \\ &= \left[\frac{U_2^{p+1} - U_1^{p+1}}{p+1}\right] \left[\frac{U_4^{q+1} - U_3^{q+1}}{q+1}\right] \end{aligned} \tag{6.23}$$

with:

$$\begin{aligned} U_1 &= \frac{2(a-1) - N}{N\sqrt{2}} \\ U_2 &= \frac{2(a+w-2) - N}{N\sqrt{2}} \\ U_3 &= \frac{2(b-1) - N}{N\sqrt{2}} \\ U_4 &= \frac{2(b+w-2) - N}{N\sqrt{2}} \end{aligned} \tag{6.24}$$

Then, the geometric moment of the ROI can be easily calculated by summing the geometric moments of all k tiles in the decomposition that are part of the ROI, since the computation of geometric moments of tiles is easier than that for the whole ROI where $k < N^2$. Then, the geometric moment for the entire ROI can be calculated as follows:

$$GM_{pq} = \sum_{n=1}^{k} GM_{pq,n} \tag{6.25}$$

In the work described here the decomposition is conducted down to the pixel level (unlike in the case of the quad-tree decomposition described in Chapter 5). Also the homogeneity condition, unlike previously, is 100% black or white. This is to ensure that exact geometric moments are derived. Note that if the image is entirely decomposed down to the pixel level (e.g. if we have a "checker board" image) then the method will be similar to the Wee method [150].

6.5 Fast Calculation of Zernike Moments

The proposed mechanism for the fast calculation of Zernike moments adopts the idea of representing the exact Zernike moments in terms of exact geometric moments calculated using a quad-tree decomposition of the form described above. This decomposition is used to speed up the computation of geometric moments as also described above. The procedure for computing a full set of Zernike moments is as follows (here Max is the maximum order of moments to be calculated):

1. Transform the image (or a ROI) into a unit circle so that the transformed image of size $N \times N$ is defined in the square $[-1/\sqrt{2}, 1/\sqrt{2}] \times [-1/\sqrt{2}, 1/\sqrt{2}]$.

2. Decompose the image into k square tiles, $B_1, B_2, ..., B_k$, using a quad-tree decomposition as described in Section 6.4.

3. For p=0 to Max
   Compute the Zernike polynomial coefficients B as in Eq. (6.9).

4. For p=0 to Max & q=0 to Max
   Compute GM_{pq} using Eq. (6.23), (6.24), (6.25)

5. For p=0 to Max & For q=0 to p
   Compute Z_{pq} using Eq. (6.22).

The Zernike moment magnitudes thus calculated is then used to define a feature space for each image (or ROI).

6.6 Feature Extraction Based on Zernike Moments

In the context of the proposed ROIBIC approach, the Zernike moment magnitudes are used to define a feature space representing the image set. Each image, or more specifically the object of interest within each image, can then be represented in terms of a feature vector. The feature vector $\{AFV\}_N$ will then consist of the accumulated Zernike moment magnitudes from order $p = 0$ to order $p = N$ with all possible repetitions q. For example, where $N = 4$, the feature vector $\{AFV\}_4$ will consist of the set of all Zernike moments corresponding to the orders $p = 0, 1, 2, 3, 4$ coupled with all possible repetitions q: $\{|Z_{00}|, |Z_{11}|, |Z_{20}|, |Z_{22}|, |Z_{31}|, |Z_{33}|, |Z_{40}|\ , |Z_{42}|, |Z_{44}|\}$.

Consequently a set of images that contain a common ROI (such as the corpus callosum in the case of the brain MRI scan data of interest with respect to this thesis) can be represented as a set of feature vectors which can be input to standard classification techniques.

6.7 Evaluation

This evaluation section is divided into four subsections: (i) experimental studies on the validity of the proposed method of Zernike moments computation, (ii) speed of the calculation of Zernike moments according to the proposed approach, (iii) the evaluation of using Zernike moments in the context of image classification, and (iv) run time analysis of the proposed classification technique.

6.7.1 Experimental Studies on the Validity of the Proposed Method of Zernike Moments Computation

An artificial image were used to demonstrate the validity of the proposed method. The artificial image used was a 4×4 pixel image in which all pixel intensity values were one, $f(x, y) = 1$ for all pixels (x, y). The image defined in the square $[-1, 1] \times [-1, 1]$ was mapped to be inside the unit circle where the coordinate origin was the center of the circle. The mapped image was defined in the square $[-1/\sqrt{2}, 1/\sqrt{2}] \times [-1/\sqrt{2}, 1/\sqrt{2}]$. The theoretical values of the exact Zernike moments, Z_{pq}^{Theo}, were then computed using:

$$Z_{pq}^{Theo} = \frac{p+1}{\pi} \sum_{\substack{k=q \\ p-k=even}}^{p} B_{pqk} \sum_{n=0}^{s} \binom{s}{n} \sum_{m=0}^{|q|} (-w)^m \binom{q}{m} \int_{\frac{-1}{\sqrt{2}}}^{\frac{1}{\sqrt{2}}} x^{(k-2n+m)}\, dx \int_{\frac{-1}{\sqrt{2}}}^{\frac{1}{\sqrt{2}}} y^{(2n+m)}\, dy \tag{6.26}$$

where $s = (k - q)/2$ and $w = \sqrt{-1}$. The approximated Zernike moments Z_{pq}^{approx} were calculated using Equations (6.15),(6.17) while the proposed exact Zernike

Table 6.1: Comparison of theoretical Z_{pq}^{Theo}, proposed Z_{pq}^{prop}, and approximated Z_{pq}^{approx} for $f(x_i, y_j) = 1$.

p	q	Z_{pq}^{Theo}	Z_{pq}^{prop}	Z_{pq}^{approx}
0	0	0.6366	0.6366	0.6366
2	0	-0.6366	-0.6366	-0.7162
2	2	0	0	0
4	0	-0.2122	-0.2122	-0.3233
4	2	0	0	0
4	4	-0.2122	-0.2122	-0.2455
6	0	0.2122	0.2122	0.3525
6	2	0	0	0
6	4	0.2122	0.2122	0.4026
6	6	0	0	0
8	0	0.1273	0.1273	0.3642
8	2	0	0	0
8	4	0.1273	0.1273	0.1850
8	6	0	0	0
8	8	0.1273	0.1273	0.1204
10	0	-0.1273	-0.1273	-0.1669
10	2	0	0	0
10	4	-0.1273	-0.1273	-0.1765
10	6	0	0	0
10	8	-0.1273	-0.1273	-0.2019
10	10	0	0	0

moments values Z_{pq}^{prop} were calculated using Equations (6.22 - 6.20). Table 6.1 indicates that the theoretical Zernike moment values and exact Zernike moment values generated by the proposed method are identical, while these values did not match with the approximated Zernike moment values.

6.7.2 Speed of Calculation of Zernike Moments According to the Proposed Approach

The speed of the proposed method of computation was compared with the Wee method [150]. All the experiments were performed with 1.86 GHz Intel(R) Core(TM)2 PC with 2GB RAM. The code was designed using Matlab 7. The full set of Zernike moments was computed using both Wee's [150] and the proposed methods. A 128 × 128 pixel binary image, as in Figure 6.3, was used. The recorded CPU elapsed times are presented in Figure 6.4. From the figure it is clear that the proposed method significantly reduced the execution time.

Figure 6.3: 128 × 128 Artificial binary test image.

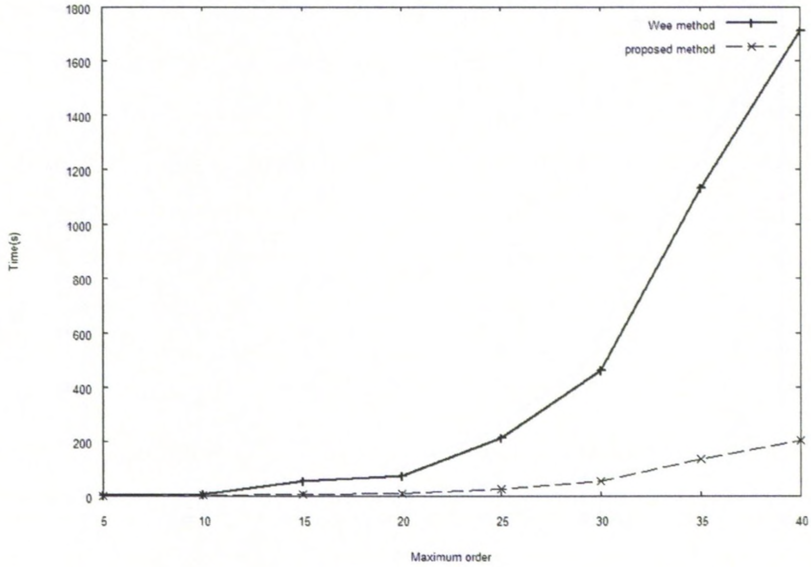

Figure 6.4: CPU elapsed time(s) of the 128 × 128 binary test image for Wee [150] and the proposed method.

6.7.3 Classification Performance

The evaluation of the proposed Zernike moment based image classification approach, with respect to the corpus callosum application, is presented in this section. This section describes the evaluation of the proposed technique using an appropriate MRI image set. Two classification techniques were used for the evaluation: (i) Decision Trees (i.e. C4.5) [122] and (ii) Support Vector Machines (SVMs) [28], to examine the performance of Zernike moments with respect to ROI image classification. For the C4.5 classifier, the WEKA implementation [60] was used, and for the SVM classifier, the LIBSVM implementation [22] was used. In the experiments, all the classification results were computed using TCV. The three studies used previously to evaluate proposed ROIBIC approaches were again used: (i) a comparison between musician and non-musician MRI scans, (ii) a comparison between left handedness and right handedness, and (iii) an epilepsy screening process. (The description of the datasets was presented in Chapter 3.)

Table 6.2 shows the TCV results obtained using the musician dataset. The SVM and C4.5 columns indicate the results using the SVM and C4.5 classification techniques respectively. Acc, Sens and Spec refer to accuracy, sensitivity and specificity respectively. The N indicates the maximum order of Zernike moments to be generated which will then influence the size of the feature vectors ($\{AFV\}_N$) used to represent individual images.

Table 6.2 indicates that the best classification accuracy achieved using the SVM was 96.23% when the maximum order of Zernike moments used was equal to 10, while the best classification accuracy achieved by C4.5 was 94.34% when maximum order of Zernike moments was equal to 9. The best sensitivity and specificity were 98.11% and 94.34% (SVM) and 96.15% and 92.59% (C4.5) respectively. The trend of the classification accuracies increased as the maximum order N increased, as can be seen in Table 6.2. It is conjectured that this is because higher orders of Zernike moments give a more detailed description of the ROI.

For the handedness study, Table 6.3 indicates that the best classification accuracies achieved were 93.90% (SVM) and 90.24% (C4.5). These best classification accuracies was obtained using a maximum order of $N = 9$. High sensitivity and specificity were also achieved and were associated with the corresponding best

Table 6.2: TCV classification results for musicians study.

N	SVM			C4.5		
	Acc.	Sens.	Spec.	Acc.	Sens.	Spec.
2	57.55	60.38	54.72	57.55	60.38	54.72
3	68.87	75.47	62.26	59.43	58.49	60.38
4	76.42	79.25	73.58	64.15	66.04	62.26
5	84.91	86.79	83.02	69.81	71.70	67.92
6	87.74	88.68	86.79	83.02	84.91	81.13
7	90.57	92.45	88.68	87.74	88.68	86.79
8	94.34	96.23	92.45	87.74	88.68	86.79
9	95.28	94.34	96.23	**94.34**	**96.15**	**92.59**
10	**96.23**	**98.11**	**94.34**	89.62	90.57	88.68

Table 6.3: TCV classification results for handedness study.

N	SVM			C4.5		
	Acc.	Sens.	Spec.	Acc.	Sens.	Spec.
2	54.88	62.50	47.62	57.32	62.50	52.38
3	62.20	67.50	57.14	60.98	67.50	54.76
4	69.51	75.00	64.29	62.20	67.50	57.14
5	75.61	82.50	69.05	73.17	82.50	64.29
6	79.27	82.50	76.19	80.49	87.50	73.81
7	87.80	92.50	83.33	85.37	92.50	78.57
8	90.24	95.00	85.71	84.15	90.00	78.57
9	**93.90**	**95.00**	**92.86**	**90.24**	**92.50**	**88.10**
10	91.46	92.50	90.48	89.02	95.00	83.33

accuracies obtained.

Tables 6.4 to 6.6 show the classification performance using the epilepsy datasets. Inspection of these tables, indicates that the best classification accuracy obtained using the SVM were 83.02%, 84.91% and 85.38% for the three epilepsy datasets Ep_{106}, Ep_{159}, Ep_{212} respectively. The first two best accuracies were obtained using $N = 10$, while the third was obtained using $N = 9$.

From the tables, it can again be observed that the classification accuracy increases as the maximum Zernike moment order N increases. Again, it is suggested that higher Zernike moment orders hold more detail about the ROI. The overall classification accuracy results obtained using the epilepsy datasets was less than those obtained using the musician and handedness datasets. As noted previously, the suspicion here is that the results reflect the fact that although the nature of the corpus callosum may play a part in the identification of epilepsy there are

Table 6.4: TCV classification results for Ep_{106}.

N	SVM			C4.5		
	Acc.	Sens.	Spec.	Acc.	Sens.	Spec.
2	57.55	60.38	54.72	56.6	62.26	50.94
3	59.43	58.49	60.38	58.49	62.26	54.72
4	67.92	69.81	66.04	61.32	62.26	60.38
5	68.87	75.47	62.26	66.04	69.81	62.26
6	73.58	71.7	75.47	70.75	71.7	69.81
7	79.25	81.13	77.36	76.42	79.25	73.58
8	79.25	81.13	77.36	78.3	81.13	75.47
9	82.08	84.91	79.25	79.25	81.13	77.36
10	**83.02**	**84.91**	**81.13**	**80.19**	**83.02**	**77.36**

Table 6.5: TCV classification results for Ep_{159}.

N	SVM			C4.5		
	Acc.	Sens.	Spec.	Acc.	Sens.	Spec.
2	51.57	50.94	51.89	51.57	50.94	51.89
3	52.83	52.83	52.83	52.83	52.83	52.83
4	66.67	67.92	66.04	64.78	66.04	64.15
5	71.70	73.58	70.75	72.33	73.58	71.70
6	77.36	81.13	75.47	75.47	77.36	74.53
7	80.50	86.79	77.36	76.10	79.25	74.53
8	83.65	90.57	80.19	78.62	83.02	76.42
9	82.39	88.68	79.25	**81.76**	**88.68**	**78.30**
10	**84.91**	**92.45**	**81.13**	79.25	84.91	76.42

Table 6.6: TCV classification results for Ep_{212}.

N	SVM			C4.5		
	Acc.	Sens.	Spec.	Acc.	Sens.	Spec.
2	60.85	64.15	57.55	54.25	55.66	52.83
3	66.98	70.75	63.21	55.19	56.6	53.77
4	68.4	74.53	62.26	61.32	65.09	57.55
5	76.42	81.13	71.7	63.21	67.92	58.49
6	80.66	85.85	75.47	68.87	75.47	62.26
7	84.43	86.79	82.08	74.06	78.3	69.81
8	84.43	86.79	82.08	80.19	84.91	75.47
9	**85.38**	**87.74**	**83.02**	**81.6**	**86.79**	**76.42**
10	84.43	86.79	82.08	80.19	84.91	75.47

also other factors involved.

6.7.4 Time Complexity of the Proposed Classification Approach Based on Zernike Moments

The computation time of the ROI image classification approach based on Zernike moments, using the three datasets (musician, handedness and Ep_{212}), is presented in Figure 6.5. All the experiments were performed with 1.86 GHz Intel(R) Core(TM)2 PC with 2GB RAM. The code was designed using Matlab 7. Note that the run time complexity increases as the maximum Zernike moments order increases, this is to be expected as higher values of N necessitate more processing.

6.8 Discussion and Summary

In this chapter a new fast method for computing Zernike moments, based on a quad-tree decomposition, has been described. A full set of Zernike moments was used in the context of MR image classification. The use of Zernike moments is a popular technique in image processing and analysis; this is the reason why the use of Zernike moments was included in the research described in this thesis. The reported evaluation indicated that the proposed technique gave reasonable classification results. The overall performance classification accuracies presented in Section 6.7 above indicate that:

1. The proposed approach, based on the Zernike moments gives a higher accuracy using high orders of Zernike moments than when using lower orders.

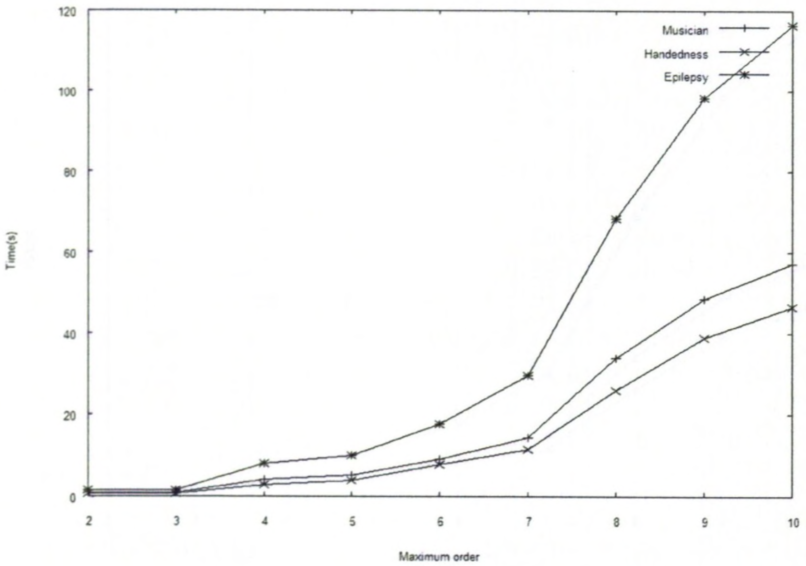

Figure 6.5: Run time complexity of image classification using different MRI datasets.

2. The classification accuracy of musician and handedness studies is relatively higher than that recorded for the epilepsy study.
3. Using the proposed computation method of exact Zernike moments reduces the computational time required for the overall classification process.

In the following chapter an alternative approach for classifying images according to a common image feature, founded on the representation of ROI as a time series, is described.

Chapter 7

Region Of Interest Image Classification Using a Time Series Representation

7.1 Introduction

In this chapter, a new approach to ROIBIC, founded on a time series representation coupled with a Case Based Reasoning (CBR) mechanism, is introduced. In this approach the features of interest are represented as time series, one per image. Two techniques for generating the desired time series are considered: (i) ROI intersection (ROI Int.) time series generation and (ii) radial distance (Rad. Dist.) time series generation. These time series are then stored in a Case Base (CB) which can be used to categorise unseen data using a Case Based Reasoning (CBR) approach. The unseen data is compared with the categorisations in the CB using a Dynamic Time Warping (DTW) similarity checking mechanism. The class associated with the most similar time series (case) in the CB is then adopted as the class for the unseen data. Note that the phrase "time series" is used with respect to the adopted representation because the proposed image classification technique is founded on work on time series analysis, not because the representation includes some temporal dimension.

The rest of this chapter is organized as follows. Section 7.2 describes the two techniques for generating the desired ROI time series *signature* based on the shape of the ROI. In Section 7.3 the DTW similarity measure used to compare ROI signatures is presented. The framework for the proposed ROIBIC approach is presented in Section 7.4, and the evaluation of the proposed approach in Section

7.5. The chapter is then concluded with a summary in Section 7.6.

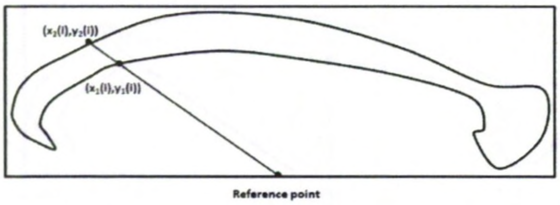

Figure 7.1: ROI signature using the ROI Int. method.

7.2 Proposed Image Signature Based on Pseudo Time Series

A shape signature is a 1D function that can be used to represent a 2D ROI, the intention is to capture the nature of the shape. With respect to the approach proposed in this chapter such signatures are defined in terms of a "pseudo" time series. Two mechanisms for generating the desired time series are considered: (i) ROI intersection time series generation (ROI Int.) and (ii) radial distance (Rad. Dist.) time series generation. Each is discussed in further detail in the following two subsections.

7.2.1 ROI Intersection Time Series Generation (ROI Int.)

Using the ROI intersection mechanism the desired image signature ("pseudo" time series) is generated using an ordered sequence of M "spokes" radiating out from a single reference point. The desired time series is then expressed as a series of values (one for each spoke) describing the size (length) of the intersection of the vector with the ROI. The representation thus maintains the structural information (shape and size) of the ROI. It should also be noted that the value of M may vary due to the differences of the shape and size of the individual ROI within the image data set.

Formally speaking, assume that there are M spokes and each spoke i, radiating out from some reference point, intersects the ROI boundary at two points $(x_1(i), y_1(i))$ and $(x_2(i), y_2(i))$; then the proposed image signature is given by [44]:

$$D(i) = \sqrt{\left((x_1(i) - x_2(i))^2 + (y_1(i) - y_2(i))^2\right)}, \quad i = 1, 2, ..., M \tag{7.1}$$

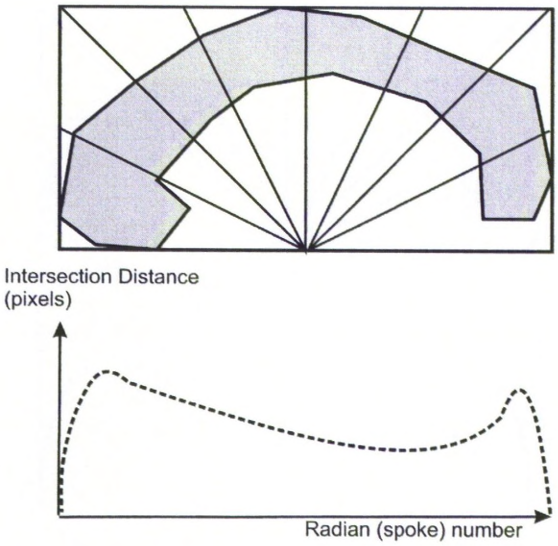

Figure 7.2: Conversion of corpus callosum into time series using the ROI Int. method.

With respect to the corpus callosum application the time series generation procedure is illustrated in Figure 7.1. The midpoint of the lower edge of the object's Minimum Bounding Rectangle (MBR) was selected as the reference point. This was chosen as this would ensure that there was only two boundary intersections per spoke. The vectors were derived by rotating an arc about the reference point pixel. The interval between spokes was one pixel measured along the edge of the MBR. For each spoke the intersection distance D_i (where i is the spoke identification number) over which the spoke intersects with a sequence of corpus callosum pixels was measured and recorded. The result is a time series with the spoke number i representing time and the value D_i, for each spoke, the magnitude (intersection length). By plotting D_i against i a pseudo time series can be derived as shown in Figure 7.2.

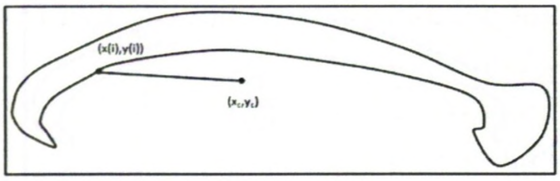

Figure 7.3: ROI signature using the Rad. Dist. method

7.2.2 Radial Distance Time Series Generation (Rad. Dist.)

An alternative approach to that described in the foregoing sub-section is the radial distance time series generation mechanism. This is founded on a well established technique used in shape description. Using this mechanism the desired time series is generated by sequentially determining the distance between each boundary point and the centroid of the ROI (see Figure 7.3). More specifically the Radial Distance time series (RD) is the distance between from each ROI boundary point $(x(i), y(i))$ to the centroid (x_c, y_c) of the ROI:

$$RD(i) = \sqrt{\left((x(i) - x_c)^2 + (y(i) - y_c)^2\right)}, \quad i = 1, 2, ..., N \tag{7.2}$$

where N is the number of boundary points. The centroid is computed as follows:

$$x_c = \frac{1}{N}\sum_{i=1}^{N} x(i), \quad y_c = \frac{1}{N}\sum_{i=1}^{N} y(i) \tag{7.3}$$

Note that, as in the case of the the ROI Int. method, the number of elements in the time series may vary from on image to another.

7.3 Similarity Measure Using Dynamic Time Warping

The objective of most similarity measures is to identify the distance between two feature vectors. There are a number of methods where this may be achieved. A common mechanism found in data mining, and especially text mining, is cosine similarity where the cosine of the angle θ between two vectors is used to determine similarity. If two vectors are identical ($\theta = 0$) the cosine similarity will be one, for all other angles the cosine similarity will be less than one. Alternatively we can compare each element in each vector individually. Both methods require the vectors to be compared to be identical in length.

In the case of time series the series can also be thought of in terms of feature vectors, although in this case it would not make sense to adopt measures such as the cosine measure. However, given two feature vector represented time series (of identical length), we can compare each pair of corresponding elements in the two vectors and determine a total difference measure by summing the individual differences. Various techniques are available to support difference measurement between feature vector represented time series, for example the Minkowsky metric. However, these techniques are not easily applicable given feature vectors of different lengths where there is no straight forward one-to-one correspondence between elements.

The time series used to describe the corpus callosum, as noted in Section 7.2, are not all of the same length; the number of spokes used to generate the time series is dependent on the size of the MBR surrounding the ROI and the number of radial distance measurements is dependent on the number of ROI boundary pixels . In this case an appropriate correspondence may be found by optimizing over all possible correspondences [130]. One such technique is Dynamic Time Warping (DTW). The DTW algorithm is a well-known algorithm in many areas. It was first introduced in 1960s [16] and extensively explored in 1970s for application within speech recognition systems. It is currently used in areas such as handwriting recognition and online signature matching [42], and protein sequence alignment [144]. DTW was adopted with respect to the proposed approach to allow for the comparison of pairs of corpora callosa.

DTW operates as follows. In order to align two time series (sequences) A and B with lengths N and M, an $N \times M$ matrix (D) is constructed, where each element (i, j) of the matrix contains the distance between the points A_i and B_j. The goal is to find a path through this matrix, which minimizes the sum of the local distances of the points. An illustration of the alignment between two time series is shown in Figure 7.4. The path from $(1, 1)$ to (N, M) in the matrix D is called the warping path W:

$$W = \{w_1, w_2, ..., w_k\} \tag{7.4}$$

and it is subject to several constraints.

- Boundary condition: This requires the warping path to start at $w_1 = (1, 1)$ and finish at $w_k = (N, M)$.

- Continuity: Given $w_k = (a, b)$, this constraint requires:

  $$w_{k-1} = (c, d) \tag{7.5}$$

  where:

  $$\begin{aligned} a - c &\leq 1, \\ b - d &\leq 1 \end{aligned} \tag{7.6}$$

  restricting the allowable steps in the warping path.

- Monotonicity: Given $w_k = (a, b)$ and $w_{k-1} = (c, d)$, this constraint requires:

  $$\begin{aligned} a - c &\geq 0, \\ b - d &\geq 0 \end{aligned} \tag{7.7}$$

The above inequalities force the points in W to be monotonically spaced in time. The warping path on the D matrix is found using some dynamic programming algorithm, which accumulates the partial distances between the sequences. If $D(i, j)$ is the global distance up to (i, j) and the local distance at (i, j) is given by $d(i, j)$, then the DTW algorithm uses the following recurrence relation:

$$D(i, j) = d(A_i, B_j) + \min \begin{cases} D(i-1, j-1) \\ D(i-1, j) \\ D(i, j-1) \end{cases} \tag{7.8}$$

Given $D(1, 1) = d(A_1, B_1)$ as the initial condition, we have the basis for an efficient recursive algorithm for computing $D(i, j)$. The algorithm starts from $D(1, 1)$ and iterates through the matrix by summing the partial distances until $D(N, M)$, which is the overall matching score of the times series (sequences) A and B. In Figure 7.4, given two time series (sequences) $A = [1, 5, 4, 6, 4, 3, 3, 7, 4]$ and $B = [1, 4, 4, 6, 6, 3, 3, 7, 2, 1]$. The DTW algorithm finds an optimal match between the entries of the time series with an overall matching score.

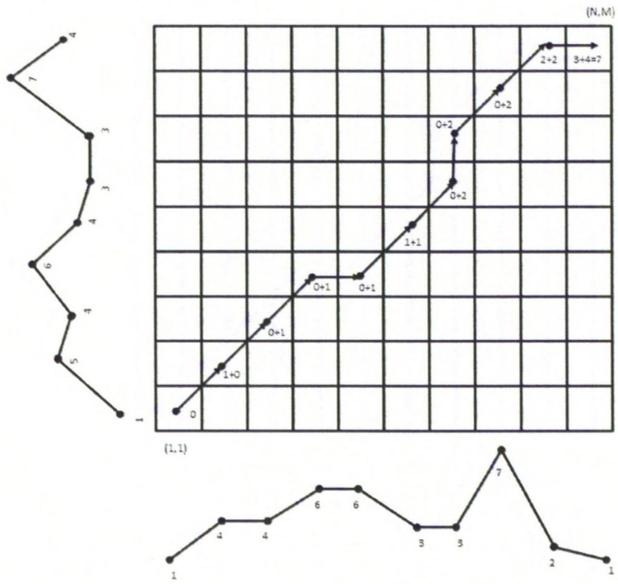

Figure 7.4: An example of the alignment of two time series using DTW, (D matrix and the warping path).

Algorithm 7.1: DTW algorithm

```
$N \leftarrow |A|$
$M \leftarrow |B|$
$D[\,] \leftarrow new[N \times M]$
$D(1,1) \leftarrow d(A_1, B_1)$
for $i \leftarrow 2$ to $N$ do
    $D(i,1) \leftarrow D(i-1,1) + d(A_i, B_1)$
end
for $j \leftarrow 2$ to $M$ do
    $D(1,j) \leftarrow D(1,j-1) + d(A_1, B_j)$
end
for $i \leftarrow 2$ to $N$ do
    for $j \leftarrow 2$ to $M$ do
        $D(i,j) \leftarrow d(A_i, B_j) + \min\{D(i-1,j-1), D(i,j-1), D(i-1,j)\}$
    end
end
return($D(N,M)$)
```

The DTW algorithm for the calculation of distance between two time series (sequences) A and B is given in Algorithm 7.1. Initially, the total distance of the cell $(1,1)$ is just its local distance $d(A_1, B_1)$. The absolute value distance (also called city block distance) is used for calculating the local distance. Then, the total distance for each successive cell in column 1 and row 1 is the local distance for the cell, plus the global distance to the cell previous to it. The algorithm iterates by calculating the global distance of the rest of the cells in the matrix using the recurrence relation. At the cell (i, j), the total distance is the local distance at (i, j) plus the minimum total distance at either $(i-1, j-1)$, $(i-1, j)$ or $(i, j-1)$. The overall distance between the sequences is the value stored in the cell (N, M).

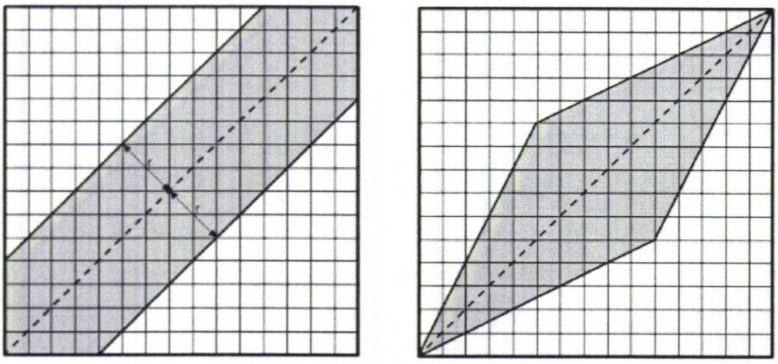

(a) (b)

Figure 7.5: Global warping path constraints: (a) Sakoe-Chiba band, and (b)Itakura parallelogram.

The computational cost of the application of DTW is $O(NM)$. In order to improve the computational cost global constraints may be introduced whereby we ignore matrix locations away from the main diagonal. Two well known global constraints are the "Sakoe-Chiba band" [127] and "Itakura parallelogram" [77], as shown in Figure 7.5. Alignments of points can be selected only from the respective shaded regions. The Sakoe-Chiba band runs along the main diagonal and has a fixed width R such that $j - R \leq i \leq j + R$ for the indices of the warping path $w_k(i, j)$ (see Figure 7.5(a)). While the Itakura parallelogram describes a region that constrains the slope of a warping path. More specifically, for a fixed $S > 1$, the Itakura parallelogram consists of all points that are traversed by some warping path having a slope between $1/S$ and S (see Figure 7.5(b)). There are several reasons for using global constraints, one of which is that they slightly speed up the DTW distance calculation. However, the most important reason is to prevent pathological warpings, where a relatively small section of one time series maps onto a relatively large section of another. In the work described here, the Sakoe-Chiba band was adopted.

7.4 Framework for Image Classification Based on Time Series Representation

The time series based image classification approach commences with the segmentation and registration of the input images as described in Chapter 3. Once the ROI have been segmented and identified the next step is to derive the time series according to the boundary line circumscribing the ROI. In each case the ROI is then represented using the proposed time series generation techniques described in Section 7.2. Each ROI signature is then conceptualised as a *proto-type* or case contained in a Case Base (CB), to which a Case Based Reasoning (CBR) mechanism can be applied. As noted in Chapter 2, CBR is a branch of Artificial Intelligence (AI) founded on the idea that humans solve problems according to their experience, i.e. CBR conjectures that humans solve problems by attempting to match previous successfully addressed problems to the current problem. As such a CBR system comprises a Case Base (CB) and some matching strategy to align a new problem (case) with previously solved problems (cases) in the CB. Typically it will not be possible to find an exact match and thus some matching strategy will have to be adopted to find the most relevant case or cases.

As noted previously CBR can be used for classification purposes where, given an unseen record (case), the record can be classified according to the "best match" discovered in the CB. With respect to proposed technique, and in the case of the corpus callosum application, the CB comprises a set of pre-labelled (classified) ROI time series "signatures", each describing a ROI record. The DTW time series matching strategy was then adopted to identify a best match with a new ("unseen") ROI signature. To do this each pre-labelled (classified) signature of size N was compared to the test signature of size M using the DTW technique and a sequence of similarity measures obtained. The well established k-nearest neighbour technique (KNN) was used to identify the most similar signature in the CB from which a class label was then extracted. In the experiments reported in

Table 7.1: TCV classification results of different datasets.

Datasets	ROI Int.			Rad. Dist.		
	Acc.	Sens.	Spec.	Acc.	Sens.	Spec.
Musician	98.11	100.00	96.23	94.34	96.23	92.45
Handedness	96.34	97.50	95.24	93.90	95.00	92.86
Ep_{106}	75.47	73.58	77.36	74.53	71.70	77.36
Ep_{159}	76.73	79.25	75.47	74.84	77.36	73.58
Ep_{212}	77.36	82.08	72.64	75.47	80.19	70.75

the following section 1-NN was used to identify the most similar image signature. In this manner an unseen record was classified according to the "best match" discovered in the CB.

7.5 Evaluation

The evaluation of the proposed time series based ROIBIC approach is described in this section. The evaluation was again conducted with respect to the corpus callosum application. The evaluation was undertaken in terms of classification accuracy, sensitivity and specificity. The three studies used to evaluate the previous techniques described in this thesis were again used for the investigation: (i) a comparison between musician and non-musician MRI scans, (ii) a comparison between left handedness and right handedness, and (iii) an epilepsy screening process.

Table 7.1 shows the Ten Cross Validation (TCV) results obtained using the different datasets and the two proposed time series generation techniques (ROI Int. and Rad. Dist.). Acc, Sens and Spec refer to accuracy, sensitivity and specificity respectively.

Inspection of Table 7.1 indicates that the best classification accuracy achieved, using the proposed ROI Int. time series generation method, for the musician and handedness datasets, were 98.11% and 96.34% respectively. The best sensitivity and specificity obtained were also associated with these best classification accuracies. As in the case of the reported evaluations for the previous ROIBIC approaches considered, the proposed approach did not perform as well for the epilepsy study (the results reflect the possibility that there are also other factors involved). Overall the proposed ROI Int signature generation method outperformed the Rad. Dist. method with respect to all five test datasets.

The limitation of the proposed ROI intersection signature generation method is that it does not lend itself to application to more complex, non-convex, ROIs. The method would fail to accurately capture the nature of a ROI if the spokes radiating from a reference point may intersect with the ROI boundary at more than two intersection places.

The time complexity of the image classification approach based on the time series representations, using the three datasets (musician, handedness and Ep_{212}), is presented in Figure 7.6. All the experiments were performed with 1.86 GHz Intel(R) Core(TM)2 PC with 2GB RAM. The code was designed using Matlab 7. The run time includes the time required for the proposed signature extraction process, as well as the CBR based classification.

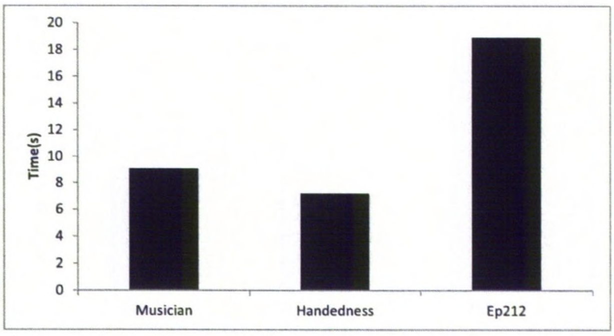

Figure 7.6: Run time complexity for the classification of different datasets.

7.6 Summary

In this chapter a new approach to ROIBIC based on time series representation has been described. Two image signature (pseudo time series) generation mechanisms were considered, (i) ROI intersection (ROI Int.) time series generation and (ii) radial distance (Rad. Dist.) time series generation. The first is a novel approach proposed by the author and directed specially at describing shapes such as the corpus callosum. The second, included for comparison purposes, is founded on an established shape description approach. Dynamic Time Warping was used to compare signatures as part of a CBR framework used to classify new records. The reported evaluation indicated that the ROI Int. time series generation method gave the best performance.

Chapter 8

Conclusion

A summary of the proposed ROI image classification approaches, the comparison between these approaches, the main findings, the research contribution and possible future directions, are presented in this chapter. Section 8.1 gives the summary of the proposed ROI image classification approaches. The comparison between these approaches with respect to their performance on the test data sets is presented in Section 8.2. Statistical comparison between theses approaches is presented in Section 8.3. The main findings and the contribution of the research work are presented in Section 8.4. Finally some directions for future research are presented in Section 8.5.

8.1 Summary

Four different ROIBIC approaches were proposed in this thesis to classifying (categorise) MRI brain scans according to the nature of the corpus callosum, a structure within the mammalian brain that connects the two brain hemispheres. The evaluation of these four approaches, on different data sets derived from the medical domain, suggests that there is no single ROIBIC approach that is best suited to all the image data sets considered. All the four ROIBIC approaches commenced with an image segmentation process so as to isolate and extract the desired ROI (the corpus callosum with respect to the scenario that formed the focus for the work described in this thesis). A variation of the Multiscale Normalized Cuts algorithm was proposed to achieve the desired segmentation. All the four ROI image classification approaches, although operating in very different manners, are essentially supervised learning mechanisms whereby a prelabelled training set was used to build a "classifier" which can then be applied to unseen data.

The first approach was founded on the concept of the Hough transform coupled with a polygonal approximation. The aim of the application of the polygonal approximation to the ROI was to obtain a smooth curve over a minimum number of line segments describing the regions boundary. The Hough transform was then used to extract a (1D) image signature vector, one per each image. The signatures from a labelled training set can thus be collected together and stored in a Case Base (CB) within a Case Based Reasoning (CBR) framework to be used in the context of image classification. The reported evaluation indicated that the proposed technique performed well in the case of the application of polygonal approximation compared with not using such an approximation.

The second approach was founded on the concept of graph mining. This approach used a hierarchical decomposition technique, coupled with a quad-tree based representation, one tree per image. A weighted frequent subgraph mining algorithm, gSpan-ATW, was then applied to identify frequently occurring subgraphs (subtrees) within the quad-tree representation. The general assumption for the application of the algorithm was that quad-tree nodes further away from the root were more significant than those nearer the root because the more distant nodes encapsulated a greater level of detail. The identified frequent subtrees were viewed as defining a feature space which could be used to represent the image set. A given image set can thus be recast into this format so that each image is represented by a feature vector whose elements are some subset of the global set of identified frequent subtrees making up the feature space. Standard classifier generation techniques can then be applied to build a classifier that can be applied to unseen data. The reported evaluation indicated that high classification accuracy results were obtained when using higher quad-tree decomposition levels coupled with low support thresholds.

The third approach was founded on using Zernike moments. A new method for the fast computation of Zernike moments, also based on a quad-tree decomposition, was proposed. Using the proposed computation method for the generation of exact Zernike moments reduced the computational time required for the overall classification process. A full set of Zernike moments was used in the context of the desired MR image classification. The reported evaluation indicated that the proposed technique gave more reasonable classification results using high orders of Zernike moments than when using lower orders.

The fourth approach was founded on the representation of ROI as time series. A new image signature generation mechanism, based on the size and shape of the ROI, was proposed. As in the case of the proposed Hough transform technique, the time series representing a particular image set were collected together in a CB forming part of a CBR framework. A dynamic time warping technique was adopted to calculate the similarity between new cases and time series held in the CB. The reported evaluation revealed that the proposed technique performed well with respect to the musicians and handedness studies, but not so well with respect to the epilepsy study.

8.2 Comparison of the Proposed Approaches

The four advocated approaches to ROI based image classification were evaluated in the context of the classification of brain MRI scans according to the nature of a particular ROI that appears across such datasets, namely the corpus callosum. This sections reports on an overall comparison between these approaches. The comparison was undertaken in terms of classification performance and run time complexity. The evaluation of each approach reported in the foregoing chapters, considered the effect of parameter settings associated with each approach, and is some cases variations of the approach. For the overall comparison reported in this section the best performing parameters and/or variations with respect to each technique were used (so as to consider each technique to its best advantage). Moreover, the proposed approaches were compared with the two notable techniques: the Curvature Scale Space (CSS) [102] (see Section 2.5.2.7) and the Angular Radial Transform (ART) [19] (see Section 2.5.1.3). These two techniques were used in this comparison because in the MPEG-7 standard, the curvature scale space (CSS) has been adopted as the contour-based shape descriptor and the angular radial transform (ART) has been adopted as the region-based shape descriptor.

Table 8.1 shows the TCV results obtained using the musician data set. The HT, GB, ZM, TS rows indicate the results using the Hough Transform, graph, Zernike moments, and time series based approaches respectively. The CSS, ART rows indicate the MPEG-7 descriptors (Curvature Scale Space and the Angular Radial Transform) respectively. The Acc, Sens, and Spec columns indicate accuracy, sensitivity and specificity respectively. The best results are indicated in **bold** font. Inspection of Table 8.1 demonstrates that the overall classification accuracies obtained using the four advocated approaches were over 90%, while the overall classification accuracy obtained using the time series based approach significantly improved over that obtained using the other three approaches. The best sensitivity and specificity were also obtained using the time series based approach. The four advocated approaches also outperform the CSS and ART techniques. These are excellent results.

Table 8.2 shows the TCV results obtained using the handedness data set. The column and row headers are defined as in Table 8.1. Inspection of Table 8.2 indicates that the four advocated approaches also performed well with respect to handedness study. The best overall classification results were again obtained using the time series based approach, which showed significant improvement over the other three approaches. The best sensitivity and specificity were also obtained also using time series based approach. The four advocated approaches also outperform the CSS and ART techniques. Again, these are excellent results.

Table 8.3 shows the TCV results obtained using the epilepsy data set (Ep_{212}). The column and row headers were defined as in Table 8.1. Inspection of Table 8.3 demonstrates that the Hough transform and time series based approaches did not perform as well as the other two approaches. The graph based and Zernike moments based approaches that consider all the pixels of each ROI in the feature extraction process outperformed the Hough transform and time series based approaches (recall that these approaches consider only the pixels of the boundary of the ROI). The four advocated approaches also outperform the CSS and ART techniques. The results for the epilepsy data set seem to be at odds with those obtained using the musicians and handedness studies. This was also noted with respect to the individual evaluations reported earlier in this thesis. Subsequent discussion with medical domain experts did not give an indication as to why this might be the case. However, as noted earlier, the suspicion is that the results reflect the fact that although the nature of the corpus callosum may

Table 8.1: TCV classification results of different approaches for musicians study.

	Acc	Sens	Spec
HT	91.51	92.45	90.57
GB	95.28	96.23	94.34
ZM	96.23	98.11	94.34
TS	**98.11**	**100.00**	**96.23**
CSS [102]	86.79	88.68	84.91
ART [19]	89.62	90.57	88.68

Table 8.2: TCV classification results of different approaches for handedness study.

	Acc	Sens	Spec
HT	90.24	92.50	88.1
GB	93.90	95.00	92.86
ZM	93.90	95.00	92.86
TS	**96.34**	**97.50**	**95.24**
CSS [102]	85.37	85.00	85.71
ART [19]	87.80	90.00	85.71

play a part in the identification of epilepsy there are also other factors involved.

With respect to classification accuracy in general all four ROI based image classification approaches performed remarkably well, although the time series based approach produced the best results for the musicians and handedness studies while the graph based approach produced the best results for the epilepsy study. There is no obvious reason why this might be the case, visual inspection of the MRI scans does not indicate any obvious distinguishing attributes with respect to the size and shape of the corpus callosum. Tracing the cause of a particular classification back to a particular part of the corpus callosum is thus seen

Table 8.3: TCV classification results of different approaches for epilepsy study (Ep_{212}).

	Acc	Sens	Spec
HT	76.42	81.13	71.70
GB	**86.32**	**87.74**	**84.91**
ZM	85.38	87.74	83.02
TS	77.36	82.08	72.64
CSS [102]	68.40	72.64	64.15
ART [19]	70.28	73.58	66.98

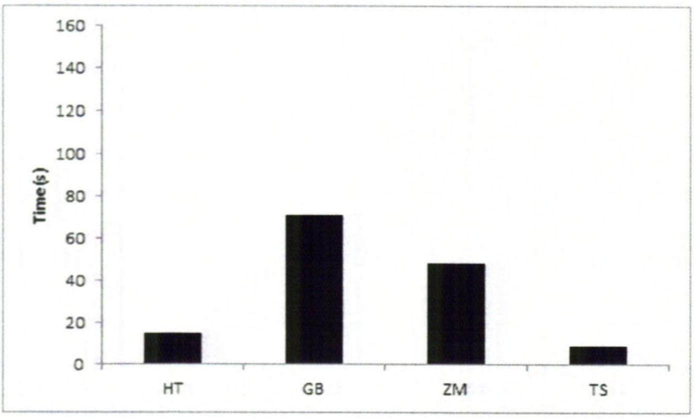

Figure 8.1: Run time complexity for the classification of the musician dataset using the four proposed ROIBIC approaches.

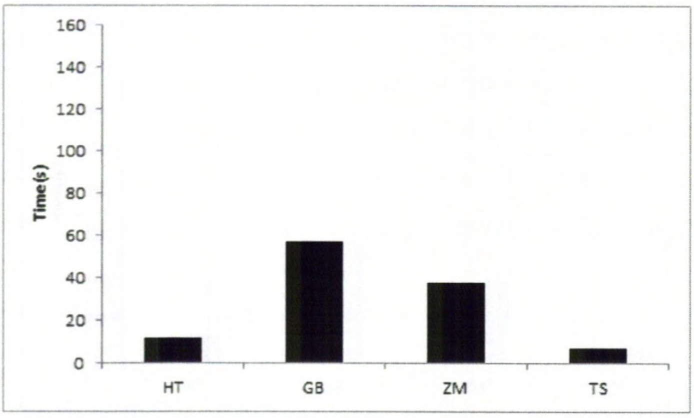

Figure 8.2: Run time complexity for the classification of the handedness dataset using the four proposed ROIBIC approaches.

as a desirable "avenue" for future research (see below). It is also interesting to note that the Hough transform based approach performed consistently badly with respect to all of the above evaluation studies suggesting that generating shape signatures using the Hough transform is not a technique to be recommended in the context of feature based classification, although the use of Hough transform is popular in other branches of image analysis.

In the literature there are a few reported studies on classifying medical images according to the nature of the corpus callosum. For example, Sampat et al. [129] used the cross sectional area of the corpus callosum and the inferior subolivary medulla oblongata volume (MOV) to distinguish patients with relapsing-remitting multiple sclerosis (RRMS), secondary-progressive multiple sclerosis (SPMS), and primary-progressive multiple sclerosis (PPMS). Their study produced a classification accuracy of 80%. Fahmi et al. [46] proposed a classification approach in order to distinguishing between healthy controls and autistic patients according to the nature of the corpus callosum. They analysed the displacement fields generated from the non-rigid registration of different corpus callosum segments onto a chosen reference within each group. Their reported result indicated that the classification accuracy was 86%. Golland et al. [57] adopted a version of skeletons for feature extraction coupled with the Fisher linear discriminant and the linear support vector machines for the classification of corpus callosum data for schizophrenia patients. The best classification accuracy achieved using the support vector machine classification method was less than 80%. These studies indicated how impressive are the classification results obtained using the four proposed ROIBIC approaches. The results obtained using the mechanism proposed in this thesis significantly improved on the results produced in these earlier studies.

The classification of medical images may be affected by the preprocessing procedures applied to the input image set; these procedures include image registration and image segmentation. The aim of medical image registration is to establish spatial correspondence between one image and another, an image and an atlas or an image and some physical space. Accurate registration of brain MRI scans is critical to any image classification study. The presence of any registration and segmentation errors produced in delineating the ROIs in the images may affect the accuracy of image classification. Therefore testing of robustness of the proposed ROIBIC approaches with respect to both registration and segmentation errors is an ongoing and important problem to be considered as a part of future work.

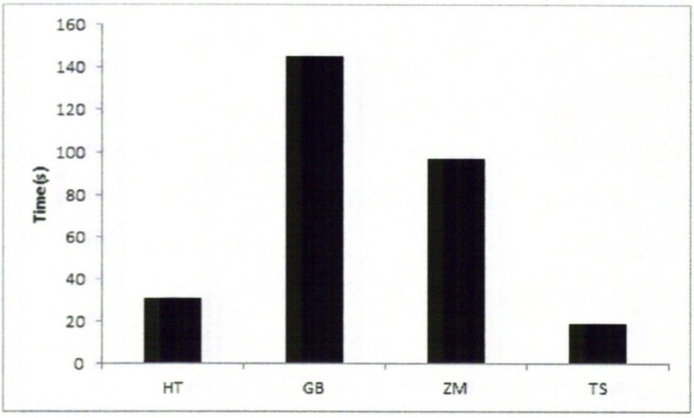

Figure 8.3: Run time complexity for the classification of the epilepsy dataset (*Ep*212) using the four proposed ROIBIC approaches.

The run time complexity of the four ROIBIC approaches using the musician, handedness, and *Ep*212 datasets, are presented in Figures 8.1, 8.2, and 8.3 respectively. The classification time is the overall run time, i.e. it incorporates the feature extraction, training and testing phases. All the experiments were performed with 1.86 GHz Intel(R) Core(TM)2 PC with 2GB RAM. The graph based approach was computationally the most expensive, while the time series based approach was computationally the least expensive. However, it is worth remarking that, especially in the medical context, it is the classification accuracy, not speed, which is the most important feature of the proposed processes.

In summary we can note that there is no constant "winner" among the four proposed ROI based image classification approaches. However, excellent classification results were produced.

8.3 Statistical Comparison of the Proposed Image Classification Approaches

Statistical tests in the literature mainly use error rate for comparison. Receiver Operating Characteristics (ROC) curves and/or Area Under the ROC Curve (AUC) statistic can also be used for comparing classifier performances as proposed by Baesens et al. [8].

The ROC is a two dimensional graphical illustration of the trade-off between the true positive rate (sensitivity) and false positive rate (1-specificity). The ROC curve illustrates the behaviour of a classifier without having to take into consideration the class distribution or misclassification cost. In order to compare the ROC curves of different classifiers, the Area Under the receiver operating characteristic Curve (AUC) must be computed. An example of ROC curve is depicted in Figure 8.4. The diagonal line represents the trade-off between the sensitivity and (1-specificity) for a random model, and has an AUC of 0.5. For a well performing classifier the ROC curve needs to be as far to the top left-hand corner as possible. In the example shown in Figure 8.4, the classifier that performs the best is the ROC_1 curve.

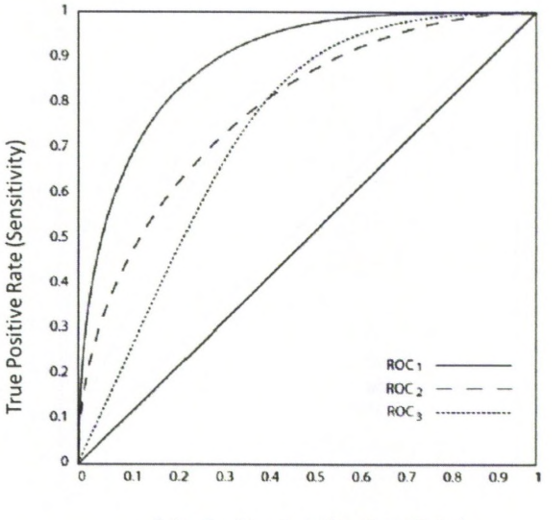

Figure 8.4: An example of ROC curve.

Friedman's test [36, 54] was used to compare the AUCs of the different clas-

Table 8.4: Area Under the receiver operating characteristic Curve (AUC) results.

	Friedman test statistic = 10.68 ($p < 0.005$)					
	Musician	Handedness	Ep_{106}	Ep_{159}	Ep_{212}	AR
HT	92.6 (4)	91.3 (4)	74.2 (4)	77.0 (4)	78.6 (4)	4
GB	97.1 (2)	96.2 (2)	**86.4** (1)	**87.7** (1)	**88.3** (1)	**1.4**
ZM	96.4 (3)	94.7 (3)	85.6 (2)	86.4 (2)	87.2 (2)	2.4
TS	**99.1** (1)	**96.8** (1)	76.5 (3)	78.7 (3)	79.3 (3)	2.2

sifiers. The Friedman test statistic is based on the average ranked (AR) performances of the classification techniques on each data set, and is calculated as follows:

$$\chi_F^2 = \frac{12N}{K(K+1)}\left[\sum_{j=1}^{K} AR_j^2 - \frac{K(K+1)^2}{4}\right] \tag{8.1}$$

where $AR_j = \frac{1}{N}\sum_{i=1}^{N} r_i^j$, N denotes the number of data sets used in the study, K is the total number of classifiers and r_i^j is the rank of classifier j on data set i. χ_F^2 is distributed according to the Chi-square distribution with $K-1$ degrees of freedom. If the value of χ_F^2 is large enough, then the null hypothesis that there is no difference between the techniques can be rejected. The Friedman statistic is well suited for this type of data analysis as it is less susceptible to outliers.

The post hoc Nemenyi test [36] was applied to report any significant differences between individual classifiers. The Nemenyi post hoc test states that the performances of two or more classifiers are significantly different if their average ranks differ by at least the Critical Difference (CD), given by

$$CD = q_{\alpha,\infty,K}\sqrt{\frac{K(K+1)}{12N}} \tag{8.2}$$

Table 8.4 reports the AUCs for all four techniques when applied to the five data sets. The numbers in the parentheses indicate the average rank of each technique. The Friedman test statistic and corresponding p-value is also shown. As these were all significant ($p < 0.005$) the null hypothesis that there is no difference between the techniques can be rejected and a post hoc Nemenyi test applied to each class distribution. In Table 8.4 the technique achieving the highest AUC on each data set and the overall highest ranked technique is indicated in bold font. From the table it can be seen that the graph based approach (GB) has the highest Friedman score (average rank (AR)). The AR of the Hough transform approach are statistically worse than the AR of the Graph based approach at the 5% critical difference level ($\alpha = 0.05$), as shown in the significance diagram in Figure 8.5. In this formula, the value $q_{\alpha,\infty,K}$ is based on the Studentised range statistic [36]. The results from the Friedmans statistic and the Nemenyi post hoc tests are displayed using a modified version of the Demšar (2006) significance diagram [90]. This diagram displays the ranked performances of the classification techniques, along with the critical difference, to highlight any techniques which are significantly different to the best performing classifiers.

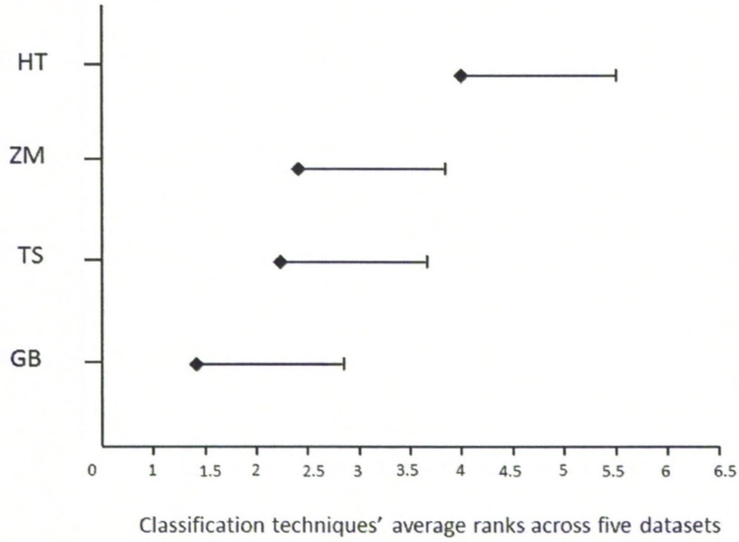

Figure 8.5: AR comparison between the proposed image classification approaches.

Figure 8.5 displays the AUC performance rank of the proposed image classification approaches, along with Nemenyi's critical difference (CD) tail. The CD value for the diagram shown in Figure 8.5 is equal to 1.48. This diagram shows the classification techniques listed in ascending order of ranked performance on the y-axis, and the image classification techniques' average rank across all five data sets displayed on the x-axis. The graph based (GB) approach is the best performing classification technique with an AR value of 1.4. This diagram clearly shows that, despite its popularity, the Hough transform performs significantly worse than the best performing classifier with value of 4.

In summary, when considering the AUC performance measures, it can be concluded that the graph based technique yields a very good performance. However, Hough transform approach performs significantly worse than the best performing technique. The majority of classification techniques yielded classification performances that are quite competitive with each other.

8.4 Main Findings and Contributions

In this thesis, the concept of image classification according to the nature of ROIs contained within image data set, was considered. Four ROIBIC approaches were proposed. These approaches considered four different ROI representations to maintain the structural information (shape and size) of ROIs coupled with an appropriate classification technique. The proposed approaches were designed to address the research question introduced in Chapter 1 and a number of associated research issues. In this Section the research question and issues are returned to. In the following each of the identified research issues is discussed in turn and the manner in which the proposed research addresses each individual issue briefly highlighted.

(a) **"The techniques derived should serve to maximize classification accuracy."**

The proposed approaches, as described in Chapters 4, 5, 6 and 7, were able to achieve high classification accuracy in the context of classifying different image data sets.

(b) **"To achieve the desired classification accuracy any proposed feature extraction (representation) method should capture the salient elements of the ROI without knowing in advance what those salient elements might be. In other words any proposed feature extraction method, whatever form this might take, should retain as much relevant information as possible."**

According to the work described in Chapters 4, 5, 6 and 7, the different representations of ROI were able to capture the salient elements of the ROI under consideration (the corpus callosum) so as to maintain the structural information (shape and size) of these ROIs. As proposed in Chapter 5, the application of a *weighting scheme* puts an emphasis on the most important frequent subgraphs instead of identifying all the frequent subgraphs during the mining process. Also, using exact Zernike moments with a higher order, effectively captures the salient elements of a ROI as described in Chapter 6. Similarly, the signature approach based on the Hough transform and the time series approaches were also able to capture these salient elements.

(c) **"It is also desirable to conduct the classification in reasonable time, there is thus a trade off between accuracy and efficiency that must be addressed."**

Some of the proposed approaches conducted the desired classification in reasonable time, such as the Hough transform and time series approaches (without any speed up mechanisms). With regard to the graph based approach, the application of a *weighting scheme* (ATW) enabled the weighted FSM algorithm (gSpan-ATW) to identify a significantly smaller number of frequent subgraphs than might have been achieved using standard FSM algorithms. Of note also is the mechanism proposed to speed up of the computation of exact Zernike moments so as to reduce the overall classification time with respect to the Zernike moments approach.

(d) **"Not all potential representations are compatible with all available classification paradigms, thus different representations may require the application of different classification techniques."**

The proposed approaches worked in different manners according to the nature of the proposed ROI representation. Using the Hough transform and time series approaches a CBR technique was adopted to classify the unseen cases. Although different similarity measures were used, *euclidean distance* for the Hough transform technique and DTW for the time series based approach. Standard classification techniques (SVM and decision trees) were adopted in the case of the graph and Zernike moments based approaches. Therefore it is possible to conclude that the adopted classification mechanism were dependent on the nature of the ROI representation technique adopted.

Returning to Chapter 1, the overriding research question was: **"How best to process image collections so that efficient and effective classifica-**

tion, according to some ROI contained across the image set, can be achieved?"

The work described in the foregoing chapters clearly indicates that the answer to this question is that the proposed ROI representations, coupled with appropriate classification techniques, can clearly classify such images in a way that is both efficient and effective.

The primary contributions of the research work presented in this thesis can thus be summarized as follows:

(a) A variation of the *multiscale normalized cuts algorithm* to achieve the desired segmentation and delineating of a ROI contained across an image data set.

(b) A novel approach to MR image classification based on the Hough transform coupled with a polygonal approximation.

(c) An effective approach to MR image classification based on a quad tree represented hierarchical decomposition coupled with a weighted frequent subgraph mining algorithm.

(d) A novel mechanism to speed up the computation of exact Zernike Moments, also based on a quad-tree decomposition, and the usage of the resulting Zernike moments to define signatures for input to a classification system.

(e) An effective mechanism to describe ROIs in the form of a time series coupled with the use dynamic time warping to determine the similarity between images within the context of a CBR framework.

8.5 Future Work

The research described in this thesis has sparked a number of promising directions for future research. In the concluding section of this chapter, and this thesis, these future research directions are briefly outlined below.

- **Explanation facility.** In Section 8.2 it was noted that although excellent classification results were produced (using all four methods) none of the methods included an explanation facility. If any of the proposed techniques are to be used in clinical practice the clinicians using the techniques will require some explanation as to the reason for a particular classification. Therefore mechanisms whereby the cause of a particular classification can be traced back, through the representation, to a particular part of the ROI under consideration is therefore seen as an important avenue for future research.

- **Classification of volumetric medical image datasets.** The work described in this thesis has concentrated on 2D analysis. One avenue for proposed future work would seek to investigate feature based classification techniques that can be applied to 3D volumetric data. The work would require the extension of the proposed techniques to encompass 3D data as follows:

  - 3D Tree Based Representations: Current work has been directed at quad-trees, however this can be extended into 3D space by adopting an oct-tree representation.
  - 3D Time Series Based Representations: A 3D feature can be described in terms of a "mesh" which in turn can be described in terms of a series of "time series curves" and thus a sequence of time series comparisons can be applied within a CBR setting. Alternatively we can describe features in terms of a 3D surface and extend existing (2D) time series techniques so that they can be applied to such surfaces.
  - 3D Zernike moments: Current work has been directed at 2D Zernike moments, however this can be extended into 3D space using 3D Zernike moments. Consequently, there will be a further need to speed up the computation of Zernike moments.
  - Hough transform can be extended into 3D space using 3D Hough transform.

  Note that the application of all these techniques will also require 3D segmentation and registration so that the desired 3D objects can be isolated. The main challenge will be the significant size of the volumetric data sets to be considered (an order of magnitude greater than the 2D images considered in this thesis).

- **Parallel weighted frequent subgraph mining.** The inherent combinatorial complexity of the frequent subgraph mining process continues to present a challenge as we wish to mine graph sets of ever increasing size, especially when extending the tree representation from the 2D (quad-tree) representation to the 3D (oct-tree) representation. Weighted frequent subgraph mining can alleviate this computation to some degree. An alternative approach is to adopt some sort of parallel weighted frequent subgraph mining.

- **Integrating feature selection into the weighted FSM algorithms.** Feature selection plays an important role in the framework for image classification based on weighted FSM. It is it possible to incorporate feature selection techniques into weighted FSM so as to directly identify the most discriminative weighted subgraphs which are effective with respect to the classification task. There is still much room for additional researcher to utilize classic data mining techniques and integrate them into weighted FSM.

- **Ensemble of ROI based image classifiers.** The work described in this thesis established that, at least in the context of the corpus callosum application, no single best classification algorithm can be identified. The use of "ensembles" of different classifiers as an alternative approach based on the exploitation of the complementary characteristics of different classifiers may offer a promising mechanism for increasing overall classification accuracy. From the literature we can identify a number of techniques to generate ensemble classifiers, the most common are *bagging* and *boosting*. The basic idea of ensemble classifiers based on *bagging* is to build independent classifiers and use a voting scheme to establish the most appropriate class label for each test image. More investigation is needed with respect to ROI based image classification to determine how this might be implemented. The basic idea of *boosting* is to feed the results from one classifier into another so as to improve the initial classification results. Typically a number of "weak" classifiers are used in sequence. Thus *boosting* attempts to produce new classifiers that are better able to predict cases for which the current ensemble's performance is poor. Again further work is required on how best this may be implemented with respect to ROIBIC.

- **Experiments with alternative data sets.** The evaluation described in this thesis has concentrated on ROIBIC using the corpus callosum found in MRI data. The work does not necessarily establish a generic ROIBIC approach. Further experiments and evaluation are therefore desirable to establish whether the proposed approaches have generic applications. There are other objects located in MRI scans to which ROIBIC may be applied, for example the ventricles.

Bibliography

[1] A. Aamodt and E. Plaza. Case-based reasoning: foundational issues, methodological variations, and system approaches. *AI Communications*, 7:39–59, 1994.

[2] R. Agrawal and R. Srikant. Fast algorithms for mining association rules in large databases. In *Proceedings of the 20th International Conference on Very Large Data Bases*, VLDB'94, pages 487–499. Morgan Kaufmann Publishers Inc., 1994.

[3] M. Ahmed, S. Yamany, N. Mohamed, A. Farag, and T. Moriarty. A modified fuzzy c-means algorithm for bias field estimation and segmentation of mri data. *IEEE Transactions on Medical Imaging*, 21(3):193 –199, 2002.

[4] L. Allen, M. Richey, Y. Chain, and R. Gorski. Sex differences in the corpus callosum of the living human being. *Journal of Neuroscience*, 11(4):933–942, 1991.

[5] B. André, T. Vercauteren, A. Perchant, A. M. Buchner, M. B. Wallace, and N. Ayache. Endomicroscopic image retrieval and classification using invariant visual features. In *Proceedings of the Sixth IEEE international conference on Symposium on Biomedical Imaging: From Nano to Macro*, ISBI'09, pages 346–349. IEEE Press, 2009.

[6] F. Attneave. Some informational aspects of visual perception. *Psychological Review*, 61(3):183–193, 1954.

[7] U. Avni, J. Goldberger, M. Sharon, E. Konen, and H. Greenspan. Chest x-ray characterization: from organ identification to pathology categorization. In *Proceedings of Multimedia Information Retrieval*, pages 155–164. ACM, 2010.

[8] B. Baesens, T. Van Gestel, S. Viaene, M. Stepanova, J. Suykens, and J. Vanthienen. Benchmarking state-of-the-art classification algorithms for credit scoring. *Journal of the Operational Research Society*, 54(6):627–635, 2003.

[9] X. Bai, L. Latecki, and W. Liu. Skeleton pruning by contour partitioning with discrete curve evolution. *IEEE Transactions on Pattern Analysis and Machine Intelligence*, 29(3):449 –462, 2007.

[10] R. Bailey and M. Srinath. Orthogonal moment features for use with parametric and non-parametric classifiers. *IEEE Transactions on Pattern Analysis and Machine Intelligence*, 18:389–399, 1996.

[11] C. Baillard, P. Hellier, and C. Barillot. Segmentation of brain 3d mr images using level sets and dense registration. *Medical Image Analysis*, 5(3):185 – 194, 2001.

[12] D. Ballard. Generalizing the hough transform to detect arbitrary shapes. *Pattern Recognition*, 13(2):111–122, 1981.

[13] E. Barbu, P. Hroux, S. Adam, and E. Trupin. Clustering document images using graph summaries. In *Proceedings of the 5th International Conference on Learning and Data Mining*, pages 194–202, 2005.

[14] S. Barker and P. Rayner. Unsupervised image segmentation using markov random field models. In *Proceedings of the First International Workshop on Energy Minimization Methods in Computer Vision and Pattern Recognition*, pages 165–178, 1997.

[15] S. Belkasim, M. Shridhar, and M. Ahmadi. Pattern recognition with moment invariants: A comparative study and new results. *Pattern Recognition*, 24(12):1117–1138, 1991.

[16] R. Bellman and R. Kalaba. On adaptive control processes. *IRE Transactions on Automatic Control*, 4(2):1 – 9, 1959.

[17] M. Berry. *Survey of Text Mining*. Springer-Verlag New York, Inc., 2003.

[18] M. Berry and G. Linoff. *Data Mining Techniques. For Marketing, Sales, and Customer Support.* Wiley, 1997.

[19] M. Bober. Mpeg-7 visual shape descriptors. *IEEE Transactions on Circuits and Systems for Video Technology*, 11(6):716 –719, 2001.

[20] J. Canny. A computational approach to edge detection. *IEEE Transactions on Pattern Analysis and Machine Intelligence*, 8:679–698, 1986.

[21] K. Castleman. *Digital Image Processing.* Prentice Hall Professional Technical Reference, 1996.

[22] C. Chang and C. Lin. Libsvm: a library for support vector machines. 2001. Software available at `http://www.csie.ntu.edu.tw/~cjlin/libsvm`.

[23] C. Chong, P. Raveendran, and R. Mukundan. A comparative analysis of algorithms for fast computation of zernike moments. *Pattern Recognition*, 36(3):731 – 742, 2003.

[24] C. Cocosco, A. Zijdenbos, and A. Evans. Adaptive, template moderated, spatially varying statistical classification. *Medical Image Analysis*, 7:513–527, 2003.

[25] F. Cohen, Z. Huang, and Z. Yang. Invariant matching and identification of curves using b-splines curve representation. *IEEE Transactions on Image Processing*, 4(1):1 –10, 1995.

[26] F. Cohen and J. Wang. Part i: Modeling image curves using invariant 3-d object curve models - a path to 3-d recognition and shape estimation from image contours. *IEEE Transactions on Pattern Analysis and Machine Intelligence*, 16:1–12, 1994.

[27] P. Conlon and M. Trimble. A study of the corpus callosum in epilepsy using magnetic resonance imaging. *Epilepsy Research*, 2(2):122–126, 1988.

[28] C. Cortes and V. Vapnik. Support-vector networks. *Machine Learning*, 20:273–297, 1995.

[29] L. Costa and R. Cesar Jr. *Shape Analysis and Classification: Theory and Practice.* CRC Press, 2001.

[30] T. Cour, F. Benezit, and J. Shi. Spectral segmentation with multiscale graph decomposition. In *Proceedings of the 2005 IEEE Computer Society Conference on Computer Vision and Pattern Recognition (CVPR'05) - Volume 2*, CVPR '05, pages 1124–1131. IEEE Computer Society, 2005.

[31] P. Cowell, A. Kertesz, and V. Denenberg. Multiple dimensions of handedness and the human corpus callosum. *Neurology*, 43(11):2353–2357, 1993.

[32] R. Damadian, M. Goldsmith, and L. Minkoff. Nmr in cancer: Xvi. fonar image of the live human body. *Physiological Chemistry and Physics*, 9(1):97–100, 1977.

[33] M. Das, M. Paulik, and N. Loh. A bivariate autoregressive technique for analysis and classification of planar shapes. *IEEE Transactions on Pattern Analysis and Machine Intelligence*, 12(1):97 –103, 1990.

[34] C. Davatzikos, M. Vaillant, S. Resnick, J. Prince, S. Letovsky, and R. Bryan. A computerized approach for morphological analysis of the corpus callosum. *Computer Assisted Tomography*, 20(1):88–97, 1996.

[35] E. Davies. *Machine Vision: Theory, Algorithms, Practicalities.* Morgan Kaufmann Publishers Inc., 2004.

[36] J. Demšar. Statistical comparisons of classifiers over multiple data sets. *Journal of Machine Learning Research.*, 7:1–30, 2006.

[37] D. Douglas and T. Peucker. Algorithm for the reduction of the number of points required to represent a line or its caricature. *The Canadian Cartographer*, 10:112–122, 1973.

[38] R. Duara, A. Kushch, K. Gross-Glenn, W. Barker, B. Jallad, S. Pascal, D. Loewenstein, J. Sheldon, M. Rabin, B. Levin, and H. Lubs. Neuroanatomic differences between dyslexic and normal readers on magnetic resonance imaging scans. *Archives of Neurology*, 48(4):410–416, 1991.

[39] S. Dubois and F. Glanz. An autoregressive model approach to two-dimensional shape classification. *IEEE Transactions on Pattern Analysis and Machine Intelligence*, PAMI-8(1):55 –66, 1986.

[40] R. Duda and P. Hart. Use of the hough transformation to detect lines and curves in pictures. *Communications of the ACM*, 15:11–15, 1972.

[41] R. Duda, P. Hart, and D. Stork. *Pattern Classification (2nd Edition).* Wiley-Interscience, 2001.

[42] A. Efrat, Q. Fan, and S. Venkatasubramanian. Curve matching, time warping, and light fields: New algorithms for computing similarity between curves. *Journal of Mathematical Imaging and Vision*, 27:203–216, 2007.

[43] A. Elsayed, F. Coenen, M. García-Fiñana, and V. Sluming. Region of interest based image categorization. In *Proceedings of the 12th international conference on Data warehousing and knowledge discovery*, DaWaK'10, pages 239–250, Berlin, Heidelberg, 2010. Springer-Verlag.

[44] A. Elsayed, F. Coenen, M. García-Fiñana, and V. Sluming. Region of interest based image classification using time series analysis. In *Proceedings of The 2010 International Joint Conference on Neural Networks (IJCNN)*, pages 1–6, 2010.

[45] A. Elsayed, F. Coenen, C. Jiang, M. García-Fiñana, and V. Sluming. Corpus callosum mr image classification. *Knowledge-Based Systems*, 23:330–336, 2010.

[46] R. Fahmi, A. El-Baz, H. Abd El Munim, A. Farag, and M. Casanova. Classification techniques for autistic vs. typically developing brain using mri data. In *4th IEEE International Symposium on Biomedical Imaging: From Nano to Macro, 2007. ISBI 2007.*, pages 1348 –1351, 2007.

[47] U. Fayyad, G. Piatetsky-shapiro, and P. Smyth. From data mining to knowledge discovery in databases. *AI Magazine*, 17:37–54, 1996.

[48] U. Fayyad, G. Piatetsky-shapiro, and P. Smyth. Knowledge discovery and data mining: Towards a unifying framework. In *Proceedings of The International Conference on Knowledge Discovery and Data Mining (KDD'96)*, pages 82 – 88. AAAI Press, 1996.

[49] U. Fayyad, G. Piatetsky-Shapiro, P. Smyth, and R. Uthurusamy. *Advances in Knowledge Discovery and Data Mining.* American Association for Artificial Intelligence, 1996.

[50] P. Freeborough and N. Fox. The boundary shift integral: an accurate and robust measure of cerebral volume changes from registered repeat mri. *IEEE Transactions on Medical Imaging*, 16(5):623 –629, 1997.

[51] H. Freeman. On the encoding of arbitrary geometric configurations. *IRE Transactions on Electronic Computers*, EC-10(2):260 –268, 1961.

[52] H. Freeman and J. Saghri. Comparative analysis of line-drawing modeling schemes. *Computer Graphics and Image Processing*, 12(3):203 – 223, 1980.

[53] Y. Freund and R. Schapire. A decision-theoretic generalization of on-line learning and an application to boosting. *Journal of Computer and System Sciences*, 55:119–139, 1997.

[54] M. Friedman. A comparison of alternative tests of significance for the problem of m rankings. *Annals of Mathematical Statistics*, 11:86–92, 1940.

[55] G. Gerig, M. Styner, D. Jones, D. Weinberger, and J. Lieberman. Shape analysis of brain ventricles using spharm. *IEEE Workshop on Mathematical Methods in Biomedical Image Analysis*, 0:171–178, 2001.

[56] R. Goebel, F. Esposito, and E. Formisano. Analysis of functional image analysis contest (fiac) data with brainvoyager qx: From single-subject to cortically aligned group general linear model analysis and self-organizing group independent component analysis. *Human Brain Mapping*, 27(5), 2006.

[57] P. Golland, W. Grimson, and R. Kikinis. Statistical shape analysis using fixed topology skeletons: Corpus callosum study. In *Proceedings of The 16th International Conference on Information Processing and Medical Imaging IPMI'99*, volume 16, pages 382–387, 1999.

[58] G. Golub and C. Van Loan. *Matrix computations (3rd ed.).* Johns Hopkins University Press, 1996.

[59] R. Gonzalez and R. Woods. *Digital Image Processing.* Addison-Wesley, 2002.

[60] M. Hall, E. Frank, G. Holmes, B. Pfahringer, P. Reutemann, and I. Witten. The weka data mining software: an update. *SIGKDD Explorations Newsletter*, 11:10–18, 2009.

[61] H. Hampel, S. Teipel, G. Alexander, B. Horwitz, D. Teichberg, M. Schapiro, and S. Rapoport. corpus callosum atrophy is a possible indicator of region and cell type-specific neuronal degeneration in alzheimer disease. *Archives of Neurology*, 55(2):193–198, 1998.

[62] J. Han and M. Kamber. *Data Mining: Concepts and Techniques, Second Edition (The Morgan Kaufmann Series in Data Management Systems).* Morgan Kaufmann, 2006.

[63] J. Han, J. Pei, and Y. Yin. Mining frequent patterns without candidate generation. In *Proceedings of the 2000 ACM SIGMOD international conference on Management of data*, SIGMOD '00, pages 1–12, 2000.

[64] D. Hand, P. Smyth, and H. Mannila. *Principles of data mining.* MIT Press, 2001.

[65] A. Hassanien. Fuzzy rough sets hybrid scheme for breast cancer detection. *Image and Vision Computing*, 25:172–183, 2007.

[66] Y. He and A. Kundu. 2-d shape classification using hidden markov model. *IEEE Transactions on Pattern Analysis and Machine Intelligence*, 13(11):1172 -1184, 1991.

[67] P. Hough. Method and means for recognizing complex patterns, 1962.

[68] G. Howell, D. Fausett, and L. Fausett. Quasi-circular splines: a shape-preserving approximation. *CVGIP: Graphical Models and Image Processing*, 55:89–97, 1993.

[69] W. Hsu, M. Lee, and J. Zhang. Image mining: Trends and developments. *Journal of Intelligent Information Systems*, 19:7–23, 2002.

[70] M. Hu. Visual pattern recognition by moment invariants. *IRE Transactions on Information Theory*, IT-8:179–187, 1962.

[71] S. Hu and D. Collins. Joint level-set shape modeling and appearance modeling for brain structure segmentation. *NeuroImage*, 36(3):672 – 683, 2007.

[72] J. Huan, W. Wang, and J. Prins. Efficient mining of frequent subgraph in the presence of isomorphism. In *Proceedings of the 2003 International Conference on Data Mining (ICDM'03)*, pages 549–552, 2003.

[73] J. Huan, W. Wang, A. Washington, J. Prins, R. Shah, and A. Tropsha. Accurate classification of protein structural families using coherent subgraph analysis. In *Proceedings of Pacific Symposium on Biocomputing*, pages 411–422, 2004.

[74] G. Hynd, J. Hall, E. Novey, D. Eliopulos, K. Black, J. Gonzalez, J. Edmonds, C. Riccio, and M. Cohen. Dyslexia and corpus callosum morphology. *Archives of Neurology*, 52(1):32–38, 1995.

[75] A. Inokuchi, T. Washio, and H. Motoda. An apriori-based algorithm for mining frequent substructure from graph data. In *Proceedings of the Fourth European Conference on Principles and Practice of Knowledge Discovery in Databases*, pages 13–23, 2000.

[76] A. Inokuchi, T. Washio, K. Nishimura, and H. Motoda. A fast algorithm for mining frequent connected subgraphs. Research Report RT0448, IBM Research, Tokyo Research Laboratory, 2002.

[77] F. Itakura. Minimum prediction residual principle applied to speech recognition. *IEEE Transactions on Acoustics, Speech and Signal Processing*, 23(1):67–72, 1975.

[78] V. Jeanne, D. Unay, and V. Jacquet. Automatic detection of body parts in x-ray images. In *Proceedings of IEEE Computer Society Conference on Computer Vision and Pattern Recognition Workshops, 2009. CVPR Workshops 2009.*, pages 25 –30, 2009.

[79] C. Jiang and F. Coenen. Graph-based image classification by weighting scheme. In *Proceedings of the 2008 SGAI International Conference on Artificial Intelligence (AI'08)*, pages 63–76, 2008.

[80] S. Joshi, S. Pizer, P. Fletcher, P. Yushkevich, A. Thall, and J. Marron. Multiscale deformable model segmentation and statistical shape analysis using medial descriptions. *IEEE Transactions on Medical Imaging*, 21(5):538 – 550, 2002.

[81] C. Kan and M. Srinath. Invariant character recognition with zernike and orthogonal fourier-mellin moments. *Pattern Recognition*, 35(1):143 – 154, 2002.

[82] R. Kashyap and R. Chellappa. Stochastic models for closed boundary analysis: Representation and reconstruction. *IEEE Transactions on Information Theory*, 27(5):627 – 637, 1981.

[83] A. Kharrat, K. Gasmi, M. Ben messaoud, N. Benamrane, and M. Abid. Content-based image retrieval at the end of the early years. *Leonardo Journal of Sciences*, 9(17):71 – 82, 2010.

[84] P. Kierkegaard. A method for detection of circular arcs based on the hough transform. *Machine Vision and Applications*, 5:249–263, 1992.

[85] W. Kim and Y. Kim. A region-based shape descriptor using zernike moments. *Signal Processing-image Communication*, 16:95–102, 2000.

[86] E. Kintner. On the mathematical properties of zernike polynomials. *Journal of Modern Optics*, 23(8):679–680, 1976.

[87] M. Kuramochi and G. Karypis. Frequent subgraph discovery. In *Proceedings of the 2001 International Conference on Data Mining*, pages 313–320, 2001.

[88] L. Latecki and R. Lakamper. Shape similarity measure based on correspondence of visual parts. *IEEE Transactions on Pattern Analysis and Machine Intelligence*, 22(10):1185 – 1190, 2000.

[89] V. Leavers. *Shape Detection in Computer Vision Using the Hough Transform*. Springer-Verlag New York, Inc., 1992.

[90] S. Lessmann, B. Baesens, C. Mues, and S. Pietsch. Benchmarking classification models for software defect prediction: A proposed framework and novel findings. *IEEE Transactions on Software Engineering*, 34:485–496, 2008.

[91] S. Li, M. Lee, and D. Adjeroh. Effective invariant features for shape-based image retrieval: Research articles. *Journal of the American Society for Information Science and Technology*, 56:729–740, 2005.

[92] T. Lindeberg. Scale-space theory: A basic tool for analysing structures at different scales. *Journal of Applied Statistics*, 21:224–270, 1994.

[93] S. Loncaric. A survey of shape analysis techniques. *Pattern Recognition*, 31:983–1001, 1998.

[94] S. Loncaric and A. Dhawan. A morphological signature transform for shape description. *Pattern Recognition*, pages 1029–1037, 1993.

[95] D. Lowd. Naive bayes models for probability estimation. In *Proceedings of the Twenty-second International Conference on Machine Learning*, pages 529–536. ACM Press, 2005.

[96] D. Lowe. Distinctive image features from scale-invariant keypoints. *International Journal of Computer Vision*, 60:91–110, 2004.

[97] G. Lu and A. Sajjanhar. Region-based shape representation and similarity measure suitable for content-based image retrieval. *Multimedia Systems*, 7:165–174, 1999.

[98] I. Lyoo, A. Satlin, C. Lee, and P. Renshaw. Regional atrophy of the corpus callosum in subjects with alzheimer's disease and multi-infarct dementia. *Psychiatry Research*, 74(2):63–72, 1997.

[99] J. Marroquin, B. Vemuri, S. Botello, E. Calderon, and A. Fernandez-Bouzas. An accurate and efficient bayesian method for automatic segmentation of brain mri. *IEEE Transactions on Medical Imaging*, 21(8):934 –945, 2002.

[100] T. Mitchell. *Machine Learning*. McGraw Hill, 1997.

[101] F. Mokhtarian and M. Bober. *Curvature Scale Space Representation: Theory, Applications, and MPEG-7 Standardization.* Kluwer Academic Publishers, 2003.

[102] F. Mokhtarian and A. Mackworth. Scale-based description and recognition of planar curves and two-dimensional objects. *IEEE Transactions on Pattern Analysis and Machine Intelligence*, 8:34–43, 1986.

[103] T. Moon. The expectation-maximization algorithm. *IEEE Signal Processing Magazine*, 13(6):47 –60, 1996.

[104] J. Morra, Z. Tu, L. Apostolova, A. Green, C. Avedissian, S. Madsen, N. Parikshak, X. Hua, A. Toga, C. Jack Jr., M. Weiner, and P. Thompson. Validation of a fully automated 3d hippocampal segmentation method using subjects with alzheimer's disease mild cognitive impairment, and elderly controls. *NeuroImage*, 43(1):59 – 68, 2008.

[105] R. Mukundan and K. R. Ramakrishnan. Fast computation of legendre and zernike moments. *Pattern Recognition*, 1995.

[106] H. Muller, N. Michoux, D. Bandon, and A. Geissbuhler. A review of content-based image retrieval systems in medical applications–clinical benefits and future directions. *International Journal of Medical Informatics*, 73(1):1 – 23, 2004.

[107] D. Mumford. Mathematical theories of shape: do they model perception? *Geometric Methods in Computer Vision*, 1570(1):2–10, 1991.

[108] P. Nikhil and P. Sankar. A review on image segmentation techniques. *Pattern Recognition*, 26(9):1277 – 1294, 1993.

[109] T. Ojala, M. Pietikainen, and T. Maenpaa. Multiresolution gray-scale and rotation invariant texture classification with local binary patterns. *IEEE Transactions on Pattern Analysis and Machine Intelligence*, 24(7):971 –987, 2002.

[110] C. Ordonez and E. Omiecinski. Discovering association rules based on image content. In *Proceedings of the IEEE Forum on Research and Technology Advances in Digital Libraries*, pages 38–49. IEEE Computer Society, 1999.

[111] A. Ozturk, B. Tascioglu, M. Aktekin, Z. Kurtoglu, and I. Erden. Morphometric comparison of the human corpus callosum in professional musicians and non-musicians by using in vivo magnetic resonance imaging. *Journal of Neuroradiology*, 29(1):29–34, 2002.

[112] D. Pao, H. Li, and R. Jayakumar. Shapes recognition using the straight line hough transform: Theory and generalization. *IEEE Transactions on Pattern Analysis and Machine Intelligence*, 14:1076–1089, 1992.

[113] T. Pavlidis. *Algorithms for Graphics and Image Processing.* Springer, 1982.

[114] P. Perner. Image mining: issues, framework, a generic tool and its application to medical-image diagnosis. *Engineering Applications of Artificial Intelligence*, 15(2):205 – 216, 2002.

[115] M. Peura and J. Iivarinen. Efficiency of simple shape descriptors. In *Proceedings of Advances in Visual Form Analysis*, pages 443–451. World Scientific, 1997.

[116] I. Pitas and A. Venetsanopoulos. Morphological shape decomposition. *IEEE Transactions on Pattern Analysis and Machine Intelligence*, 12:38–45, 1990.

[117] S. Powell, V. Magnotta, H. Johnson, V. Jammalamadaka, R. Pierson, and N. Andreasen. Registration and machine learning-based automated segmentation of subcortical and cerebellar brain structures. *NeuroImage*, 39(1):238 – 247, 2008.

[118] M. Prastawa, J. Gilmore, W. Lin, and G. Gerig. Automatic segmentation of mr images of the developing newborn brain. *Medical Image Analysis*, 9(5):457–466, 2005.

[119] A. Prata and W. Rusch. Algorithm for computation of zernike polynomials expansion coefficients. *Applied Optics*, 28:749 – 754, 1989.

[120] R. Prokop and A. Reeves. A survey of moment-based techniques for unoccluded object representation and recognition. *CVGIP: Graphical Models and Image Processing*, 54:438–460, 1992.

[121] A. Quddus and M. Gabbouj. Wavelet-based corner detection technique using optimal scale. *Pattern Recognition Letters*, 23:215–220, 2002.

[122] J. Quinlan. *C4.5: programs for machine learning.* Morgan Kaufmann Publishers Inc., 1993.

[123] A. Reeves, R. Prokop, S. Andrews, and F. Kuhl. Three-dimensional shape analysis using moments and fourier descriptors. *IEEE Transactions on Pattern Analysis and Machine Intelligence*, 10:937–943, 1988.

[124] J. Riley, D. Franklin, V. Choi, R. Kim, D. Binder, S. Cramer, and J. Lin. Altered white matter integrity in temporal lobe epilepsy: Association with cognitive and clinical profiles. *Epilepsia*, 51(4):536–545, 2010.

[125] S. Ruan, B. Moretti, J. Fadili, and D. Bloyet. Fuzzy markovian segmentation in application of magnetic resonance images. *Computer Vision and Image Understanding*, 85(1):54 – 69, 2002.

[126] Y. Rui, A. She, and T. Huang. Modified fourier descriptors for shape representation – a practical approach. In *Proceedings of first international workshop on image databases and multimedia search*, 1996.

[127] H. Sakoe and S. Chiba. Dynamic programming algorithm optimization for spoken word recognition. *IEEE Transactions on Acoustics, Speech and Signal Processing*, 26(1):43–49, 1978.

[128] D. Salat, A. Ward, J. Kaye, and J. Janowsky. Sex differences in the corpus callosum with aging. *Neurobiology of Aging*, 18(2):191–197, 1997.

[129] M. Sampat, A. Berger, B. Healy, P. Hildenbrand, J. Vass, D. Meier, T. Chitnis, H. Weiner, R. Bakshi, and C. Guttmann. Regional white matter atrophybased classification of multiple sclerosis in cross-sectional and longitudinal data. *American Journal of Neuroradiology*, 30(9):1731–1739, 2009.

[130] D. Sankoff and J. Kruskal. *Time Warps, String Edits, and Macromolecules.* Center for the Study of Language and Information, 1999.

[131] Y. Sato. Piecewise linear approximation of plane curves by perimeter optimization. *Pattern Recognition*, 25(12):1535 – 1543, 1992.

[132] G. Schlaug, L. Jancke, Y. Huang, J. Staiger, and H. Steinmetz. Increased corpus callosum size in musicians. *Neuropsychologia*, 33(8):1047–1055, 1995.

[133] Y. Sheng and J. Duvernoy. Circular-fourier-radial-mellin transform descriptors for pattern recognition. *Journal of The Optical Society of America A-optics Image Science and Vision*, 3:885–888, 1986.

[134] Y. Sheng and L. Shen. Orthogonal fourier-mellin moments for invariant pattern recognition. *Journal of the Optical Society of America (JOSA)*, 11(6):1748–1757, 1994.

[135] J. Shi and J. Malik. Normalized cuts and image segmentation. *IEEE Transactions on Pattern Analysis and Machine Intelligence*, 22:888–905, 2000.

[136] S. Shiu and S. Pal. *Foundations of Soft Case-Based Reasoning.* John Wiley & Sons, 2004.

[137] M. Siyal and L. Yu. An intelligent modified fuzzy c-means based algorithm for bias estimation and segmentation of brain mri. *Pattern Recognition Letters*, 26(13):2052 – 2062, 2005.

[138] P. Smyth. Belief networks, hidden markov models, and markov random fields: a unifying view. *Pattern Recognition Letters*, 18:1261–1268, 1998.

[139] J. Suckling, T. Sigmundsson, K. Greenwood, and E. Bullmore. A modified fuzzy clustering algorithm for operator independent brain tissue classification of dual echo mr images. *Magnetic Resonance Imaging*, 17(7):1065 – 1076, 1999.

[140] F. Tao, F. Murtagh, and M. Farid. Weighted association rule mining using weighted support and significance framework. In *Proceedings of ACM SIGKDD International Conference on Knowledge Discovery and Data Mining*, 2003.

[141] M. Teague. Image analysis via the general theory of moments. *Journal of the Optical Society of America (1917-1983)*, 70:920–930, 1980.

[142] C. Teh and R. Chin. On image analysis by the methods of moments. *IEEE Transactions on Pattern Analysis and Machine Intelligence*, 10(4):496 –513, 1988.

[143] R. Veltkamp. Shape matching: similarity measures and algorithms. In *Proceedings of International Conference on Shape Modeling and Applications, SMI2001*, pages 188–197, 2001.

[144] J. Vial, H. Nocairi, P. Sassiat, S. Mallipatu, G. Cognon, D. Thiebaut, B. Teillet, and D. Rutledge. Combination of dynamic time warping and multivariate analysis for the comparison of comprehensive two-dimensional gas chromatograms application to plant extracts. *Journal of Chromatography A*, 2008.

[145] M. Vlachos, Z. Vagena, P. Yu, and V. Athitsos. Rotation invariant indexing of shapes and line drawings. In *Proceedings of the 14th ACM international conference on Information and knowledge management*, CIKM '05, pages 131–138. ACM, 2005.

[146] J. Wang, G. deHaan, D. Unay, O. Soldea, and A. Ekin. Voxel-based discriminant map classification on brain ventricles for alzheimer's disease. In *SPIE Medical Imaging*, 2009.

[147] L. Wang, J. Swank, I. Glick, M. Gado, M. Miller, J. Morris, and J. Csernansky. Changes in hippocampal volume and shape across time distinguish dementia of the alzheimer type from healthy aging. *NeuroImage*, 20(2):667–682, 2003.

[148] P. Wang and H. Wang. A modified fcm algorithm for mri brain image segmentation. In *Proceedings of the 2008 International Seminar on Future BioMedical Information Engineering*, pages 26–29. IEEE Computer Society, 2008.

[149] B. Weber, E. Luders, J. Faber, S. Richter, C. Quesada, H. Urbach, P. Thompson, A. Toga, C. Elger, and C. Helmstaedter. Distinct regional atrophy in the corpus callosum of patients with temporal lobe epilepsy. *Brain*, 130(12):3149–3154, 2007.

[150] C. Wee and R. Paramesran. On the computational aspects of zernike moments. *Image and Vision Computing*, 25:967–980, 2007.

[151] S. Weis, M. Kimbacher, E. Wenger, and A. Neuhold. Morphometric analysis of the corpus callosum using mri: Correlation of measurements with aging in healthy individuals. *American Journal of Neuroradiology*, 14(3):637–645, 1993.

[152] C. Wu, S. Horng, and P. Lee. A new computation of shape moments via quadtree decomposition. *Pattern Recognition*, 34(7):1319 – 1330, 2001.

[153] J. Wu, D. Hong, M. Kankanhalli, and J. Lim. *Perspectives on Content-Based Multimedia Systems*. Kluwer Academic Publishers, 2000.

[154] J. Xue, S. Ruan, B. Moretti, M. Revenu, and D. Bloyet. Knowledge-based segmentation and labeling of brain structures from mri images. *Pattern Recognition Letters*, 22(3-4):395 – 405, 2001.

[155] X. Yan and J. Han. gspan: Graph-based substructure pattern mining. In *Proceedings of the 2002 International Conference on Data Mining*, page 721, 2002.

[156] X. Yan, P. Yu, and J. Han. Graph indexing: A frequent structure-based approach. In *Proceedings of SIGMOD Conference'04*, pages 335–346, 2004.

[157] W. Yang, X. Chen, H. Xie, and X. Huang. Ica-based automatic classification of magnetic resonance images from adni data. In *Proceedings of the 2010 international conference on Life system modeling and simulation and intelligent computing, and 2010 international conference on Intelligent computing for sustainable energy and environment: Part III*, LSMS/ICSEE'10, pages 340–347. Springer-Verlag, 2010.

[158] R. Yip, P. Tam, and D. Leung. Modification of hough transform for circles and ellipses detection using a 2-dimensional array. *Pattern Recognition.*

[159] H. Yuen, J. Princen, J. Illingworth, and J. Kittler. Comparative study of hough transform methods for circle finding. *Image and Vision Computing*, 8:71–77, 1990.

[160] C. Zahn and R. Roskies. Fourier descriptors for plane closed curves. *IEEE Transactions on Computers*, C-21(3):269 –281, 1972.

[161] O. Zaiane, M. Antonie, and A. Coman. Mammography classification by an association rule-based classifier. In *Proceedings of International Workshop on Multimedia Data Mining*, pages 62–69, 2002.

[162] D. Zhang and G. Lu. A comparative study of fourier descriptors for shape representation and retrieval. In *Proceedings of 5th Asian Conference on Computer Vision (ACCV)*, pages 646–651. Springer, 2002.

[163] D. Zhang and G. Lu. Shape-based image retrieval using generic fourier descriptor. *Signal Processing: Image Communication*, 17(10):825 – 848, 2002.

[164] D. Zhang and G. Lu. Evaluation of mpeg-7 shape descriptors against other shape descriptors. *Multimedia Systems*, 9:15–30, 2003.

[165] D. Zhang and G. Lu. Review of shape representation and description techniques. *Pattern Recognition*, 37(1):1–19, 2004.

[166] J. Zhang, W. Hsu, and M. Lee. Image mining: Issues, frameworks and techniques. In *Proceedings of Knowledge Discovery and Data Mining*, pages 13–20, 2001.

[167] J. Zhang, W. Hsu, and M. Li Lee. An information-driven framework for image mining. In *Proceedings of the 12th International Conference on Database and Expert Systems Applications*, DEXA '01, pages 232–242. Springer-Verlag, 2001.

[168] Q. Zhang and R. Segall. Web mining: A survey of current research, techniques, and software. *International Journal of Information Technology & Decision Making (IJITDM)*, 7(4):683–720, 2008.

[169] Y. Zhang, M. Brady, and S. Smith. Segmentation of brain mr images through a hidden markov random field model and the expectation-maximization algorithm. *IEEE Transactions on Medical Imaging*, 20(1):45 –57, 2001.

Appendix A

Published Work

In this appendix a list of publications to date from the work described in this thesis is presented:

Refereed Conferences:

[1] A. Elsayed, F. Conenen, C. Jiang, M. García-Fiñana and V. Slumming. *Corpus Callosum MR Image Classification.* Research and Development in Intelligent Systems XXVI incorporating Applications and Innovations in Intelligent Systems XVII, Proceedings AI'2009, Springer, London, pages (333-348), 2009. **Winner of the Best Application Paper Prize.**

[2] A. Elsayed, F. Conenen, M. García-Fiñana and V. Slumming. *Region Of Interest Based Image Categorization.* Proceedings 12th Int. Conf.on Data Warehousing and Knowledge Discovery (DaWaK'10),Springer LNCS 6263, pages (239-250), 2010.

[3] A. Elsayed, F. Conenen, M. García-Fiñana and V. Slumming. *Region Of Interest Based Image Classification Using Time Series Analysis.* Proceedings Int. Joinit Conf. on Neural Network (Special Session on Soft Computing in Medical Imaging), part of IEEE World Congress on Computational Intelligence (WCCI'10), pages (3501-3507), 2010.

[4] A. Elsayed, F. Conenen, M. García-Fiñana and V. Slumming. *MRI Brain Scan Classification According to The Nature of The Corpus Callosum.* Proceedings Medical Image Understanding and Analysis (MIUA'10), pages (19-23), 2010.

[5] A. Elsayed, M. Hijazi, F. Conenen, M. García-Fiñana, V. Slumming and Y. Zheng. *Image Categorisation Using Time Series Case Based Reasoning.* Proceedings of 15th UK Workshop on Case-Based Reasoning, pages (2-11), BCS-SGAI,

Cambridge, 2010.

[6] A. Elsayed, M. Hijazi, F. Conenen, M. García-Fiñana, V. Slumming and Y. Zheng. *Time Series Case Based Reasoning for Image Categorisation.* In A. Ram and N. Wiratunga (Eds.): ICCBR 2011, pages (423-436), 2011.

Journal papers:

[7] A. Elsayed, F. Conenen, C. Jiang, M. García-Fiñana and V. Slumming. *Corpus Callosum MR Image Classification.* Volume 23, Issue 4, pages (330-336). Knowledge-Based Systems (KBS) journal, 2010.

[8] A. Elsayed, F. Conenen, M. García-Fiñana and V. Slumming. *Classification of MRI brain scan data using shape criteria.* To appear in the Annals of the British Machine Vision Association (BMVA).